

Abstract

Measurement of the collision energy dependence of jet-quenching signatures of de-confinement at STAR

Stephen Horvat

2017

Confinement is a phenomenon where quarks and gluons are only found in bound color-neutral states, or hadrons. Experiments at the Brookhaven National Laboratory (BNL) and the European Organization for Nuclear Research (CERN) have measured and published key signatures for the formation of a state of nuclear matter where quarks are temporarily de-confined in the hot, dense aftermath of heavy-ion nuclear collisions at $\sqrt{s_{\text{NN}}} = 200$ GeV. This de-confined state corresponds to the theoretically predicted quark gluon plasma (QGP). One reported QGP signature was the suppression of high momentum particles using nuclear modification factors. STAR is now analyzing data produced in the RHIC Beam Energy Scan (BES) which spans $\sqrt{s_{\text{NN}}} = 7.7 - 62.4$ GeV.

This dissertation reports the collision energy dependence of nuclear modification factors. The high-transverse-momentum (high- p_{T}) suppression reported at higher $\sqrt{s_{\text{NN}}}$ is seen to turn off and be replaced by an enhancement of high- p_{T} particle production as the collision energy is reduced. The physics that leads to this strong enhancement competes against and obscures the physics leading toward suppression. Only when the suppression is stronger than the enhancement do the nuclear modification factors provide a clean signature of QGP formation. This dissertation also outlines a new procedure to better disentangle suppression effects from enhancement effects. In this procedure, the centrality dependence of enhancement and suppression effects are exploited with the goal of establishing a limit for the minimum collision energy needed to produce a QGP in central heavy-ion collisions.

**Measurement of the collision energy
dependence of jet-quenching signatures
of de-confinement at STAR**

A Dissertation

Presented to the Faculty of the Graduate School

of

Yale University

in Candidacy for the Degree of

Doctor of Philosophy

by

Stephen Paul Horvat

Dissertation Director: Helen Caines

December 2017

© by Stephen Paul Horvat
All rights reserved.

Acknowledgements

I would like to thank the Yale Relativistic Heavy Ion Group, Brookhaven National Laboratory, and the STAR experiment for facilitating the research that went into this dissertation. In particular, I would like to thank my adviser Helen Caines whose scientific expertise guided me through this research. I would also like to thank John Harris, who with Helen Caines has formed an open, welcoming, and collaborative environment for students to grow into researchers and mentors. To my office-mates and fellow group members: thank you for answering my many questions and for sharing fantastic lunch conversations. Thank you to my family for your support, and especially my most cherished collaborator and partner: Elizabeth.

Contents

Acknowledgements	ii
List of Figures	v
List of Tables	x
Acronyms	xi
Symbols	xii
1 Introduction	1
1.1 Quark-Gluon Plasma	2
1.1.1 Heavy-Ion Collisions	2
1.1.2 Signatures of Quark Gluon Plasma	9
1.2 Beam Energy Scans	14
2 Nuclear Modification of High-p_T Probes	17
2.1 Glauber Monte Carlo	19
2.2 Trigger and Vertex Reconstruction Efficiency	20
2.3 Spectra	21
2.4 R_{dAu}	23
2.5 R_{CP}	24
2.6 Y	27
3 Experimental Setup	28
3.1 The Relativistic Heavy Ion Collider	29
3.2 The Solenoidal Tracker at RHIC	30
3.2.1 Time Projection Chamber	31
3.2.2 Trigger Detectors	33
3.2.3 Minimum Bias Triggers	33
3.2.4 Data Acquisition and Event Reconstruction	34
4 Quality Assurance	36

4.1	Data	37
4.2	Good Run and Event Selection	37
4.3	Good Track Selection	42
5	Corrections	45
5.1	FeedException, Knockout, and Photo-Production	46
5.2	Tracking Efficiency	49
5.3	Identified Spectra Fits	52
5.4	Momentum Resolution and Energy Loss	53
5.5	Combined Correction	57
6	Systematic Uncertainties	60
7	Results	66
7.1	p_T -spectra	66
7.2	$\langle p_T \rangle$	69
7.3	R_{CP}	69
7.4	S_{loss}	72
7.5	Y	74
8	Discussion	80
8.1	Spectra	81
8.2	$\langle p_T \rangle$	82
8.3	R_{CP}	84
8.4	S_{loss}	85
8.5	Y	86
9	Modeling Heavy-Ion Collisions	88
9.1	HIJING	91
9.2	AMPT	92
9.2.1	String-Melting On	93
9.2.2	String-Melting Off	94
9.3	UrQMD	96
9.4	Summary	99
10	Conclusions and Outlook	100
A	Glauber Monte Carlo Results	104
	Glossary	108
	Bibliography	109

List of Figures

1.1	The stages of heavy-ion collisions at sufficiently high $\sqrt{s_{\text{NN}}}$ to form a QGP [5].	3
1.2	Proton next to next to leading order (NNLO) PDF from CTEQ-TEA for gluons, the two valence up quarks, the valence down quark, and sea quarks. The PDFs are shown for $Q = 2 \text{ GeV}$ and $Q = 100 \text{ GeV}$ [6].	4
1.3	An example of the typical nuclear modification of a PDF from DIS measurements. The characteristic ordering of the shadowing, anti-shadowing, EMC effect, and Fermi motion regions are labeled [7].	4
1.4	The initial energy density distribution in the transverse plane generated for a small impact parameter heavy-ion collision using the IP-Glasma model [16].	6
1.5	0-10% λ spectra from STAR at $\sqrt{s_{\text{NN}}} = 200 \text{ GeV}$ described by a model including fragmentation, coalescence, and weak decay feed-down [34].	8
1.6	Antiproton to negative pion ratio from STAR and PHENIX in 0-10% at $\sqrt{s_{\text{NN}}} = 200 \text{ GeV}$ described by a model including fragmentation, coalescence, and weak feed-down and radial flow for the solid red curve [34].	9
1.7	A Glauber Monte Carlo simulation of a mid-peripheral Au+Au collision at $\sqrt{s_{\text{NN}}} = 200 \text{ GeV}$ with a fluctuation driven triangular distribution of participating nucleons [37].	10
1.8	The nuclear modification factor, R_{AA} , for π^0 and h^\pm for $\sqrt{s_{\text{NN}}} = 17.3 \text{ GeV} - 2.76 \text{ TeV}$ [42].	12
1.9	The nuclear phase diagram with the regions that are accessible at the large hadron collider (LHC) and RHIC highlighted [46].	15
2.1	Direct photon R_{AA} measured by PHENIX for 0-5% centrality in $\sqrt{s_{\text{NN}}} = 200 \text{ GeV}$ [49].	20
2.2	STAR detector level charged multiplicity in $ \eta < 0.5$ for data compared to Glauber Monte Carlo expectation for $\sqrt{s_{\text{NN}}} = 200 \text{ GeV}$ [51].	21
2.3	STAR detector level charged tracks reconstructed in each (η , V_Z) bin at $\sqrt{s_{\text{NN}}} = 7.7 \text{ GeV}$	22
2.4	Fully corrected charged hadron p_T spectra from $p+p$ collisions and several centralities of Au+Au at $\sqrt{s_{\text{NN}}} = 200 \text{ GeV}$ [45].	22
2.5	Fully corrected pion, proton, and charged hadron R_{dAu} at $\sqrt{s_{\text{NN}}} = 200 \text{ GeV}$ for minimum bias as well as 0-20% collisions[53].	24
2.6	Fully corrected charged hadron R_{CP} at $\sqrt{s_{\text{NN}}} = 200 \text{ GeV}$ with two different peripheral reference centralities [45].	25

2.7	Fully corrected charged hadron R_{AA} at $\sqrt{s_{NN}} = 200$ GeV for six centrality classes [45].	26
2.8	Fully corrected π^0 R_{AA} at $\sqrt{s_{NN}} = 39, 62.4,$ and 200 GeV versus N_{part} [59].	26
3.1	The site map for RHIC.	29
3.2	Schematic of the STAR detector.	31
3.3	The inner and outer anode pad geometries for each STAR TPC sector consist of 30 densely spaced outer pad rows and 15 sparsely spaced inner pad rows [68].	32
3.4	Summary of the event reconstruction algorithm used in STAR [79].	34
4.1	The mean p_T of each run is shown in the upper figure and the mean charge of each run is shown in the lower for $\sqrt{s_{NN}} = 7.7$ GeV. Runs were excluded if means of physics quantities within those runs were not within 3σ of the average.	38
4.2	The reconstructed vertex V_Z distributions are shown for $\sqrt{s_{NN}} = 7.7$ GeV (left) and $\sqrt{s_{NN}} = 200$ GeV (right).	39
4.3	The $\sqrt{s_{NN}} = 7.7$ GeV reconstructed vertex distribution is shown on the left for (V_X, V_Y) and on the right for V_R	40
4.4	The number of events that pass all run and event cuts is given by Event Flag = 0 for $\sqrt{s_{NN}} = 7.7$ (a) and 62.4 GeV (b). The other Event Flag indices count the number of events that failed each cut.	41
4.5	Signed DCA of charged hadrons for $\sqrt{s_{NN}} = 7.7$ GeV.	42
4.6	Primary p_T, p_T^{pr} , is plotted on the x-axis and global p_T, p_T^{gl} , on the y-axis for $\sqrt{s_{NN}} = 39$ GeV. The right plot is the same as the left except that it includes the cut: $7/10 \cdot p_T^{\text{gl}} < p_T^{\text{pr}} < 10/7 \cdot p_T^{\text{gl}}$	44
5.1	Fit of feeddown correction factor for charged hadrons in $0 < Mult \leq 20$ at $\sqrt{s_{NN}} = 7.7$ GeV as a function of p_T	46
5.2	Linear fits of the $Mult$ dependence of parameters p0 (a), p1 (b), and p2 (c) from Eq. 5.1 for $\sqrt{s_{NN}} = 7.7$ GeV.	47
5.3	Feeddown correction used for $\sqrt{s_{NN}} = 7.7$ GeV.	48
5.4	Fit of single species efficiency from embedding of π^+, K^+ , and p into $0 < Mult < 20$ for $\sqrt{s_{NN}} = 7.7$ GeV.	50
5.5	Fits of the $Mult$ dependence of $\sqrt{s_{NN}} = 7.7$ GeV π^+ efficiency parameters p0 (a), p1 (b), and p2 (c)	51
5.6	Fit of single species efficiency from embedding of π^+ for $\sqrt{s_{NN}} = 7.7$ GeV.	52
5.7	Fit to the spectra of π^+ for peripheral 60-80% $\sqrt{s_{NN}} = 7.7$ GeV.	53
5.8	Fit parameters as a function of centrality for π^+ at $\sqrt{s_{NN}} = 7.7$ GeV for parameters p0 (a), p1 (b), and p2 (c).	54
5.9	The fits of the spectra were used to construct this 2D function to describe the spectra as a function of p_T and $Mult$ shown here for $\sqrt{s_{NN}} = 7.7$ GeV.	55
5.10	The distributions of p_T shifts as a function of p_T are shown for π^+, K^+ , and p for $\sqrt{s_{NN}} = 7.7$ GeV.	56

5.11	The distributions of p_T shifts as a function of p_T are shown for p at $\sqrt{s_{NN}} = 7.7$ and 62.4 GeV projected over $4.5 < p_T < 4.75$ GeV/c and fit with Gaussians.	57
5.12	Momentum resolution as a function of p_T and fit at high- p_T with a linear fit for π^+ at $\sqrt{s_{NN}} = 7.7$ GeV and 62.4 GeV. The momentum resolution is similar for the other species and energies.	57
5.13	Ratio of smeared spectra to non-smeared spectra as a function of p_T for π^+ at $\sqrt{s_{NN}} = 7.7$ GeV and 62.4 GeV.	58
5.14	Combined corrections as a function of p_T and $Mult$ for inclusive charged hadrons for each energy in the BES.	59
6.1	Total systematic uncertainties for p_T spectra (from tracking efficiency, momentum resolution, and weak decay feed-down in summed in quadrature) are shown for each $\sqrt{s_{NN}}$ as a function of p_T and detector level multiplicity measured in $ \eta < 0.5$	63
6.2	Total systematic uncertainties for p_T spectra (from tracking efficiency, momentum resolution, and weak decay feed-down in summed in quadrature) are shown for each $\sqrt{s_{NN}}$ as a function of p_T and detector level multiplicity measured in $ \eta < 0.5$	64
7.1	Corrected charged hadron spectra for each $\sqrt{s_{NN}}$ and centrality bin as a function of p_T and measured in $ \eta < 0.5$. Systematic uncertainty bands are shown but are generally smaller than the symbol size.	67
7.2	Charged hadron $\langle p_T \rangle$ in $ \eta < 0.5$ for $\sqrt{s_{NN}} = 7.7, 11.5, 14.5, 19.6, 27, 39,$ and 62.4 GeV and in 0-5%, 5-10%, 10-20%, 20-40%, 40-60%, and 60-80% centrality bins. The error bars on the points are from statistical uncertainty only and are smaller than the markers. The systematic uncertainties would be highly correlated with centrality and $\sqrt{s_{NN}}$ with the dominant uncertainties arising from tracking efficiency and feed-down corrections. The point-to-point systematic uncertainties should be smaller than 0.01 GeV/c	68
7.3	Charged hadron R_{CP} in $ \eta < 0.5$ are shown for $\sqrt{s_{NN}} = 7.7, 11.5, 14.5, 19.6, 27, 39,$ and 62.4 GeV. N_{part} scaling is indicated for each collision energy by the colored lines at $p_T = 0$ GeV/c. The error bands at unity on the right side of the plot indicate the N_{bin} scaling uncertainty. The error bars on the points are for their statistical uncertainty and the boxes on the points are for their systematic uncertainties.	70
7.4	Identified $\pi^\pm, K^\pm, p,$ and \bar{p} R_{CP} in $ y < 0.25$ is shown for $\sqrt{s_{NN}} = 7.7, 11.5, 19.6, 27, 39,$ and 62.4 GeV. The gray boxes at unity on the left side of the plot indicate the N_{bin} scaling uncertainty. The error bars on the points are for their statistical uncertainty and the boxes on the points are for their systematic uncertainties [90].	71

7.5	Negative charged hadron R_{CP} in $ \eta < 0.5$ is shown for $\sqrt{s_{NN}} = 7.7, 11.5, 14.5, 19.6, 27, 39,$ and 62.4 GeV. N_{part} scaling is indicated for each collision energy on the y-axis. The error bands at unity on the right side of the plot indicate the N_{bin} scaling uncertainty. The error bars on the points are for their statistical uncertainty and the boxes on the points are for their systematic uncertainties.	72
7.6	Charged hadron S_{loss} in $ \eta < 0.5$ is shown for $\sqrt{s_{NN}} = 7.7, 11.5, 14.5, 19.6, 27, 39, 62.4,$ and 200 GeV. Systematic uncertainties due to N_{bin} scaling would dominate the uncertainties of this measurement and are $\approx 4\%$	73
7.7	Negative charged hadron S_{loss} in $ \eta < 0.5$ is shown for $\sqrt{s_{NN}} = 7.7, 11.5, 14.5, 19.6, 27, 39, 62.4,$ and 200 GeV. Systematic uncertainties due to N_{bin} scaling would dominate the uncertainties of this measurement and are $\approx 4\%$	74
7.8	Charged hadron $Y(N_{part})$ in $ \eta < 0.5$ for $\sqrt{s_{NN}} = 7.7, 11.5, 14.5, 19.6, 27, 39, 62.4,$ and 200 GeV. The statistical uncertainty bars are mostly smaller than the marker sizes. The error band is the quadrature sum of the uncertainty on N_{bin} and the uncertainty from the feed-down correction. The left panel shows Y for $3 < p_T < 3.5$ GeV/c while the right panel shows Y for $4 < p_T < 4.5$ GeV/c.	75
7.9	Charged hadron $Y(N_{part})$ in $ \eta < 0.5$ for $\sqrt{s_{NN}} = 14.5$ GeV. The statistical uncertainty bars are mostly smaller than the marker sizes. The error band is the quadrature sum of the uncertainty on N_{bin} and the uncertainty from the feed-down correction.	76
7.10	Charged hadron [(0-5%)/(10-20%)] R_{CP} in $ \eta < 0.5$ is shown for $\sqrt{s_{NN}} = 7.7, 11.5, 14.5, 19.6, 27, 39,$ and 62.4 GeV. N_{part} scaling is indicated for each collision energy on the y-axis. The error bands at unity on the right side of the plot indicate the N_{bin} scaling uncertainty. The error bars on the points are for their statistical uncertainty while the highly correlated point-to-point systematic uncertainties are suppressed.	77
7.11	Negative charged hadron $Y(N_{part})$ in $ \eta < 0.5$ for $3 < p_T < 3.5$ GeV/c and for $\sqrt{s_{NN}} = 7.7, 11.5, 14.5, 19.6, 27, 39, 62.4,$ and 200 GeV. The statistical uncertainty bars are mostly smaller than the marker sizes. The error band is the quadrature sum of the uncertainty on N_{bin} and the uncertainty from the feed-down correction.	78
8.1	Charged hadron 0-5% central p_T -spectra in $ \eta < 0.5$ is shown for $\sqrt{s_{NN}} = 7.7$ GeV Au+Au collisions with an exponential fit.	80
8.2	Corrected charged hadron p_T -spectra for 0-5% central Au+Au collisions at $\sqrt{s_{NN}} = 7.7$ (a) and 62.4 GeV (b) with two component fits. The exponential contribution to the fit is shown with the green curve while the power-law contribution is shown with the blue curve.	81
8.3	$\langle p_T \rangle$ for identified species in the BES [89].	82
8.4	p/π as a function of N_{part} for $\sqrt{s_{NN}} = 7.7, 11.5, 19.6, 27, 39, 62.4,$ and 200 GeV [89].	83

8.5	Identified p , \bar{p} , K^\pm , and π^\pm $Y(N_{\text{part}})$ in $ y < 0.25$ is shown for $\sqrt{s_{\text{NN}}} = 7.7, 11.5, 19.6, 27, 39, \text{ and } 62.4$ GeV. The error bands are the quadrature sum of the uncertainties on N_{bin} , from the feed-down correction, from the tracking efficiency, and from the particle identification procedure [90].	87
9.1	The correlation of impact parameter with charged multiplicity in $ \eta < 0.5$ at $\sqrt{s_{\text{NN}}} = 14.5$ GeV from UrQMD.	89
9.2	HIJING generated charged hadron R_{CP} in $ \eta < 0.5$ are shown for $\sqrt{s_{\text{NN}}} = 7.7, 11.5, 19.6, 27, 39, 62.4, \text{ and } 200$ GeV for 0-5% over 60-80% centrality bins.	90
9.3	Ratios of charged hadron p_{T} spectra from HIJING to those from data for 0-5% central (a) and 60-80% peripheral collisions (b) for $\sqrt{s_{\text{NN}}} = 7.7, 11.5, 19.6, 27, 39, 62.4, \text{ and } 200$ GeV.	91
9.4	AMPT generated charged hadron R_{CP} in $ \eta < 0.5$ for $\sqrt{s_{\text{NN}}} = 7.7, 11.5, 19.6, 27, 39, 62.4, \text{ and } 200$ GeV for 0-5% over 60-80% centrality bins are shown from the string melting version of the model.	93
9.5	Ratios of charged hadron p_{T} spectra from the string melting version of AMPT to those from data for 0-5% central (a) and 60-80% peripheral collisions (b) for $\sqrt{s_{\text{NN}}} = 7.7, 11.5, 19.6, 27, 39, 62.4, \text{ and } 200$ GeV.	94
9.6	AMPT generated charged hadron R_{CP} in $ \eta < 0.5$ for $\sqrt{s_{\text{NN}}} = 7.7, 11.5, 19.6, 27, 39, 62.4, \text{ and } 200$ GeV for 0-5% over 60-80% centrality bins are shown from the default version of the model.	95
9.7	Ratios of charged hadron p_{T} spectra from the default version of AMPT to those from data for 0-5% central (a) and 60-80% peripheral collisions (b) for $\sqrt{s_{\text{NN}}} = 7.7, 11.5, 19.6, 27, 39, 62.4, \text{ and } 200$ GeV.	95
9.8	Ratios of charged hadron p_{T} spectra from the default version of HIJING to those from HIJING with AMPT's LUND splitting function parameter values for 0-5% central (a) and 60-80% peripheral collisions (b) for $\sqrt{s_{\text{NN}}} = 7.7, 11.5, 19.6, 27, 39, 62.4, \text{ and } 200$ GeV.	96
9.9	UrQMD generated charged hadron R_{CP} in $ \eta < 0.5$ for $\sqrt{s_{\text{NN}}} = 7.7, 11.5, 19.6, 27, 39, 62.4, \text{ and } 200$ GeV for 0-5% over 60-80% centrality bins are shown from the default version of the model.	97
9.10	Ratios of charged hadron p_{T} spectra from data to those from UrQMD are shown for 0-5% central (a) and 60-80% peripheral collisions (b) for $\sqrt{s_{\text{NN}}} = 7.7, 11.5, 19.6, 27, 39, 62.4$ GeV.	97
9.11	Ratios of charged hadron p_{T} spectra from UrQMD to those from data are shown for 0-5% central (a) and 60-80% peripheral collisions (b) for $\sqrt{s_{\text{NN}}} = 200$ GeV using an alternative centrality selection procedure.	98
9.12	The ratio of UrQMD generated charged hadron R_{CP} to that from data in $ \eta < 0.5$ for $\sqrt{s_{\text{NN}}} = 200$ GeV for 0-5% over 60-80% centrality bins are shown.	99
10.1	Dihadron correlations from $\sqrt{s_{\text{NN}}} = 39$ (a) and 200 GeV (b) for $3 < p_{\text{T}}^{\text{trigger}} < 10$ GeV/c and $1.5 < p_{\text{T}}^{\text{associated}} < 3$ GeV/c. These 2D correlations are not corrected for tracking efficiency and acceptance.	103

List of Tables

4.1	Data used in these analyses. The good event count is for events that pass the run and event quality cuts.	37
A.1	Nucleon-nucleon inelastic cross sections for each $\sqrt{s_{\text{NN}}}$	105
A.2	Negative binomial distribution parameter values.	105
A.3	$\langle N_{\text{bin}} \rangle$ for each energy and centrality used in these analyses.	106
A.4	$\langle N_{\text{part}} \rangle$ for each energy and centrality used in these analyses.	106

Acronyms

AGS	A lternating G radient S ynchotron
BBC	B eam B eam C ounter
BES	B eam E nergy S can
BNL	B rookhaven N ational L aboratory
CNM	C old N uclear M atter
DCA	D istance of C losest A pproach
EBIS	E lectron B eam I on S ource
PHENIX	P ioneering H igh E nergy N uclear I nteraction eX periment
RCF	R HIC C omputing F acility
RHIC	R elativistic H eavy I on C ollider
STAR	S olenoidal T racker A t R HIC
TOF	T ime O f F light
TPC	T ime P rojection C hamber
ZDC	Z ero D egree C alorimeter

Symbols

DCA	distance of closest approach between a reconstructed global track and a primary vertex	cm
$Mult$	charged multiplicity measured in TPC for $ \eta <0.5$ and corrected for reconstruction efficiency	unitless
$refMult$	charged multiplicity measured in TPC for $ \eta <0.5$ and not corrected for reconstruction efficiency	unitless
N_{bin}	average number of $p+p$ -like collisions within a centrality class	unitless
N_{part}	average number of participating nucleons within a centrality class	unitless
p_T	transverse momentum	GeV/ c
$\sqrt{s_{NN}}$	center of mass collision energy per nucleon pair	GeV
η	pseudorapidity	unitless

*In memory of my father and brother:
George Horvat and Kevin Horvat*

Chapter 1

Introduction

Quarks and gluons are subatomic particles that carry color charge and are only found in nature in color neutral groupings. There are three colors labeled red, green, and blue; plus the anti-colors associated with anti-particles. Gluons carry combinations of color charge and anti-color charge and are the force carrying bosons that bind quarks and anti-quarks together into mesons, $q\bar{q}$, as well as baryons, qqq and $\bar{q}\bar{q}\bar{q}$. Confinement is the condition that requires color neutrality to be preserved and prevents isolated quarks from being observed in nature [1]. The strong nuclear force, mediated by gluons, does not get weaker as colored particles are separated due to gluon self interactions [1]. Instead it grows roughly linearly with parton separations until, for sufficiently large distances, it becomes energetically favorable to form additional $q+\bar{q}$ pairs. It was proposed by Bohr and Nielsen that if rather than trying to separate quarks many quarks are squeezed into a small volume then the quarks will become de-confined [2]. This de-confined state of nuclear matter is called the quark-gluon plasma (QGP).

1.1 Quark-Gluon Plasma

If ordinary nuclear matter is heated enough, it will evaporate into a hadron gas. The number of degrees of freedom in this state is defined by the hadronic degrees of freedom. With further heating or increases in density it may be possible to transition from hadronic to partonic degrees of freedom. The cores of some neutron stars may achieve the required density to have their equation of state (EoS) described by partonic degrees of freedom [3], some with exotic forms such as color superconductors [4]. However, the methods available in the laboratory for melting hadrons are found to produce QGP, a higher temperature and lower density form of partonic matter than that found in neutron stars [2]. The laboratory tool that is used for these experiments is the high-energy heavy-ion collider.

1.1.1 Heavy-Ion Collisions

Nuclear accelerators work by stripping the electrons off of nuclei (ionization), using electric and magnetic fields to accelerate and steer the ions, and smashing beams of these ions into either fixed targets or other beams at nearly the speed of light¹. The time evolution of heavy-ion collisions may be broken down into several stages as in Fig. 1.1 [5]: a description of the nuclei before colliding, high momentum transfer interactions, low momentum transfer interactions, pre-equilibrium parton cascade and thermalization, QGP, QCD phase transition, hadron gas, chemical freeze-out, and kinetic freeze-out. Each of these parts are described in the paragraphs below.

The description of the nuclei before the collision depends on an understanding of the distribution of nucleons in the nuclei. This distribution may be described using a Glauber Monte Carlo, which is discussed in more detail in Chapter 4. The next step to

¹At top RHIC energies the beams are maintained in RHIC's rings for an average of 8 hours during which time each ion circles the ring two billion times, traveling $8.6 \cdot 10^{12} m$, the equivalent of following the Earth's orbit around the sun 9 times in those 8 hours. This accomplishment is similar to firing a beam twice the distance from the sun to Neptune guided by magnetic fields in a beam pipe, and having it hit a target half a centimeter wide.

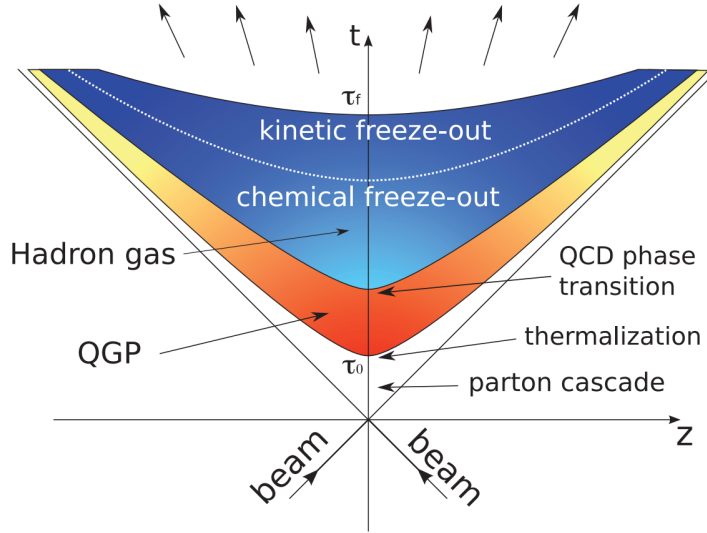


FIGURE 1.1 The stages of heavy-ion collisions at sufficiently high $\sqrt{s_{\text{NN}}}$ to form a QGP [5].

describing the nucleus before the collision is determining the probabilities of different partons interacting and what fraction of a nucleon's momentum they carry going into an interaction depending on momentum transfer (Q^2). Deep inelastic scattering (DIS) experiments of electron beams onto proton targets have constrained the parton distribution functions (PDFs) of valance quarks, sea quarks, and gluons in protons (see Fig. 1.2) [6]. Similar DIS experiments with heavy-ions have constrained the nuclear PDFs (nPDFs). The nuclear modification to PDFs is shown by the ratio of a nPDF to a PDF as shown in Fig. 1.3 [7] and described in the next paragraph.

Each parton in a proton or neutron carries a fraction of that nucleon's momentum (x). PDFs describe the probability for a parton to have a particular x for a given Q^2 . Each type of parton has a different PDF with gluons dominating at low x , while valance quarks dominate near $x = 1/3$ for protons and neutrons, as can be seen in Fig. 1.2 [6–9]. The physics that leads to nPDFs being enhanced or suppressed at various x , relative to proton PDFs, modify the probability of scatterings occurring that would produce mid-rapidity partons with particular momenta. nPDFs are suppressed (< 1) for $x < \approx 0.03$. This suppression is attributed to nuclear “shadowing”. Then nPDFs are enhanced for ≈ 0.03

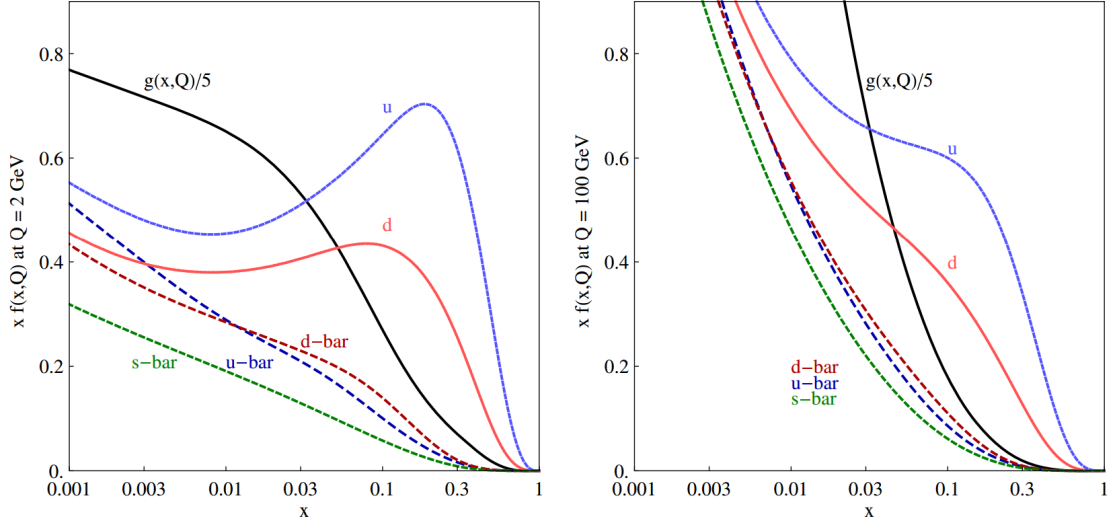


FIGURE 1.2 Proton next to next to leading order (NNLO) PDF from CTEQ-TEA for gluons, the two valence up quarks, the valence down quark, and sea quarks. The PDFs are shown for $Q = 2 \text{ GeV}$ and $Q = 100 \text{ GeV}$ [6].

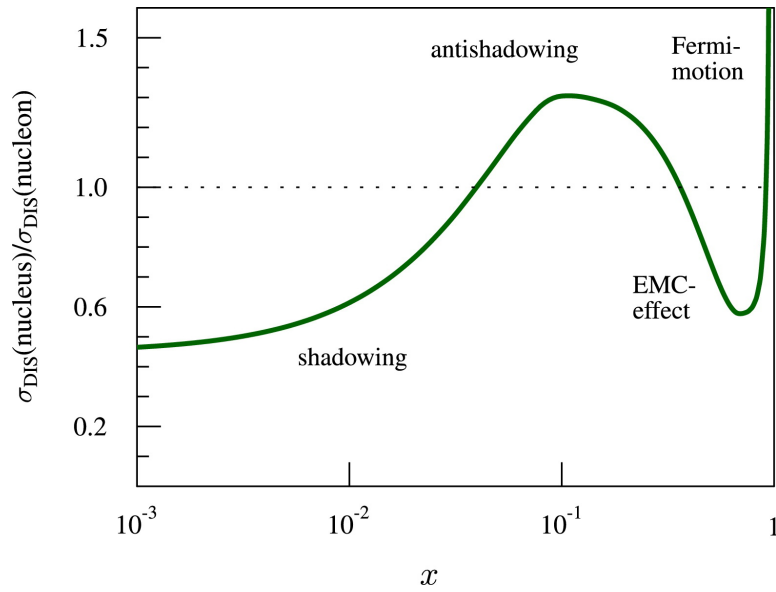


FIGURE 1.3 An example of the typical nuclear modification of a PDF from DIS measurements. The characteristic ordering of the shadowing, anti-shadowing, EMC effect, and Fermi motion regions are labeled [7].

$< x < \approx 0.3$ due to “anti-shadowing”, suppressed from $\approx 0.3 < x < \approx 0.8$ due to the “EMC effect”, and enhanced for $x > \approx 0.8$ due to fermi motion. While explanations for the features of nPDFs have not been agreed upon, some features are better understood than others. Shadowing may be due to the high-cross-section, low- x , interactions in the leading portion of a colliding nucleus reducing the probability of similar interaction in the trailing portion [10] or it may be due to parton recombination resulting from multi-nucleon correlations [11]. For Fermi motion, the PDF in the denominator is a steeply falling function with a maximum range of $x = 1$. However, the nucleons bound in a nucleus have finite momenta relative to the nuclear mean so that the x values of their constituent partons are smeared and can have values greater than 1. Hence the enhancement seen at high x is the result of the denominator going to zero faster than the numerator. Anti-shadowing may have contributions from the same coherent interactions at low x that contribute to shadowing [11]. That is, several coherent interactions at low x may mimic a higher x interaction. The EMC effect may be due to a reduced effective nucleon mass or it may be due to an increase of the quark confinement size in nuclear matter [12].

The next stage of the collision is the collision of the Lorentz contracted nuclei. As the nuclei overlap, individual partons from the nucleons in the nuclei interact with each other. High momentum transfer (Q^2) interactions are well described by perturbative quantum chromodynamics (pQCD), but lower Q^2 interactions are non-perturbative. pQCD would treat each initial hard scattering incoherently, but this model breaks down at low Q^2 where interaction cross-sections are higher, as well as for subsequent scatterings and thermalization that occur during the pre-equilibrium phase [13]. High- Q^2 -processes lead to the production of hard probes. They are called “hard” because they are produced with high Q^2 and “probes” because they form before QGP and may be used as an external probe of QGP properties. They may be calibrated by measuring them in a reference system where a QGP is unlikely to be produced, such as $p+p$ or peripheral $A + A$ collisions. Hard probes include high transverse momentum (p_T) partons and heavy quark-anti-quark pairs. High- p_T partons carry color charge and interact through

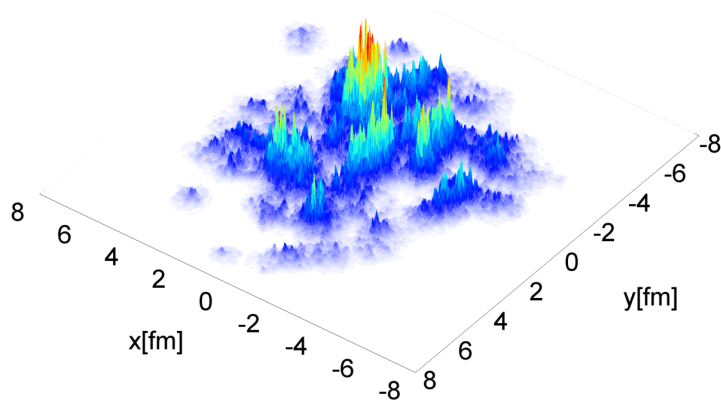


FIGURE 1.4 The initial energy density distribution in the transverse plane generated for a small impact parameter heavy-ion collision using the IP-Glasma model [16].

the strong interaction with the QGP. For heavy quarks, there are charm and bottom quarks which can bind with their anti-particles when they are produced forming bound mesonic states collectively called quarkonia. Their varying mass and binding energy leads to varying size which leads to a varying degree of color screening such that different types of quarkonia are more or less sensitive to QGP [14, 15].

While high- Q^2 interactions are well described by pQCD, low- Q^2 interactions in QCD are non-perturbative and can not be solved exactly. Several approaches to describing the low- Q^2 regime have been developed and this is still an active research field. Examples include boson exchange models and QCD effective kinetic theory (EKT) which includes $1 \rightarrow 2$ splittings in addition to hard $2 \rightarrow 2$ scatterings [17, 18]. These parton cascades may continue until $1 \rightarrow 2$ processes are balanced by $2 \rightarrow 1$ processes, up to a saturation scale described by the Color Glass Condensate model [19]. The IP-Glasma gives initial conditions for heavy-ion collisions by combining impact parameter dependent saturation with a Yang-Mills description of initial Glasma fields with fluctuations in both the transverse and the longitudinal energy deposition as seen in Fig. 1.4 [16, 20]. This pre-equilibrium phase of heavy-ion collisions is perhaps the least well described and understood part of heavy-ion collisions.

The parton cascade increases the number of partons in the pre-equilibrium medium which shortens their mean free path. After each parton has undergone several interactions the various regions of the medium will approach local equilibrium and thermalization [13]. At this point a near-equilibrium QGP can be well described using hydrodynamics [21] or with lattice QCD calculations [22]. The hard probes discussed above would interact with this medium. Fluctuations in the distributions of interacting partons drive initial anisotropies that may be washed out to some degree during the pre-equilibrium phase, but have been found to still be significant. Models that do not include event-by-event spatial anisotropies in their initial conditions and do not run event-by-event hydrodynamics have been found to do a poor job at describing the data [23]. The initial spatial anisotropies lead to pressure gradients which give larger momentum boosts in the direction of steeper gradients to partons in the QGP. The study of this “flow” is very active with many observables developed that have differing degrees of sensitivity to the QGP relative to other phases of the collision [21, 24–32]. Some of these will be discussed in the next section. As the QGP expands it cools, until at a critical temperature that varies with the baryon chemical potential (μ_B) the system hadronizes².

Over the course of the system’s evolution many quark-anti-quark pairs are produced along with many gluons. Lattice tells us that when the medium’s temperature drops below T_C the colored partons that make up the QGP must hadronize. That is, they must combine into groups that have no net color charge. At high p_T this is well modeled by fragmentation and modifications to fragmentation observables from their vacuum values may be taken as being due to the presence of a medium during or before the fragmentation process. It may be that when the phase space density is sufficiently high, co-moving partons hadronize by coalescing rather than through the fragmentation process. This means that much of the bulk in a central heavy-ion collision may hadronize through coalescence, hence the full momentum distribution of hadrons should be described by a combination of modified fragmentation and coalescence while also accounting for feed-down from weak decays as in Fig. 1.5 [34]. The Hubble-like expansion driven by the

²For $\mu_B = 0$ the critical temperature (T_C) is $T_C \approx 155$ MeV [22, 33].

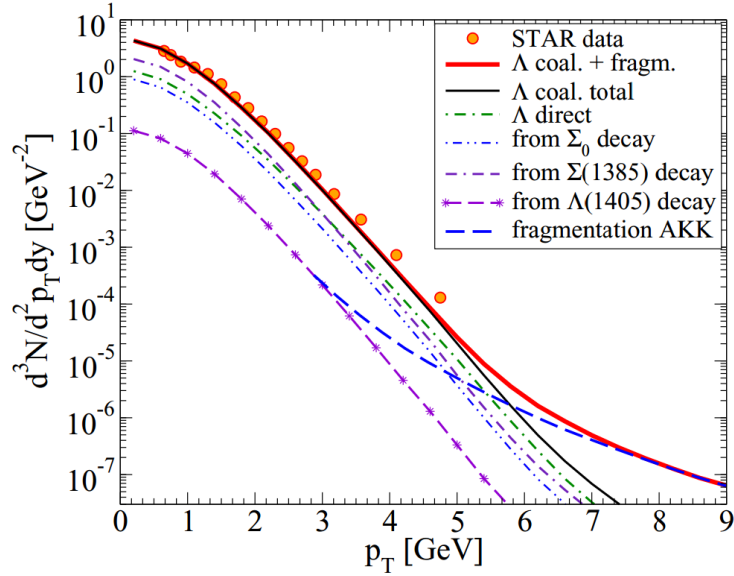


FIGURE 1.5 0-10% λ spectra from STAR at $\sqrt{s_{NN}} = 200$ GeV described by a model including fragmentation, coalescence, and weak decay feed-down [34].

pressure gradients in the partonic phase leads to a radial flow that must be included by theorists in order to describe the data, as shown in Fig. 1.6 [34].

After hadronization the system is described as a hadron gas. Interactions continue as the system continues to expand and cool. When inelastic collisions cease the particle ratios are fixed. This is called chemical freezeout. Next, when elastic collisions stop the system is said to undergo thermal freezeout. Statistical thermal model fits to the particle ratios are used to describe the temperature and baryon chemical potential at chemical freezeout. Fits to the p_T spectra give the temperature at kinetic freezeout. After kinetic freezeout the hadrons stream to the detectors with some fraction of the hadrons decaying such that only their daughters are detected.

With all of these different stages of the collision effecting particle production and kinematics it becomes important for the investigation of QGP to construct observables that are maximally sensitive to the QGP and minimally sensitive to the other phases. These observable can provide signatures of QGP formation.

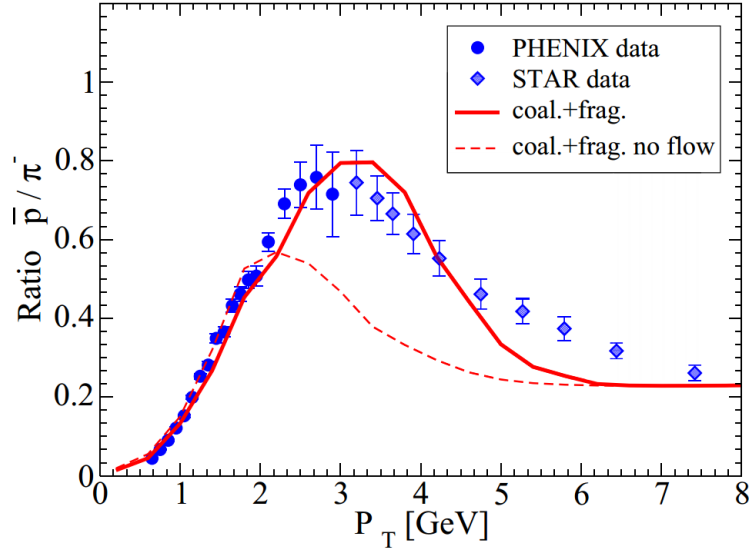


FIGURE 1.6 Antiproton to negative pion ratio from STAR and PHENIX in 0-10% at $\sqrt{s_{NN}} = 200$ GeV described by a model including fragmentation, coalescence, and weak feed-down and radial flow for the solid red curve [34].

1.1.2 Signatures of Quark Gluon Plasma

The signatures of QGP formation primarily come from two sources: Hard probes and the bulk. The bulk is the collection of low momentum particles that form a near perfect fluid and whose evolution may be described using hydrodynamics [13]. Hard probes are the high momentum transfer (Q^2) particles that are formed prior to the bulk and then interact with it. Most evidence for the QGP from bulk signatures is obtained by investigating correlations among the many low momentum particles generated in a collision and trying to determine whether those correlations can be generated with understood physics and without invoking a QGP phase. The large azimuthal anisotropies discovered at the relativistic heavy ion collider (RHIC) imply a liquid phase occurs early in the collision in order to convert the spatial anisotropies of the initial scattering system into the momentum anisotropies that are ultimately measured [35].

An important tool for describing correlation structures in heavy-ion collisions is the Fourier decomposition of azimuthal distributions³ of particle correlations as shown in

³These distributions describe the correlations of particles to the reaction plane; the plane defined by the beam axis and a line between the centers of the nuclei.

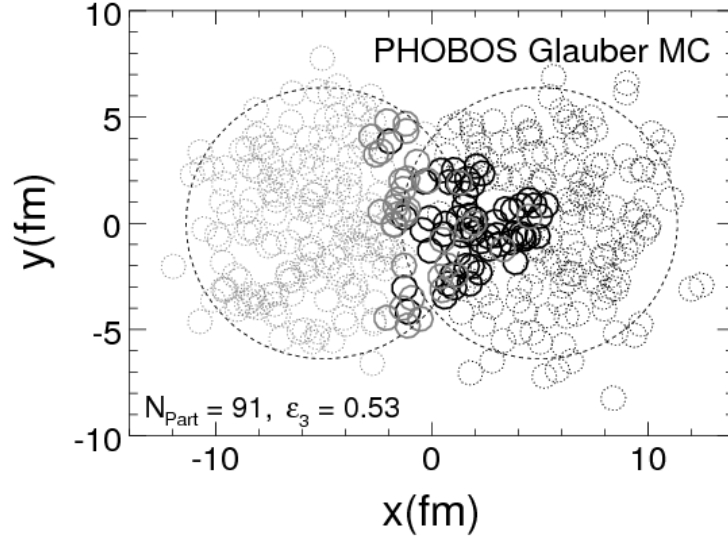


FIGURE 1.7 A Glauber Monte Carlo simulation of a mid-peripheral Au+Au collision at $\sqrt{s_{NN}} = 200$ GeV with a fluctuation driven triangular distribution of participating nucleons [37].

[36]. While it was once thought that the even terms in this decomposition could be generated from the almond overlap shape alone and that the odd terms would be zero, it has been shown that fluctuations in the initial geometry contribute to the even terms and drive non-zero odd terms as illustrated in Fig. 1.7 [37]. Higher orders in the Fourier decomposition become increasingly suppressed as viscosity is increased and so they serve as sensitive probes of the viscosity at early times [24]. Signatures of QGP formation from the bulk have been measured for many $\sqrt{s_{NN}}$. The focus of this thesis is to use hard probes to provide independent evidence for QGP formation and to determine the lowest $\sqrt{s_{NN}}$ for which hard probes provide evidence of QGP formation.

Hard probes are generated before QGP formation and then interact with the produced medium. A sensitive probe should be well calibrated, sensitive to the QGP phase, and unaffected by other phases of the collision. Photons, heavy flavor particle production, and high momentum partons are examples of hard probes, each with differing degrees of sensitivity to QGP as well as to the other stages of the collision's evolution.

The QGP is transparent to photons and so they provide a reference for particle production unaffected by the medium. However the medium itself produces thermal photons at low momentum that form a background to the photons produced in initial hard scatterings [38]. In addition, photons are generated from hadronic decays and fragmentation processes forming a background that makes it experimentally difficult to identify exclusively those photons that were emitted in the early, hard scattering, phase of the collision. Because it is so difficult to separate the photons of interest from the background at low p_T , this analysis would be very difficult at low- $\sqrt{s_{NN}}$.

Heavy quarks, those quarks that are more massive than the strange quark are less likely to be formed from in-medium thermal radiation due to their masses⁴. Most of these particles are therefore formed prior to the formation of the QGP and probe its entire evolution. They are expected to have a mass dependence to the strength of their interactions with the medium [40]: At low momentum they are expected to get less of a boost from the expanding medium, and at high momentum they are expected to lose less energy. While radiative energy loss was thought to dominate and heavy quarks were expected to lose less energy due to the dead-cone effect, measurements have not consistently born this out [41]. However, these probes are seldom made at low $\sqrt{s_{NN}}$ and so their energy dependence is difficult to measure.

The most promising probe produced in sufficient numbers at low $\sqrt{s_{NN}}$ are high momentum light quarks; up, down, and strange. They are the hard probes that are studied in this dissertation. As high transverse momentum (p_T) partons traverse the medium they interact and undergo collisional and radiative energy-loss [41, 43]. Partonic energy loss depletes the number of high- p_T final state hadrons relative to a system where a medium is not produced. In order to produce such a reference, one can collide protons with each other with the expectation that the system would be too small to produce an extensive medium. Then a Glauber Monte Carlo may be used to estimate the number of $p+p$ -like collisions that occur in the Au+Au collision system (N_{bin}) and use it to scale the $p+p$ reference. Glauber Monte Carlos are described in more detail in chapter 4 and

⁴The charm mass is $\approx 1.25 GeV/c^2$ while the temperature of the medium is initially $\approx 0.34 GeV$ [39]

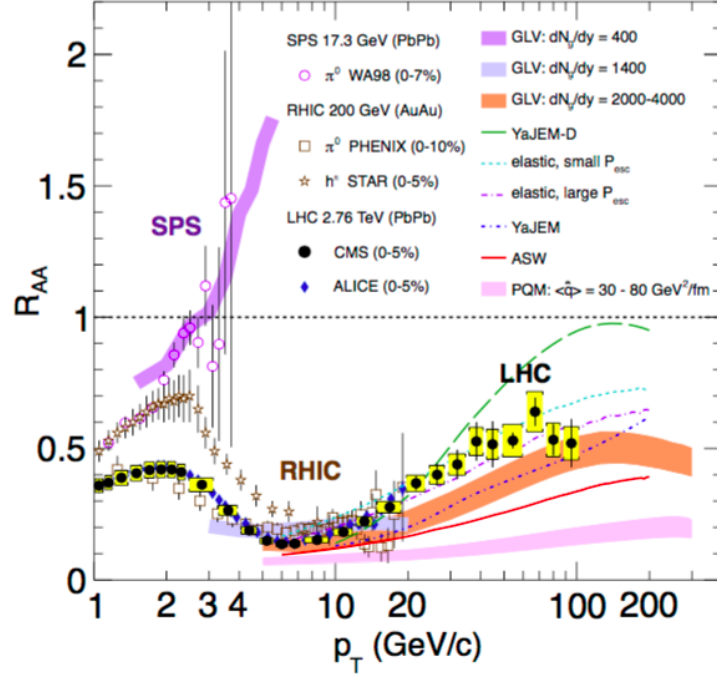


FIGURE 1.8 The nuclear modification factor, R_{AA} , for π^0 and h^\pm for $\sqrt{s_{NN}} = 17.3$ GeV - 2.76 TeV [42].

in [44]. They arrange nucleons randomly within Woods Saxon potentials to construct nuclei and then overlap two such nuclei with some impact parameter. Then they use proton-proton cross sections to determine the distributions of interacting nucleons. The nuclear modification factor, R_{AA} , can then be constructed as:

$$R_{AA} = \frac{1}{\langle N_{\text{bin}} \rangle_{\text{Au+Au}}} \frac{\left(\frac{d^2 N}{dp_T d\eta} \right)_{\text{Au+Au}}}{\left(\frac{d^2 N}{dp_T d\eta} \right)_{\text{p+p}}}. \quad (1.1)$$

Some of the world's R_{AA} for central, small impact parameter⁵, spectra are shown in Fig. 1.8 [42]. This analysis requires that $p+p$ collisions be conducted at every collision energy that heavy-ion collisions are conducted at in order to provide reference systems. This greatly increases the beam time and reduces the heavy-ion data totals. An alternative reference system for the nuclear modification factor is peripheral, large impact

⁵The impact parameter is the distance of closest approach between the nuclei if the nuclei were to travel along straight lines.

parameter, heavy-ion collisions that have a small overlap area and relatively few $p+p$ -like binary collisions. Any produced media should still be smaller and shorter lived on average than they would be in central, small impact parameter, heavy ion collisions. Since in this procedure the scaled central spectra are compared to the scaled peripheral spectra, the mathematical description becomes

$$R_{\text{CP}} = \frac{\langle N_{\text{bin}} \rangle_{\text{Peripheral}} \left(\frac{d^2 N}{dp_{\text{T}} d\eta} \right)_{\text{Central}}}{\langle N_{\text{bin}} \rangle_{\text{Central}} \left(\frac{d^2 N}{dp_{\text{T}} d\eta} \right)_{\text{Peripheral}}}. \quad (1.2)$$

The advantage of this observable is that the reference data is taken concurrently with the data of primary interest. It was shown for $\sqrt{s_{\text{NN}}} = 200$ GeV that the ratio of scaled peripheral spectra to $p+p$ spectra was close to unity for $p_{\text{T}} > 2$ GeV/c [45].

A challenge that most analyses in this field face is that the particles that are finally measured in detectors are often affected by physical processes from stages of the collision both before and after QGP formation. Also, the process by which the colored partons form into colorless hadrons, hadronization, may vary depending on partonic phase space density⁶. Several of these physical processes work to conceal the QGP signature of partonic energy-loss that would otherwise be seen as high- p_{T} suppression of charged hadron production (*i.e.* $R_{\text{CP}} < 1$). These processes include p_{T} broadening, radial flow, and variation in the relative contribution to hadronization from fragmentation and coalescence. p_{T} broadening is caused by multiple scattering. A steeply falling spectrum of particles where the particles underwent more scatterings will shift some of the particles from low p_{T} bins with many particles to higher p_{T} bins where there are fewer particles. Taking the ratio of the broadened spectra to the reference would then show an enhancement at high p_{T} . A feature of hydrodynamic descriptions of the partonic phase is that the pressure gradients from the center of the overlap region to the edge will drive a hubble-like expansion called radial flow. Figure 1.6 [34] demonstrates the importance of including radial flow for describing p_{T} spectra. Finally, coalescence is expected to dominate at

⁶Partonic phase space density is a measure of the number of partons per unit volume in position space as well as per unit volume in momentum space. High phase space density means more co-moving partons and a higher probability for them to coalesce [34].

low p_T for central collisions due to the relatively high partonic phase space density in these high multiplicity collisions, as seen in Fig. 1.5 [34]. However, as you go more peripheral the phase space density is reduced and more final state particles in each p_T bin will have originated from the fragmentation of a higher momentum parton rather than the coalescence of several lower momentum partons. This means that central collisions will have an enhancement of hadrons at high- to mid- p_T relative to the fragmentation dominated peripheral collisions. While the enhancement due to coalescence would be the result of having produced a partonic medium, the other sources of enhancement to p_T -spectra make it difficult to use this as a model independent QGP signature.

1.2 Beam Energy Scans

Over time, particle accelerators have been constructed that achieve higher and higher collision energies ($\sqrt{s_{NN}}$) for heavy ions. Detectors at these various facilities had a range of capabilities and focused on different physics so that looking at the $\sqrt{s_{NN}}$ dependence of QGP observables is difficult with existing data. This motivated the RHIC Beam Energy Scan (BES) as a way to use a general purpose detector to measure the $\sqrt{s_{NN}}$ dependence of a range of observables with a common acceptance and detector capability. The interest in the BES was in demonstrating that observables for QGP production would “turn off” at sufficiently low energies, as well as the search for a possible critical point and first order phase transition in the phase diagram of nuclear matter. A sample phase diagram is shown in Fig. 1.9 [46]. Here you see that ordinary atomic nuclei exist at relatively low temperature, on the x-axis here and at a particular baryon density. Moving up the y-axis we see a phase transition at low baryon density that is well described by Lattice QCD as a cross-over transition [22]. High- $\sqrt{s_{NN}}$ collisions create media with low baryon density that evolve through the region of the phase diagram near the y-axis. However, as the collision energy is reduced the produced media are formed and evolve at higher net baryon densities.

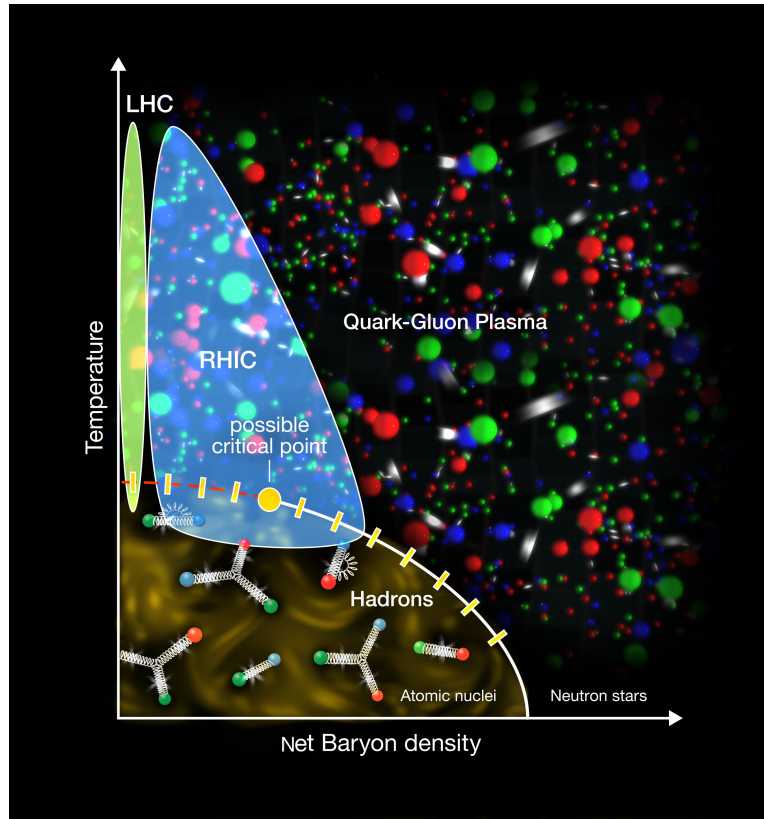


FIGURE 1.9 The nuclear phase diagram with the regions that are accessible at the large hadron collider (LHC) and RHIC highlighted [46].

It has been proposed that there may be a first order phase transition between hadronic and partonic matter at sufficiently high net baryon density, which would imply the existence of a critical endpoint. The RHIC BES and its future second phase, BES II, will determine whether such a critical point exists in the region of the phase diagram accessible by heavy-ion collisions. Even if the critical point exists at an inaccessible baryon chemical potential, the data may still determine the location of the critical point if the properties of the produced media, such as their finite size and lifetimes, can be properly exploited [47]. Phase diagrams such as Fig. 1.9 are for equilibrated, infinite systems. Models that describe finite-time-finite-size scaling account for the fact that heavy-ion collisions do not form infinitely large and infinitely long lived systems. Employing such models facilitate more than trying to describe the collision system more accurately though. They can be used to fix the scaling exponents which can then be

used to determine the location of the critical point in the phase diagram as was done in [47, 48]. This model may need to be expanded to take into account pre-equilibrium and hadronic effects as well as medium shape dependence due to the different centrality classes employed in the scaling, but it already does well at scaling the data with a common set of exponents within a single model for two different sets of observables.

The aim of this dissertation is to measure the $\sqrt{s_{\text{NN}}}$ dependence of R_{CP} so as to explore whether the dominance of high- p_{T} suppression effects measured at $\sqrt{s_{\text{NN}}} = 200$ GeV weakens and is overwhelmed by enhancement effects at sufficiently low $\sqrt{s_{\text{NN}}}$. Next, using a procedure developed here, the centrality dependence of the N_{bin} -scaled high- p_{T} yield will be used to partially disentangle enhancement and suppression effects in order to provide evidence for partonic energy loss at lower $\sqrt{s_{\text{NN}}}$ than would be possible with R_{CP} alone. To this end, chapter 2 provides an overview of the analysis method, including a description of the Glauber Monte Carlo and the details of the data observables included in this dissertation. RHIC and the STAR detector will be described in chapter 3. Then chapter 4 will provide an overview of quality assurance techniques. Chapter 5 describes the correction procedures used to account for detector effects on the final observables. The systematic uncertainty analysis is shown in chapter 6 and the results in chapter 7. Discussions of the results appear in chapter 8. Chapter 9 will provide comparisons to several Monte Carlo event generators that rely on different models of the underlying physics in heavy-ion collisions. Chapter 10 will provide conclusions and an outlook of future directions for beam energy scan physics relating to partonic energy loss.

Chapter 2

Nuclear Modification of High- p_T Probes

One way to measure the effects of a QGP on a probe is to compare data from a system where a QGP is likely to be formed to a baseline where a QGP is unlikely to be formed. Possible baselines include $p+p$ collisions and peripheral Au+Au collisions. In order to scale between the $p+p$ or peripheral Au+Au data and central Au+Au, it is useful to model Au+Au collisions as N_{bin} distinct $p+p$ -like collisions. N_{bin} is estimated here using a Glauber Monte Carlo simulation, as described in Section 2.1.

A Glauber Monte Carlo simulation can be used to describe the relationship between the impact parameter, b , and N_{bin} ; as well as the number of participating nucleons, N_{part} . It can also be used to map between these values and centrality classes, experimentally defined divisions of the data which in STAR are determined by matching the 5% highest mid-rapidity multiplicity events to the 5% highest N_{part} collisions and calling it 0-5% centrality, and so forth for each of the other centrality classes. Centrality definitions depend on the efficiency of triggering on and reconstructing events. Since the trigger and vertex reconstruction efficiencies get worse for more peripheral collisions, a correction must be applied to re-weight the reconstructed events by their event reconstruction

efficiencies before this mapping occurs. This procedure is described in more detail in section 2.2.

Once the events' centrality classes are determined with estimates for their N_{part} and N_{bin} values, detector-level p_T spectra from each centrality and $\sqrt{s_{\text{NN}}}$ can be determined, as described in section 2.3.

Similar Glauber Monte Carlo simulations can provide the mean N_{bin} values for collisions of deuterons with gold ($d+\text{Au}$). The ratio of N_{bin} -scaled spectra from $d+\text{Au}$ collisions to those from $p+p$ collisions is R_{dAu} , a nuclear modification factor defined as

$$R_{\text{dAu}} = \frac{1}{\langle N_{\text{bin}} \rangle_{d+\text{Au}}} \frac{(\frac{d^2 N}{dp_T d\eta})_{d+\text{Au}}}{(\frac{d^2 N}{dp_T d\eta})_{p+p}}. \quad (2.1)$$

Published results from $\sqrt{s_{\text{NN}}} = 200 \text{ GeV}$ for this observable are discussed in section 2.4.

The ratio of N_{bin} -scaled spectra from central collisions to those from peripheral collision is R_{CP} , a nuclear modification defined by Eq. 1.2. R_{CP} is discussed further in section 2.5.

R_{CP} describes the overall, or net, modification from peripheral to central collisions. A new observable is developed in Section 2.6 called Y that shows the evolution with centrality of the N_{bin} scaled high- p_T yields. This centrality differential method of characterizing the nuclear modification of high- p_T probes may disentangle enhancement effects that increase quickly with centrality before saturating from partonic energy loss which continues to increase with increasing centrality even for the most central collisions. Using Y to describe the nuclear modification of probes may provide evidence of medium induced parton energy loss down to lower $\sqrt{s_{\text{NN}}}$ than R_{CP} , as described in more detail in section 2.6.

2.1 Glauber Monte Carlo

Heavy-ion collisions can be modeled as N_{bin} independent $p+p$ -like collisions, but this model works best for rare probes like high- Q^2 interactions which are little effected by having a nucleon interact with more than one other nucleon over the course of a heavy-ion collision. This means that the initial high- p_T parton production is expected to scale with N_{bin} . Low- Q^2 processes are instead expected to scale with the number of participating nucleons, N_{part} because having one such interaction for a particular nucleon depletes the probability of that nucleon having another such interaction.

Each recorded event at STAR may be characterized by the number of good quality detector-level charged particles associated with the primary vertex and measured in $|y| < 0.5$. STAR calls this quantity *refMult*. Centrality bins are defined by taking the 5% highest *refMult* events and calling that the 0-5% centrality bin, and so forth for the other centrality bins. In order to estimate the $\langle N_{\text{bin}} \rangle$ and $\langle N_{\text{part}} \rangle$ values for each centrality bin, a Glauber Monte Carlo simulation is employed [44]. The Glauber model is used to describe the positions of nucleons within nuclei for many different simulated collisions. The Glauber model describes the nuclei before the collision, the initial state, by placing their nucleons in random positions within a Woods-Saxon potential¹, using the $p+p$ cross-section for that collision energy² to determine the size of the nucleons. Two nuclei are fashioned in this way and then overlapped with a randomly determined impact parameter, as in Fig. 1.7 [37]. The number of nucleons from each nucleus that overlap nucleons from the other nucleus are counted in order to determine N_{part} and N_{bin} for that collision. This procedure is repeated many times to simulate the initial conditions of many events so that $\langle N_{\text{part}} \rangle$ and mean $\langle N_{\text{bin}} \rangle$ for each centrality class may be determined.

Systematic uncertainties due to model assumptions are accounted for with the systematic uncertainties for $\langle N_{\text{part}} \rangle$ and $\langle N_{\text{bin}} \rangle$ within each centrality bin. For STAR, these

¹The model currently used by STAR does not differentiate neutrons from protons.

²Details of the Glauber Monte Carlo parameters are listed in Appendix A.

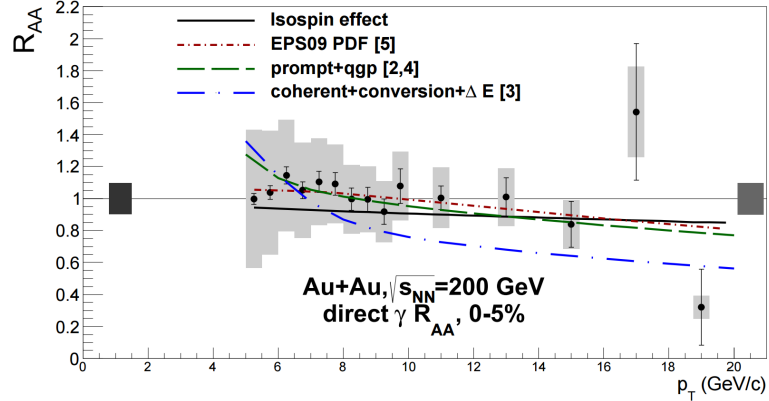


FIGURE 2.1 Direct photon R_{AA} measured by PHENIX for 0-5% centrality in $\sqrt{s_{NN}} = 200$ GeV [49].

uncertainties are dominated by an uncertainty in the combined trigger efficiency and vertex reconstruction efficiency in peripheral collisions.

Validation of N_{bin} scaling for hard processes is provided by the measured direct photon R_{AA} , as in Fig. 2.1 [49]. Photons, a colorless probe, are not expected to undergo modification in the colored medium. The lack of modification for photons passing through a QGP means that direct photon R_{AA} can be used to test whether the N_{bin} values obtained from Glauber Monte Carlo simulations are accurate. Small modifications due to modification of the nPDF would be expected, but the errors in this measurement are too large to resolve such small effects. Similar measurements at the LHC with photons, and with W and Z bosons, also found that N_{bin} scaling holds [50].

2.2 Trigger and Vertex Reconstruction Efficiency

Large impact parameter heavy-ion collisions have fewer produced particles and are less likely to satisfy the conditions to fire the minimum bias trigger. Having fewer tracks also reduces the likelihood of the primary vertex being reconstructed. These combined inefficiencies reduce the number of reconstructed peripheral collisions in data from the Glauber Monte Carlo expectation, as shown in Fig. 2.2 [51]. A ratio is constructed with

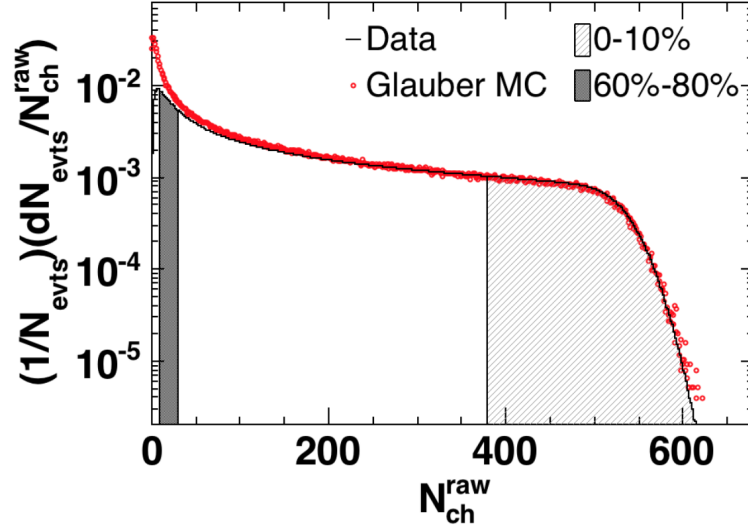


FIGURE 2.2 STAR detector level charged multiplicity in $|\eta| < 0.5$ for data compared to Glauber Monte Carlo expectation for $\sqrt{s_{NN}} = 200$ GeV [51].

a fit to the data for the numerator and the Glauber Monte Carlo expectation for the denominator. This gives the combined trigger and vertex reconstruction efficiency. There is also a bias introduced for collisions with large displacements in the beam direction, $|Z_{vertex}|$. Due to anisotropies in the detector performance, vertices displaced from the center of the detector have more or fewer reconstructed tracks than average. The (η, V_Z) track distribution is shown in Fig. 2.3. It demonstrates that vertices reconstructed at high positive V_Z consist of more tracks on average than vertices reconstructed with highly negative V_Z values. This vertex position bias in the multiplicity determination is measured and corrected for in STAR analyses in order to have a consistent measure of centrality. The corrected multiplicity will be called $Mult$ for the remainder of this thesis.

2.3 Spectra

p_T spectra form the core measurement for all of the derived observables in this dissertation. This chapter outlines how the detector level data were collected and the next

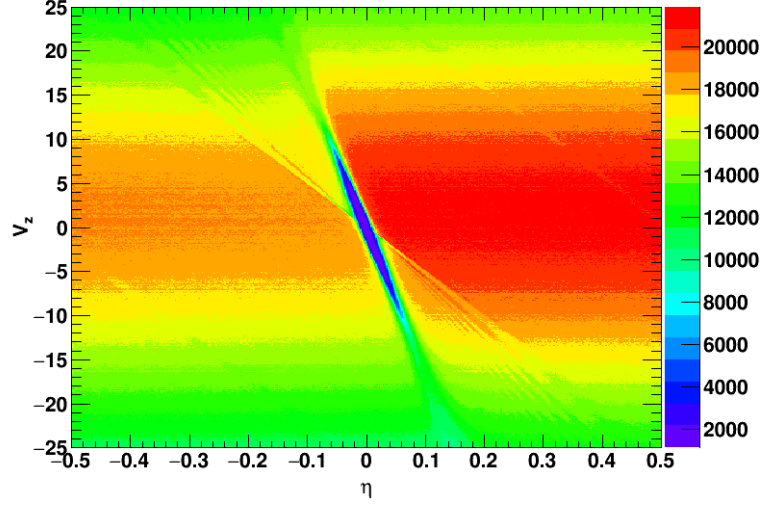


FIGURE 2.3 STAR detector level charged tracks reconstructed in each $(|\eta|, V_Z)$ bin at $\sqrt{s_{NN}} = 7.7$ GeV.

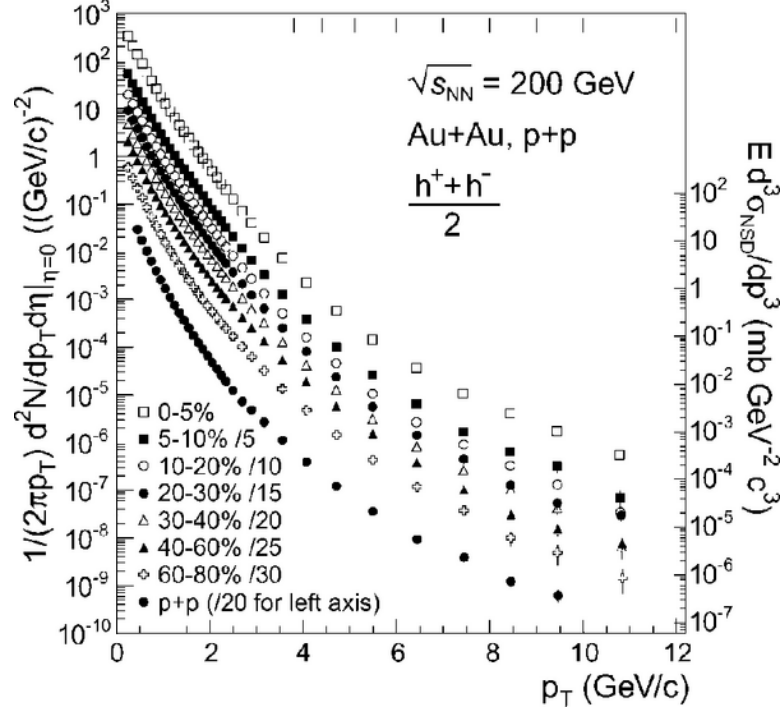


FIGURE 2.4 Fully corrected charged hadron p_T spectra from $p+p$ collisions and several centralities of Au+Au at $\sqrt{s_{NN}} = 200$ GeV [45].

chapter will detail the corrections for detector efficiency and other effects. Data are collected for each $\sqrt{s_{NN}}$ and centrality as a function of p_T in an interval $|\eta| < 0.5$ and weighted to obtain

$$p_T \text{ spectra} \equiv \frac{1}{2\pi p_T} \frac{d^2 N}{d\eta dp_T}. \quad (2.2)$$

After corrections are applied (see Chapter 5), such spectra may be fit by a decaying exponential at low p_T and low $\sqrt{s_{NN}}$, but is typically fit with a power law at higher p_T and $\sqrt{s_{NN}}$ [52]. Better fits are achieved with blastwave fits that take the low- p_T radial flow into account [52]. Figure 2.4 shows published spectra for $\sqrt{s_{NN}} = 200$ GeV Au+Au and $p+p$ data [45] as an example. Such spectra may then be scaled by N_{bin} and compared to each other using R_{CP} and Y , as discussed in the next two sections.

2.4 R_{dAu}

While Au+Au collisions may produce QGP, it is important to verify that observed modification from $p+p$ data is the result of interactions in QGP and not interactions with a cold nucleus. Asymmetric collisions of protons or deuterons with a heavy nuclei are unlikely to produce QGP in the way that heavy-ion collisions do so that any modification from $p+p$ collisions would be due to cold nuclear matter (CNM) effects. The nuclear modification factor, R_{dAu} (Eq. 2.1), shows how much net modification there is for $d+Au$ spectra relative to $p+p$ spectra as a function of p_T . R_{dAu} uses N_{bin} scaling so that if there is no net nuclear modification of $d+Au$ spectra relative to $p+p$ spectra, R_{dAu} equates to unity. Different centrality bins may be determined from event activity and $\langle N_{\text{bin}} \rangle$ values estimated from a Glauber Monte Carlo simulation.

Figure 2.5 shows R_{dAu} for $\sqrt{s_{NN}} = 200$ GeV for inclusive centrality as well as the 0-20% most central events, and for pions and protons as well as charged hadrons [53]. There is significant enhancement for $2 < p_T < 7$ GeV/c for minimum bias³ produced charged hadrons. Protons are more enhanced than pions and particles from the 0-20% highest

³Minimum bias means that the data samples as much of the non-single-diffractive cross section as possible without preferentially selecting certain types of collisions.

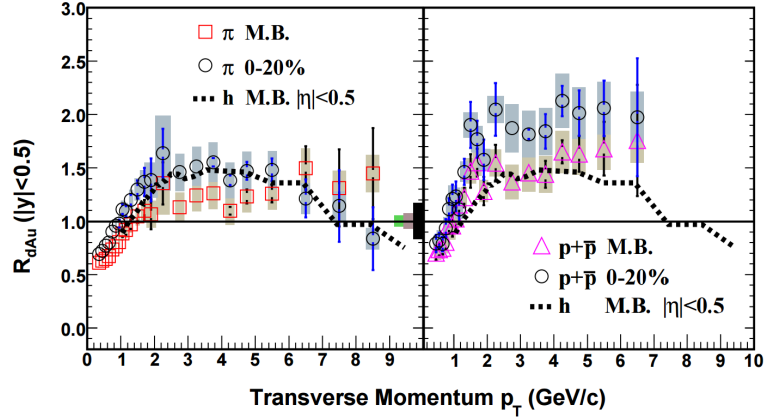


FIGURE 2.5 Fully corrected pion, proton, and charged hadron R_{dAu} at $\sqrt{s_{NN}} = 200$ GeV for minimum bias as well as 0-20% collisions[53].

activity collisions are more enhanced than those from minimum bias collisions. Previous measurements by Cronin *et al.* of asymmetric collisions at lower $\sqrt{s_{NN}}$ also found these effects and so the measured enhancement has come to be called the ‘‘Cronin effect’’ or ‘‘Cronin enhancement’’ [54–56]. These CNM enhancement effects are the result of having a single heavy ion in the collision. Systems with two heavy ions would likely have stronger CNM enhancement effects [57, 58]. If this enhancement is due to p_T -broadening, then the enhancement would be stronger for steeper spectra. Suppression effects in heavy-ion collisions would have to be stronger than CNM enhancement effects in order to result in net suppression in R_{AA} or R_{CP} .

2.5 R_{CP}

The nuclear modification factor, R_{CP} (Eq. 1.2), shows how much net modification there is for central spectra relative to peripheral spectra as a function of p_T . R_{CP} uses N_{bin} scaling so that if there is no net nuclear modification of central spectra relative to peripheral spectra then R_{CP} would be unity. This is based off the assumption that the high- Q^2 part of Au+Au collisions may be modeled as N_{bin} independent incoherent $p+p$ -like collisions. Different centrality bins may be chosen for the central and peripheral

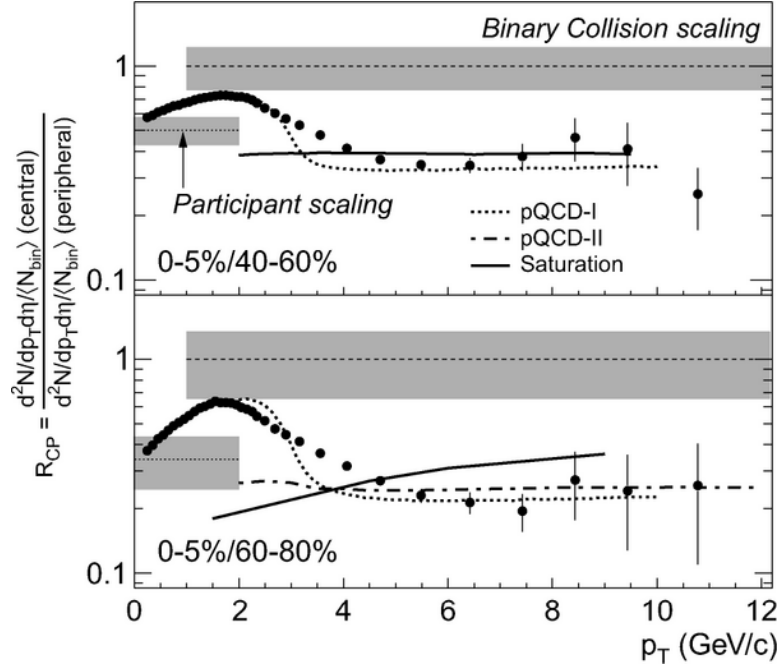


FIGURE 2.6 Fully corrected charged hadron R_{CP} at $\sqrt{s_{NN}} = 200$ GeV with two different peripheral reference centralities [45].

spectra. The most central spectra are expected to be subject to the most modification, and the most peripheral spectra are expected to be the most $p+p$ -like.

Sample fully corrected R_{CP} results are shown in Fig. 2.6 for $\sqrt{s_{NN}} = 200$ GeV with two different peripheral bins for the reference [45]. The 60-80% centrality class was found to have little net high- p_T nuclear modification from a $p+p$ baseline, as shown in Fig. 2.7 [45]. There may still have been some high- p_T suppression, but if so this was countered by enhancement effects. While unmodified high- p_T hadrons are expected to exhibit N_{bin} scaling, the less rare particles at very low- p_T are expected to scale with N_{part} . The theory curves correspond to pQCD calculations, with or without shadowing and Cronin effects included, as well as an extension of a saturation model to high momentum transfer.

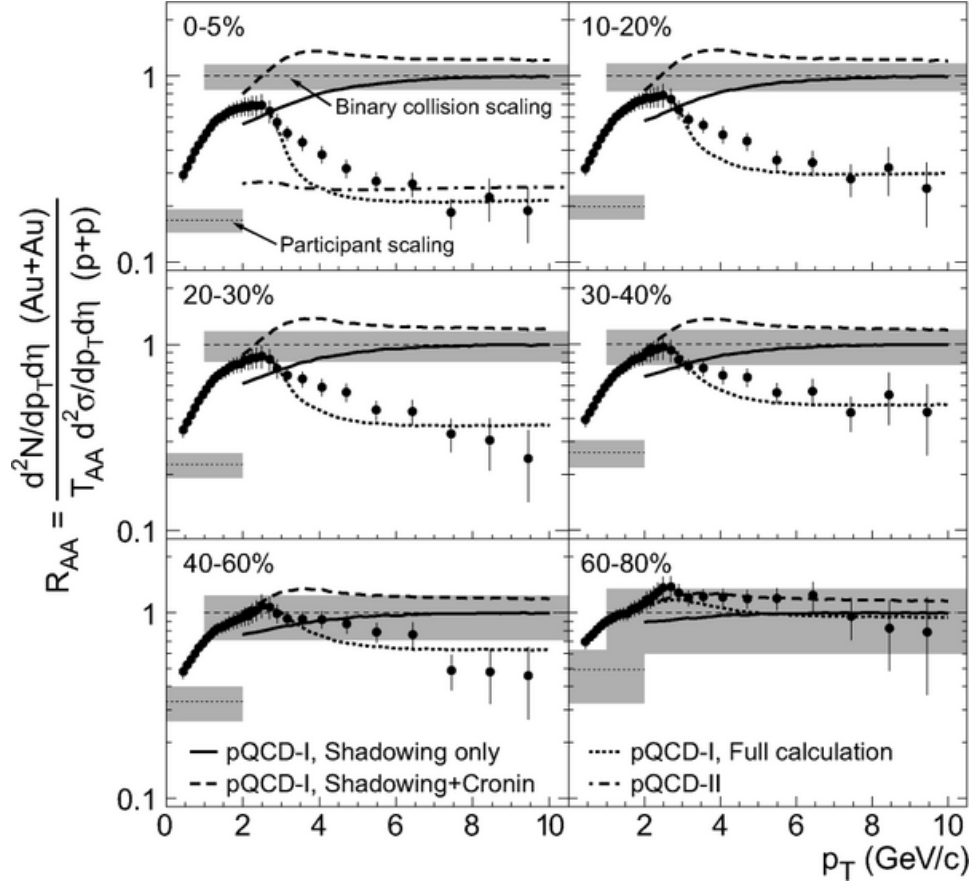


FIGURE 2.7 Fully corrected charged hadron R_{AA} at $\sqrt{s_{NN}} = 200$ GeV for six centrality classes [45].

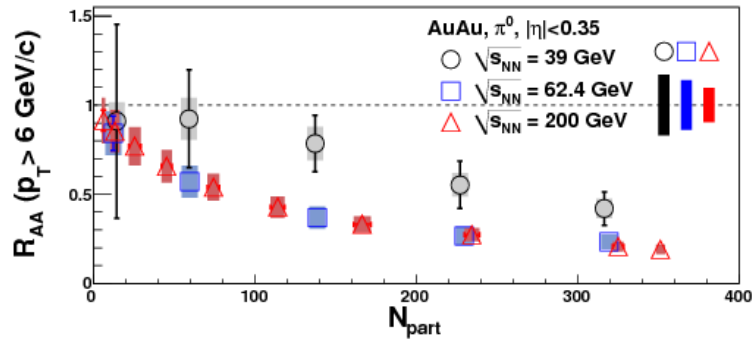


FIGURE 2.8 Fully corrected π^0 R_{AA} at $\sqrt{s_{NN}} = 39, 62.4,$ and 200 GeV versus N_{part} [59].

2.6 Y

Rather than just looking at the net nuclear modification as R_{CP} does, it may be informative to consider the centrality⁴ dependence of nuclear modification for high- p_T particles. An example for π^0 s by PHENIX at $\sqrt{s_{NN}} = 39, 62.4, \text{ and } 200 \text{ GeV}$, is shown in Fig. 2.8 [59]. The Au+Au data from every centrality is divided by the same $p+p$ data so that the denominator introduces a common scale factor while increasing the statistical and systematic errors. To investigate their shapes as a function of N_{part} more accurately, the distributions in Fig. 2.8 could be scaled by an arbitrary value, such as the yields of their most peripheral bins. This would make it easier to compare how the centrality dependence of the scaled yields varies with $\sqrt{s_{NN}}$ without introducing additional uncertainties from $p+p$ data. While the errors are still small for the PHENIX results shown in Fig. 2.8, they are larger for R_{CP} results from the highest p_T bins of low $\sqrt{s_{NN}}$ collisions since the statistical uncertainty of the most peripheral bin dominates the uncertainties. While the magnitude of R_{AA} or R_{CP} at high p_T will inform us of the net enhancement to suppression, the shape as a function of centrality tells us whether suppression or enhancement effects are increasing faster as we go more central. If suppression effects increase faster than enhancement effects then this provides evidence for partonic energy loss, even at energies where the net effects are dominated by enhancement. In other words, even if R_{AA} or R_{CP} is greater than unity, there may still be partonic energy loss that is simply being concealed by the magnitude of the enhancement effects. The N_{part} dependence of the N_{bin} -scaled high- p_T yields can therefore partially disentangle the enhancement and suppression effects by looking at whether the most central spectra are suppressed relative to any other centrality bin rather than just comparing them to the most peripheral. For this purpose we introduce a new variable for detecting partonic energy loss:

$$Y(\langle N_{part} \rangle) = \frac{1}{\langle N_{bin} \rangle} \frac{d^2 N_{high} p_T}{d\eta dp_T}(\langle N_{part} \rangle). \quad (2.3)$$

⁴Note that “increasing centrality” means the same thing as “going more central” and also corresponds to increasing N_{part} .

Chapter 3

Experimental Setup

Heavy-ion collisions were first carried out at fixed target facilities. Here ions of particular nuclei would be accelerated to near the speed of light and smashed into targets of a particular element. The ion-nucleus collisions resulted in sprays of particles that would be measured by arrays of detectors. These facilities provided, and continue to provide data at lower $\sqrt{s_{\text{NN}}}$. The problem was that new and interesting physics was expected at higher collision energies than were available at the time, but the center of mass collision energy, $\sqrt{s_{\text{NN}}}$, did not scale well with increasing beam energy for fixed target collisions. In particular, $\sqrt{s_{\text{NN}}}$ is roughly proportionate to the square root of the beam energy in a fixed target system. The high-energy frontier would not be best explored with fixed targets. Instead, collider facilities were designed so that the collision system would benefit from simply adding the beam energies in order to determine the $\sqrt{s_{\text{NN}}}$. A welcome side effect of colliders was having the center of momentum for the colliding system be in the lab frame regardless of $\sqrt{s_{\text{NN}}}$. There have been two heavy-ion colliders; the large hadron collider (LHC) that began taking data in 2010 and the relativistic heavy-ion collider (RHIC) which began operation in 2000. The LHC now takes Pb+Pb data at $\sqrt{s_{\text{NN}}} = 5.02$ TeV while RHIC runs Au+Au collisions at a maximum of $\sqrt{s_{\text{NN}}} = 200$ GeV.

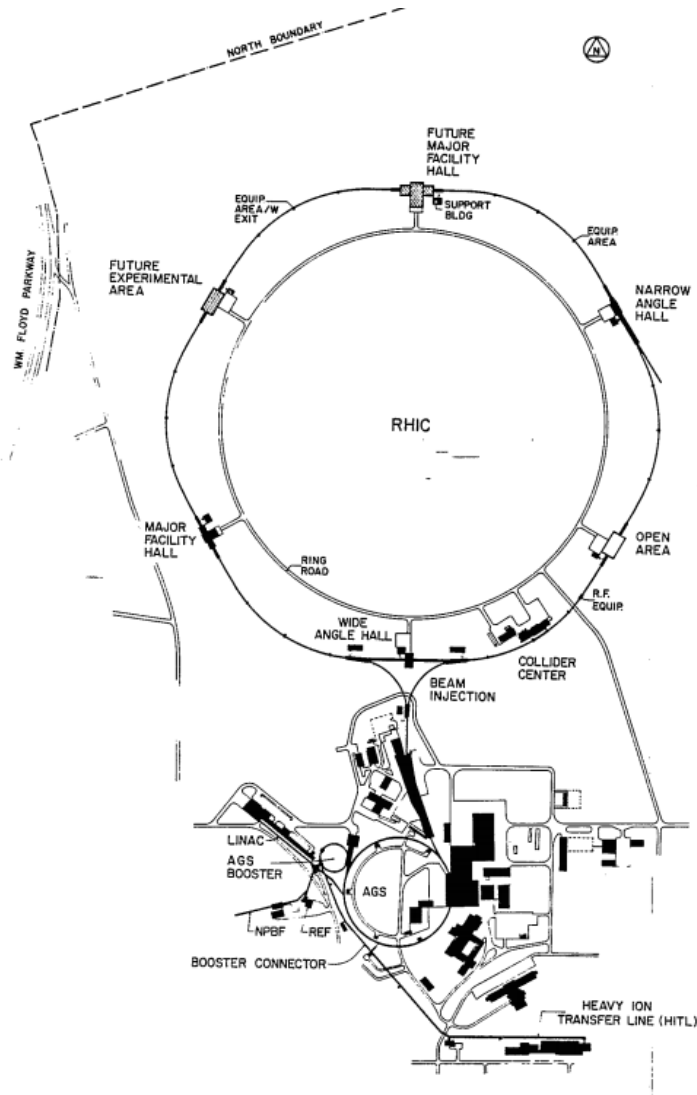


FIGURE 3.1 The site map for RHIC.

3.1 The Relativistic Heavy Ion Collider

Prior to 2012 the heavy ions at the Relativistic Heavy Ion Collider (RHIC) [60, 61] began at one of two Tandem Van de Graaffs that stripped off their electrons and provided their first stage of acceleration. Beginning in 2012, the Electron Beam Ion Source (EBIS) replaced the Tandems. The ions were further accelerated in a booster and then delivered to the Alternating Gradient Synchrotron (AGS) where they got another boost before being sent to RHIC at the injection energy of 9.8 GeV for $\sqrt{s_{NN}} = 19.6$ GeV and above

and at $E = \sqrt{s_{\text{NN}}}/2$ for lower collision energies. The top heavy-ion $\sqrt{s_{\text{NN}}}$ for RHIC is 200 GeV. The beams are fed into separate beam-pipes, yellow and blue, that counter rotate with it being possible to cross the beams at several interaction regions. Detector halls at these interaction regions initially held the experiments of 4 major collaboration, BRAHMS at 2 o'clock [62], STAR at 6 o'clock [63], PHENIX at 8 o'clock [64], and PHOBOS at 10 o'clock [65]. At the time of BES I only STAR and PHENIX were in operation and only STAR took data at all $\sqrt{s_{\text{NN}}}$. To achieve $\sqrt{s_{\text{NN}}} > 19.6$ GeV, RHIC ramps the beams to their final collision energies using a 28 MHz RF system in conjunction with a 197 MHz RF system. The heavy ion collision energies so far have occurred over $\sqrt{s_{\text{NN}}} = 7.7 - 200$ GeV. Figure 3.1 is a schematic for the layout described above [60, 61].

3.2 The Solenoidal Tracker at RHIC

The Solenoidal Tracker at RHIC (STAR) [66] is a large acceptance multi-component and multi-purpose detector located at RHIC. STAR sits in a large volume 0.5 T solenoidal magnet with near constant magnetic field in the direction of the beams [67]. The time projection chamber (TPC) provides the tracking for STAR as well as low- p_{T} charged particle identification [68]. The barrel electromagnetic calorimeter (BEMC) captures the neutral energy component of collisions at mid-rapidity [69]. The end-cap electromagnetic calorimeter (EEMC) captures the neutral energy component at forward rapidities [70]. The time-of-flight (TOF) aids in particle identification, aids in event position determination, and aids in tagging out-of-time events that would be poorly reconstructed [71]. Trigger detectors include the zero degree calorimeters [72, 73], the upgraded Vertex Position Detector (upVPD) [74], and the beam-beam counter (BBC) [75]. The detectors that are paramount to this dissertation are described in greater detail below.

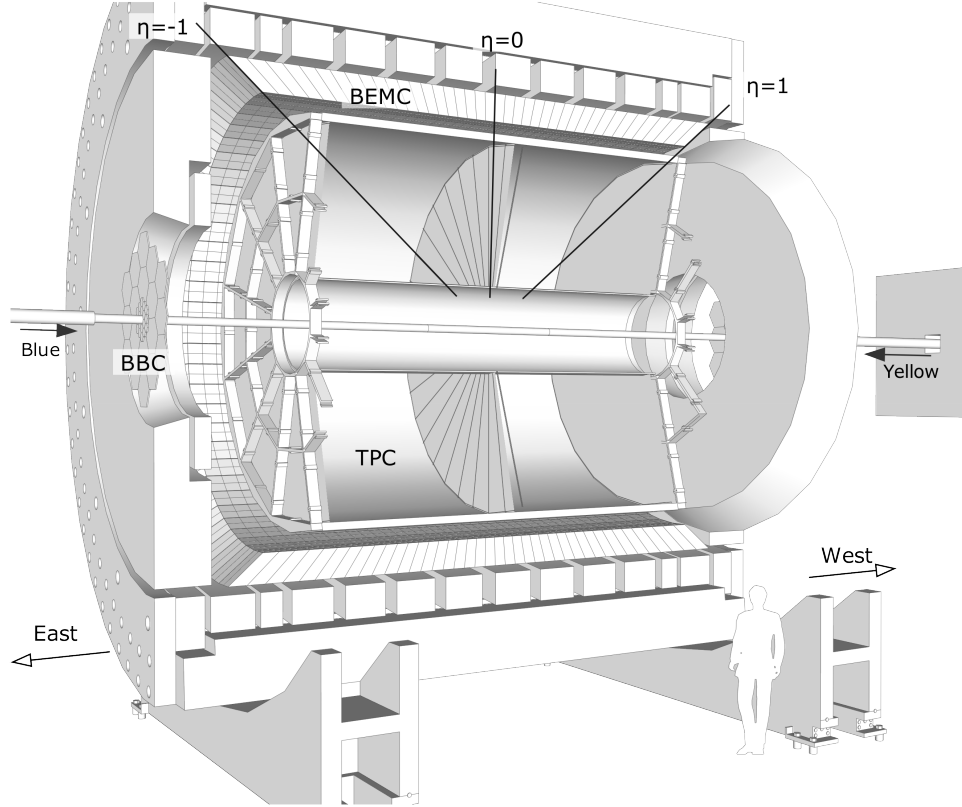


FIGURE 3.2 Schematic of the STAR detector.

3.2.1 Time Projection Chamber

The TPC provides charged particle tracking to include momentum determination and particle identification through dE/dx , energy-loss per unit length in the TPC gas [68]. This work-horse has 2π azimuthal and $|\eta^1| < 1$ acceptance as shown in Fig. 3.2. It features a central membrane cathode at 28 kV and anodes at each end generating a nearly uniform electric field of ≈ 135 V/cm with gating grids to eliminate charge buildup. The gas is a P10 and the drift velocity 5.45 cm/ μ s.

Particles emerging from heavy-ion collisions near mid-rapidity pass through the low material budget Be beam pipe before entering the TPC at a radius of 50 cm from the

¹Pseudorapidity measures the direction of the particle relative to the longitudinal or beam direction as $\eta \equiv -\ln(\tan(\theta/2))$, where θ is the polar angle of the particle's momentum vector relative to the lab defined positive beam direction.

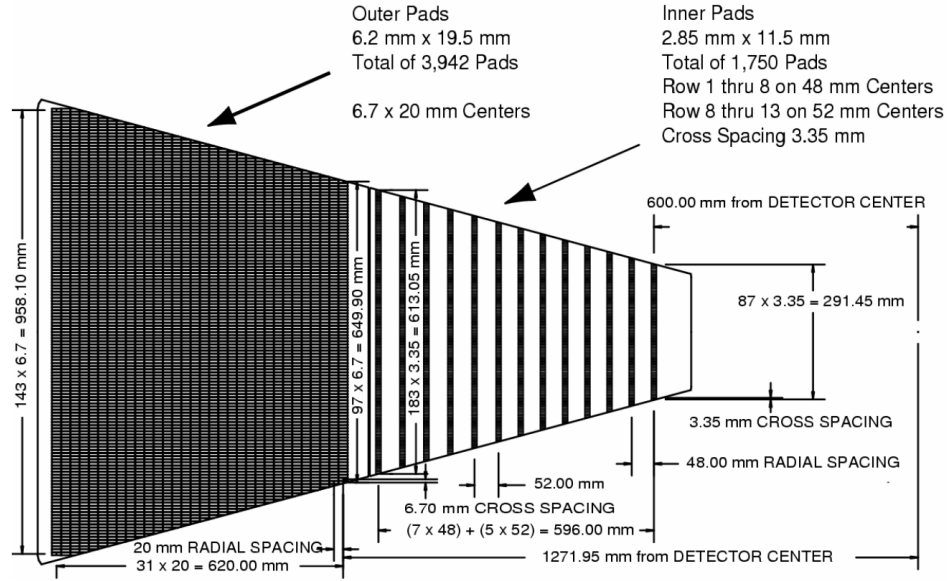


FIGURE 3.3 The inner and outer anode pad geometries for each STAR TPC sector consist of 30 densely spaced outer pad rows and 15 sparely spaced inner pad rows [68].

collision point radially². As particles move through the TPC they interact with the gas in the TPC ionizing it. The liberated electrons are then accelerated by the electric field toward the anodes at the outer edges of the TPC. They reach terminal velocity very quickly so that they can be considered to have moved at a constant velocity through the TPC. Where they hit the TPC end-cap readout electronics of the TPC gives the x and y positions of the hit while the drift time multiplied by the drift speed gives the z position. The end-cap electronics consists of 24 sectors, 12 on each side, with 45 pad rows each, as shown in Fig. 3.3 [68]. A gating grid is used to reduce the back flow of positive ions into the TPC. The gating grid consists of wires that can be opened, by all being set to the same voltage, or closed by being set to alternating potentials of ± 75 V from the nominal value [68]. The gating grid remains closed until triggered to open and it takes $2.1 \mu\text{s}$ to process a trigger and open the gating grid which reduces the usable volume of the TPC by 12 cm. The amount of charge that is read out in each pad is recorded and correlated to a value of dE/dx for a given track.

²The volume of the TPC extends out to 200 cm radially.

3.2.2 Trigger Detectors

The STAR trigger is used to select events of interest [76]. Zero degree calorimeters (ZDCs) exist at each RHIC detector in order to provide a common measure of instantaneous luminosity across the experiments [72, 73]. Perturbed heavy nuclei “evaporate” neutrons with low relative momenta such that they continue along straight trajectories even as the RHIC magnets bend the rest of the ions and charged beam fragments away. Calorimeters placed along this straight trajectory at $z \approx 20$ m from the interaction region were designed to trigger when hit by neutrons with ≈ 100 GeV energy each and in $|\eta| > 6.3$. While this is an efficient trigger detector for $\sqrt{s_{\text{NN}}} = 200$ GeV, it performs more poorly at lower $\sqrt{s_{\text{NN}}}$.

The upgraded Vertex Position Detector (upVPD) is based on scintillator and fast photomultiplier tubes (PMTs) [74]. This detector would be sensitive to X-rays, gamma rays, fast neutrons, and charged particles. It sits around the beam pipe at $|z| = 570$ cm and covers $4.24 < |\eta| < 5.1$. The larger acceptance and improved sensitivity of this detector makes it ideal for a low- $\sqrt{s_{\text{NN}}}$ trigger detector.

The beam-beam counter (BBC), visible in Fig. 3.2, is scintillator that sits around the beam pipe at $z = \pm 374$ cm from the interaction region and covers $3.4 < |\eta| < 5.0$ [75].

3.2.3 Minimum Bias Triggers

Because of the relatively low event rate capabilities of the STAR TPC, RHIC delivers far more heavy-ion collisions than STAR can fully record. In order to select collisions that are likely to contain interesting physics STAR uses fast detectors to select which collisions should be studied so that the TPC only collects data for those events. For this dissertation the goal is to minimize the biasing of the collision (event) selection. Coincident particle detection in fast detectors at forward and backward rapidities (*i.e.* upVPD, BBC, and/or ZDC) “triggers” data collection of a minimum bias event from the TPC. Coincidence is required because single detection would be more likely to be caused

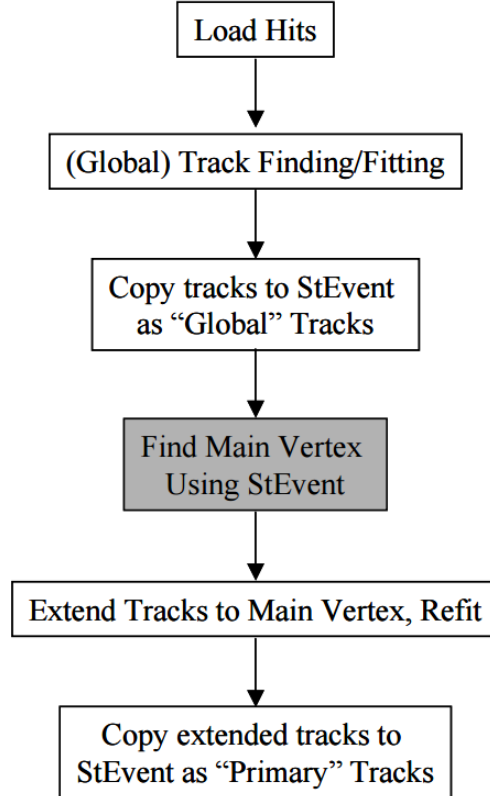


FIGURE 3.4 Summary of the event reconstruction algorithm used in STAR [79].

by single diffractive events, beam-pipe interactions, and other backgrounds. Coincident detection at forward and backward rapidities means that both nuclei were significantly perturbed in an interaction near the center of the TPC.

3.2.4 Data Acquisition and Event Reconstruction

The STAR data acquisition system (DAQ) [77] collects the data from each STAR subsystem, does initial event processing to reduce the data rate, and sends the processed events to the RHIC Computing Facility (RCF) [78] to await further processing. The DAQ's modular design has allowed new upgrades and detectors to be seamlessly integrated into the existing architecture.

The data for triggered events stored at RCF are corrected for detector calibrations [80], go through event reconstruction algorithms that reconstruct tracks, match these tracks to common vertices, and refit the tracks using reconstructed vertices as additional fit points [79, 81]. The algorithm for event reconstruction from TPC data is shown in Fig. 3.4 [79]. After the events are reconstructed they are run through a series of quality assurance procedures.

Chapter 4

Quality Assurance

After RHIC's beams have been injected, ramped up to full energy, and steered in collisions, STAR turns on its detectors and begins taking data. Data is taken until instantaneous luminosities are low enough to justify dumping the beam and re-injecting. The time from when the beam is injected until when it is dumped is called a "fill". While at top RHIC energies fills can last for several hours, at the lowest energies fills last for less than an hour. While the fill lasts, STAR takes "runs" of data. When a run is started the instantaneous luminosity is assessed so as to scale what the data acquisition rate of each trigger should be so that the overall data rates stay within STAR's capabilities. Runs last ≈ 30 minutes, during which time a STAR collaborator checks that the detectors are performing within their standard operating parameters. If a problem is noticed with the data or one of the detectors that run will be marked as bad and rejected from further analysis. This is STAR's "online QA", which accepts or rejects runs rather than individual events or entire fills. Basic track and event quality cuts are then used for further QA during the reconstruction of events so that they may later be studied for individual analyses from a common baseline. Each individual analysis then includes additional quality cuts based on what is required for their analysis. These quality cuts may reject tracks, events, or entire runs. This chapter will describe the data used for this dissertation. Then it will describe the typical quality cuts used, and why those

Energy (GeV)	Year	Triggered Events (10^6)	Good Events (10^6)
7.7	2010	98	1.8
11.5	2010	55	6.8
14.5	2014	275	11
19.6	2011	110	15
27	2011	165	28
39	2010	230	88
62.4	2010	155	42
200	2010	310	120

TABLE 4.1 Data used in these analyses. The good event count is for events that pass the run and event quality cuts.

values were selected, as well as some quality cuts that were developed for this specific analysis.

4.1 Data

The data for these analyses were taken in 2010, 2011, and 2014 as shown in Table 4.1. Detector performance, calibrations, and reconstruction techniques varied over time. Additionally, a narrower beam pipe was inserted between 2011 and 2014 and additional material in the form of an inner silicon detector was placed between the beam pipe and the TPC.

4.2 Good Run and Event Selection

By run-averaging physics quantities that should not vary with time due to detector effects, runs that are statistically inconsistent may be rejected. This is shown in Fig. 4.1 for two quantities: $\langle p_T \rangle$ and $\langle \text{charge} \rangle$. Neither of these quantities should vary even if portions of the TPC are included and excluded from data reconstruction. $\langle \text{charge} \rangle$ is defined as the number of positive tracks minus the number of negative tracks divided by the number of charged tracks for each run. If a run contained more background events than average from beam+beam-pipe interactions then these physics quantities would be

different for that run, with a larger $\langle \text{charge} \rangle$ and a smaller $\langle p_T \rangle$. Runs of these varieties were excluded and Fig. 4.1 shows only those runs that were within 3σ of the run average. For $\sqrt{s_{\text{NN}}} = 7.7 \text{ GeV}$, 327 of 1864 runs were removed from the data analysis while for $\sqrt{s_{\text{NN}}} = 62.4 \text{ GeV}$, 101 of 530 runs were removed from the data analysis. Because bad runs were often shorter than average, the number of events rejected by removing these runs was not as large as one would expect by just looking at the number of runs rejected.

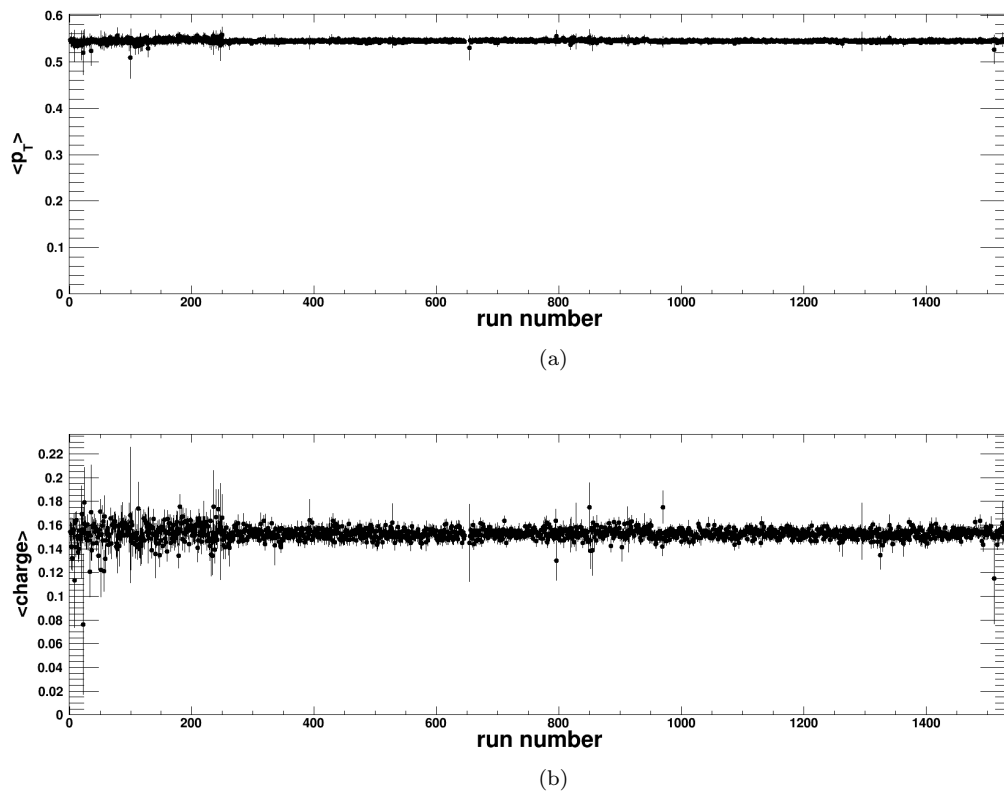


FIGURE 4.1 The mean p_T of each run is shown in the upper figure and the mean charge of each run is shown in the lower for $\sqrt{s_{\text{NN}}} = 7.7 \text{ GeV}$. Runs were excluded if means of physics quantities within those runs were not within 3σ of the average.

In addition to QA that rejected runs based on run averaged physics quantities, there was also QA that rejected events. These event cuts included a requirement that the reconstructed vertex of a collision be no more than 30 cm from the center of the TPC in the beam, z , direction. The location of the vertex in this direction is denoted as V_Z . The V_Z distribution has a strong dependence on the collision energy due to the

broader longitudinal beam profiles at lower $\sqrt{s_{\text{NN}}}$. A narrower beam profile at higher $\sqrt{s_{\text{NN}}}$ means that the width of the beam intersection region where the beams are crossed is reduced. This drives the variation in the V_Z distributions at $\sqrt{s_{\text{NN}}} = 7.7 \text{ GeV}$ and $\sqrt{s_{\text{NN}}} = 200 \text{ GeV}$ shown in Fig. 4.2. Not only is the V_Z distribution broader at $\sqrt{s_{\text{NN}}} = 7.7 \text{ GeV}$, but it also has extra features. These features are reconstructed vertices from collisions of ions in the beams' periphery with the beam-pipe. The spikes near $\pm 55 \text{ cm}$ are due to flanges while the jumps near $\pm 75 \text{ cm}$ are where the beam-pipe tapers to a narrower section near the interaction region. Requiring that reconstructed vertices are in $|V_Z| < 30 \text{ cm}$ from the center of the detector cuts out these features, but is not guaranteed to cut out all beam-pipe interactions. To improve on this a cut on the radial position¹ of the reconstructed vertex is also included.

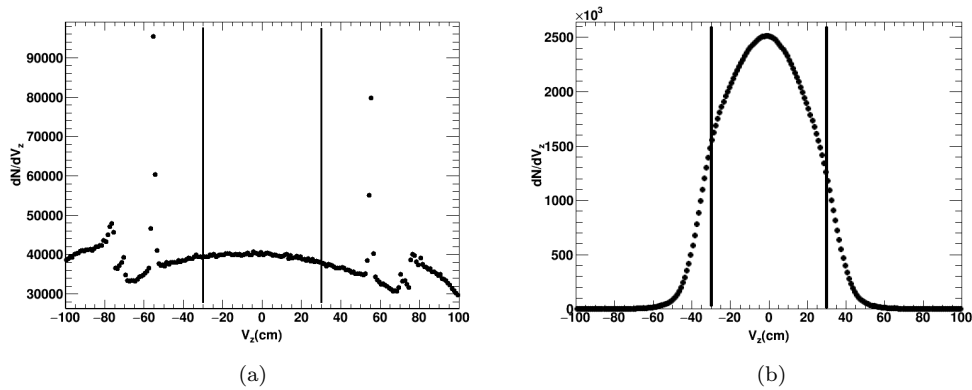


FIGURE 4.2 The reconstructed vertex V_Z distributions are shown for $\sqrt{s_{\text{NN}}} = 7.7 \text{ GeV}$ (left) and $\sqrt{s_{\text{NN}}} = 200 \text{ GeV}$ (right).

Figure 4.3 shows for $\sqrt{s_{\text{NN}}} = 7.7 \text{ GeV}$ the radial distribution of reconstructed vertices. The beam-pipe is clearly distinguishable, motivating a cut on $V_R < 1 \text{ cm}$. This cut removes the background of low multiplicity “fixed target” Au+Be collisions. Higher $\sqrt{s_{\text{NN}}}$ does not have this background due to narrower radial beam profiles and reduced transverse emittance [82].

¹The radial vertex position is measured from the mean vertex position in the plane transverse to the beam axis. It is defined as $V_R = \sqrt{(V_X - V_{X,0})^2 + (V_Y - V_{Y,0})^2}$

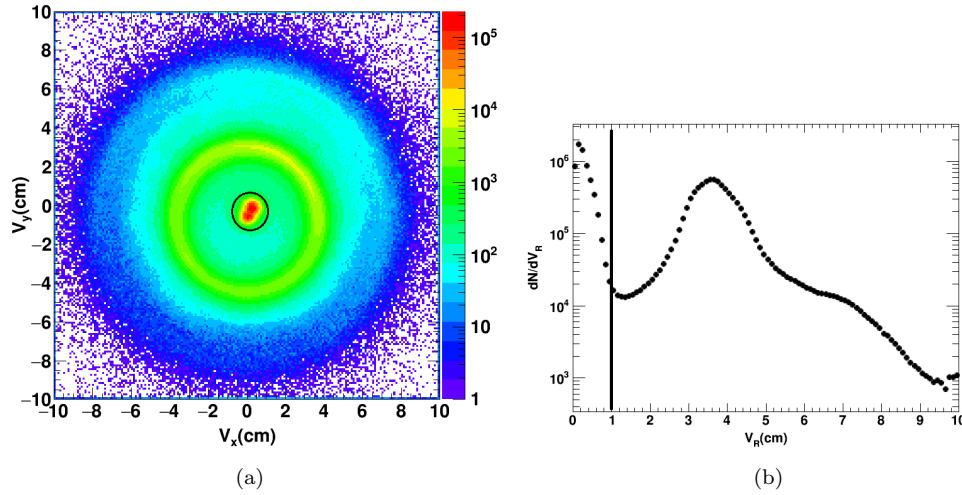


FIGURE 4.3 The $\sqrt{s_{NN}} = 7.7$ GeV reconstructed vertex distribution is shown on the left for (V_X, V_Y) and on the right for V_R .

The final event cut used in this analysis is a requirement that at least two tracks in each event be matched to hits in the TOF. This requirement removes out-of-time events where the events would not be properly reconstructed due to the tracks in each half of the TPC drifting in opposite directions. Requiring two TOF matches rather than one almost completely eliminates the chance of an event being included due to an out-of-time track randomly pointing toward an in-time TOF hit. Only requiring two TOF matches rather than most tracks to be matched to TOF hits minimizes the chance of the event being rejected due to poor TOF matching efficiency while still cutting out-of-time events.

Figure 4.4 shows how many events were removed by the various run and event cuts for $\sqrt{s_{NN}} = 7.7$ and 62.4 GeV. If the events were found to fail some condition or test then they were “flagged” with a value from 1 to 10. The first 7 tests are exclusive, so failing the third, for example, would mean the event would be thrown away before testing the fourth. Event Flags 7 through 10 are inclusive, so it is possible for a single event to fail all three of these tests and to be counted for each. The number of events that passed all event and run cuts are given by Event Flag = 0; less than 2 million for 7.7 GeV and more than 40 million for 62.4 GeV. Event Flag 1 is for when the data file fails to open

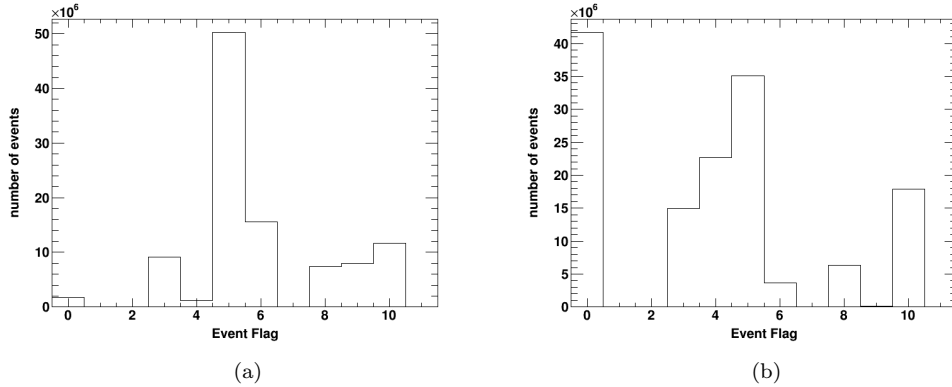


FIGURE 4.4 The number of events that pass all run and event cuts is given by Event Flag = 0 for $\sqrt{s_{NN}} = 7.7$ (a) and 62.4 GeV (b). The other Event Flag indices count the number of events that failed each cut.

while Event Flag 2 is for when the run stored in the data file is from a different data set than intended, so it is not surprising that these both have zero events. Event Flag 3 is for events in runs that were rejected by the run cuts. Event Flag 4 is a trigger cut, requiring that the event to have a minimum bias trigger. Event Flag 5 is for when no primary vertex could be reconstructed. This is where the most events were rejected. Some of these triggered events would be from ions hitting the beam pipe, especially at low $\sqrt{s_{NN}}$, while others would be from very peripheral collisions with few tracks in the TPC. Event Flag 6 comes from a requirement that at least 2 TPC tracks in each event be matched to hits in the TOF. Reconstructing events that fail this cut results in biases in η distributions and unphysical results. Event Flag 7 was only used for 200 GeV and is a requirement that $|V_Z^{TPC} - V_Z^{VPD}|^2 < 3$ cm. Event Flag 8 is from a requirement that the event have a multiplicity that places it in the 0-80% centrality, so events that are too peripheral are not counted. Event Flag 9 counts the events with $|V_R| > 1$ cm while Event Flag 10 counts the events with $|V_Z| > 30$ cm. There were many beam-pipe interactions for $\sqrt{s_{NN}} = 7.7$ GeV data. Such events would have $V_R > 1$ cm, and have few tracks so that they were likely to be counted by both Event Flag 8 and Event Flag

² V_Z^{VPD} is for vertices reconstructed with the vertex position detector while V_Z^{TPC} is for vertices reconstructed using TPC tracks. V_Z will be reported using the TPC measurement everywhere else in this thesis.

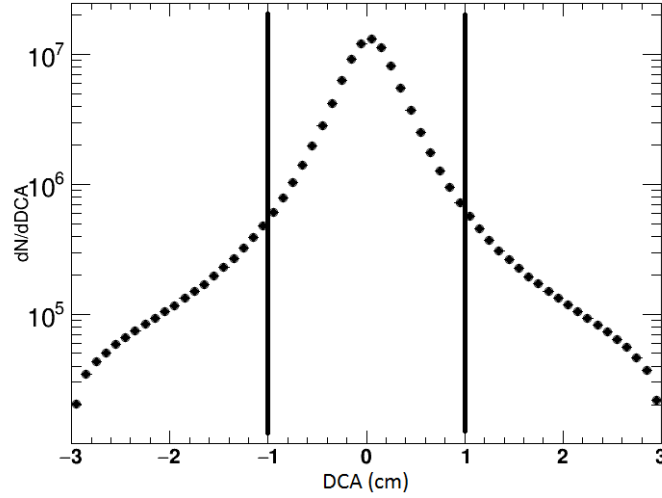


FIGURE 4.5 Signed DCA of charged hadrons for $\sqrt{s_{NN}} = 7.7$ GeV.

9. Only a small fraction of recorded events at $\sqrt{s_{NN}} = 7.7$ GeV pass the quality cuts to be analyzed, but this fraction improves with increasing energy.

4.3 Good Track Selection

The TPC readout consists of 45 pad-rows where hits may be measured. The more hits in the TPC that are found and used the better the track may be described to discern its momentum and energy loss. However, requiring many hits in the TPC means that many tracks will be rejected and the tracking efficiency and detector acceptance will be reduced. Then the corrections for these effects will be larger and the sensitivity of the measurement to how well we can model detector effects on track reconstruction is increased. For this analysis, a minimum of 15 space charge points in the TPC are required for each track. This cuts out $\approx 2\%$ of the tracks. Also, in order to prevent the splitting of hits from a single track into two or more tracks, a cut is included that requires that the number of hits used in the fit divided by the number of possible hits for a track of that geometry is greater than 0.52. This cut removes $< 1\%$ of tracks.

During event reconstruction, reconstructed tracks are used to determine the location of the primary vertex: the position of the heavy-ion collision in the detector. Then the tracks are fit again using the primary vertex as an additional fit point. The primary vertex has an uncertainty associated with its position, so the tracks are not constrained to pass through the primary vertex and instead have a distance of closest approach (DCA). If the track is reconstructed with the primary vertex as a fit point then the DCA is the primary DCA. For choosing whether or not to keep a track for analysis it is better to use the global DCA. The larger the global DCA, the more likely that the track did not originate at the primary vertex and instead is either the daughter of a secondary decay or a background track that is incorrectly associated with the primary vertex. By cutting on global DCA the purity of actual primary tracks can be increased. This is especially important at high- p_T because refitting tracks while including the primary vertex as a fit point will shift the reconstructed momentum of the track to a false value. The larger the global DCA, the larger the shift in the p_T when going from a global track to a primary track will be. Low- p_T analyses at STAR that are primarily concerned with having a high reconstruction efficiency use a cut on a three-dimensional global DCA of 3 cm. This analysis, like most other high- p_T analyses at STAR, uses a cut of 1 cm instead since the much straighter high- p_T tracks are more effected by daughters from secondary decays and randomly associated particles from other events or cosmic rays whose DCA distributions are not as tightly correlated with the vertex position as are primary tracks. For these background tracks, using the primary vertex in the fit to reconstruct their trajectories biases and shifts their momenta, and this effect is larger for the very straight high- p_T tracks since a small change in their curvature has a much larger effect on their reconstructed momenta than for low- p_T tracks. This cut removes $\approx 20\%$ of tracks. The global signed DCA distribution, the projection of the global DCA onto the transverse plane, is shown in Fig. 4.5 for $\sqrt{s_{NN}} = 7.7$ GeV. If the vertex is inside the extrapolation of the reconstructed track than it has a positive sign. Otherwise the sign is negative.

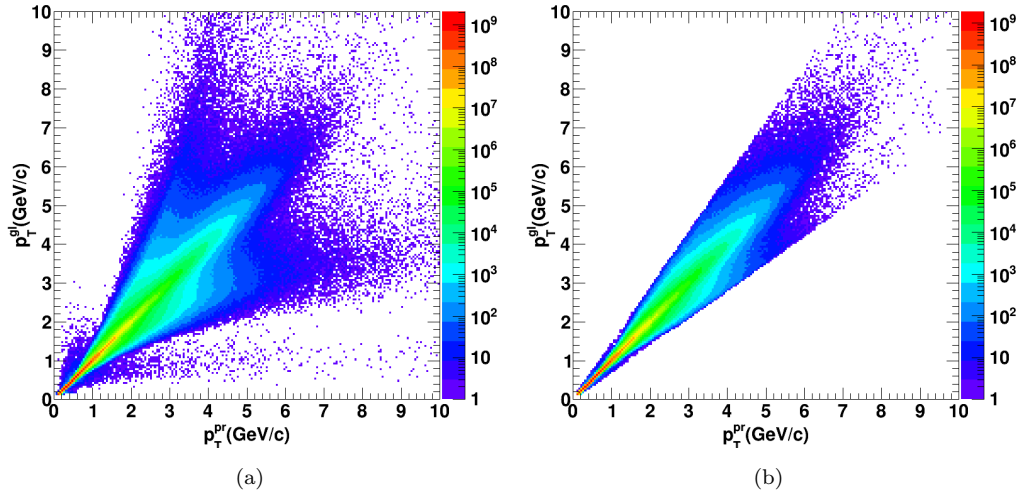


FIGURE 4.6 Primary p_T , p_T^{pr} , is plotted on the x-axis and global p_T , p_T^{gl} , on the y-axis for $\sqrt{s_{\text{NN}}} = 39$ GeV. The right plot is the same as the left except that it includes the cut: $7/10 \cdot p_T^{\text{gl}} < p_T^{\text{pr}} < 10/7 \cdot p_T^{\text{gl}}$.

After applying these standard track quality cuts there is still a significant high- p_T background of tracks whose momenta are shifted significantly when the primary vertex is included in the fit. This may be due to vertices being reconstructed in the wrong location due to secondary decays or randomly associated tracks. While there are relatively few of these poorly reconstructed tracks, they are distributed broadly in p_T and become dominant at high- p_T . In order to remove this background a cut is included that requires that the p_T of a track reconstructed without using the primary vertex, p_T^{gl} , be similar to the p_T when the vertex is included in the fit, p_T^{pr} . In particular, it is required that $7/10 \cdot p_T^{\text{gl}} < p_T^{\text{pr}} < 10/7 \cdot p_T^{\text{gl}}$. The effects of this cut are shown in Fig. 4.6. This cut removes a very small fraction of the total tracks. This cut, like all of the track quality cuts for this analysis, had a very weak dependence on $\sqrt{s_{\text{NN}}}$, but it has a strong dependence on p_T with the majority, as high as 100%, of tracks at high- p_T and low- $\sqrt{s_{\text{NN}}}$ being rejected by this cut. The effects of this and the other tracks quality cuts are accounted for with a tracking efficiency correction described in Chapter 5.

Chapter 5

Corrections

Detector level spectra are modified from their true distributions by several effects. In order to recover the true distributions, corrections must be developed that account for each of these effects. The corrections must be applied as a function of p_T , $Mult$, and $\sqrt{s_{NN}}$. In order to leverage limited statistics of simulated detector effects, for each $\sqrt{s_{NN}}$ the p_T and $Mult$ dependence of the effects are fit with $2D$ functions and these functions are combined to construct the overall correction function. This method takes advantage of the smooth evolution of the correction factors as a function of p_T and $Mult$ and reduces the statistical uncertainty in the correction. Had these corrections been applied bin-by-bin, far more detector simulations would have been necessary, to the point of straining the computational resources available at RCF. The first section deals with feeddown, knockouts, and photo-production. The second section develops the single particle tracking efficiency correction. The third section develops an identified species fitting procedure. The fourth section addresses momentum resolution and energy loss. And finally, the sixth section combines the various corrections into a single $2D$ correction function for each $\sqrt{s_{NN}}$.

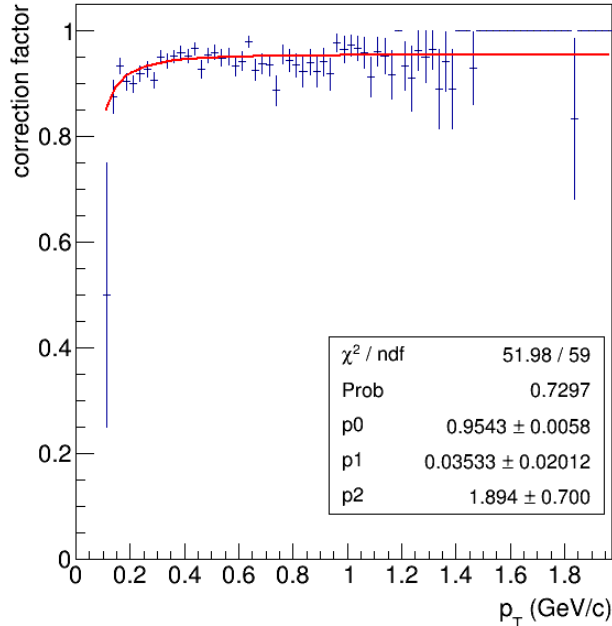


FIGURE 5.1 Fit of feeddown correction factor for charged hadrons in $0 < Mult \leq 20$ at $\sqrt{s_{NN}} = 7.7 \text{ GeV}$ as a function of p_T .

5.1 Feeddown, Knockout, and Photo-Production

When high- p_T particles pass through detector material, support material, and the beam pipe they sometimes knock out protons. These protons from secondary interactions form a background that needs to be subtracted from the data. While data-driven methods for this correction exist [83], they have been found to be consistent with a method using simulated events passed through a simulation of STAR that will be outlined in this section. The simulation is favored here because it simultaneously corrects for other backgrounds as well. One of these backgrounds is the photo-production of electrons in the same materials listed above. Another background comes from the weak decay of hadrons that carry strangeness and have a lifetime that separates their decay vertex from the primary vertex while still decaying relatively close to the primary vertex. In order to subtract these backgrounds, UrQMD [84] produced collisions were run through a GEANT [85, 86] simulation of the STAR detector and then reconstructed. These

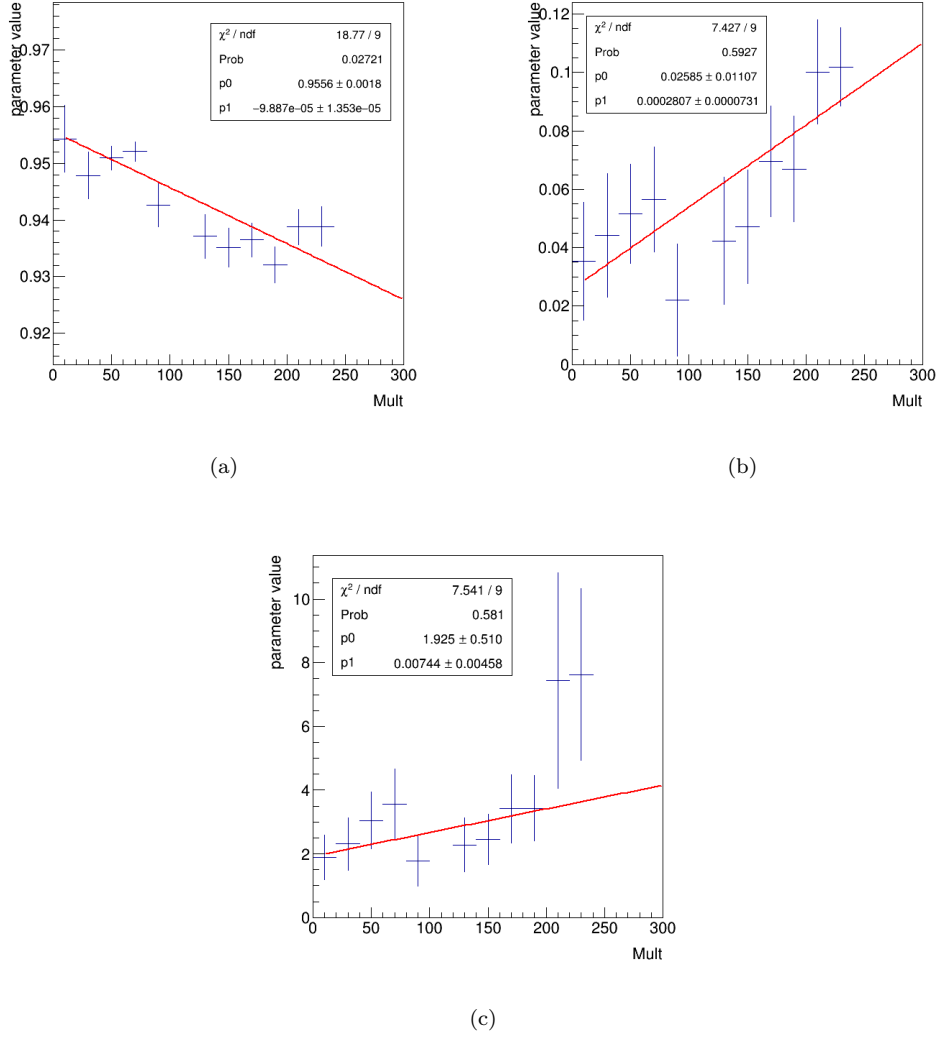


FIGURE 5.2 Linear fits of the $Mult$ dependence of parameters p_0 (a), p_1 (b), and p_2 (c) from Eq. 5.1 for $\sqrt{s_{NN}} = 7.7$ GeV.

simulated collisions were used to correct, at the ensemble level, for the fraction of background particles that would pass the track quality cuts used in this analysis. After the simulated events were created, the first step was measuring the kinematic information of identified pions, kaons and protons which UrQMD identified as primary tracks. These histograms were divided by histograms that were filled from all charged particles that passed the analysis track quality cuts; primary and feeddown inclusively. This correction factor is applied to the measured spectra to account for the feeddown particles, that we

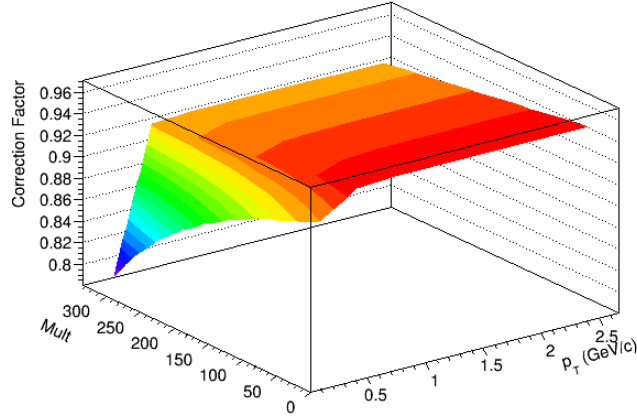


FIGURE 5.3 Feeddown correction used for $\sqrt{s_{NN}} = 7.7$ GeV.

do not want to report, in the final measurement. This correction was performed in bins of $Mult$, 20 units broad, and as a function of p_T as shown in Fig. 5.1. The next step was to fit these correction data with a 3 parameter function,

$$C_{feed}(p_T) = p_0 \cdot e^{-(p_1/p_T)^{p_2}}, \quad (5.1)$$

in each $Mult$ slice (Fig. 5.1), and then to fit these parameters to determine their centrality dependence (Fig. 5.2). It is then possible to construct the $2D$ function,

$$C_{feed}(p_T, Mult) = (p_0 + p_1 \cdot Mult) \cdot e^{-((p_2 + p_3 \cdot Mult)/p_T)^{(p_4 + p_5 \cdot Mult)}}, \quad (5.2)$$

shown for $\sqrt{s_{NN}} = 7.7$ GeV/c in Fig. 5.3. Note that the ordered parameters (p_0, p_1, \dots) are used for convenience but that they are not the same in Eq. 5.1 as in Eq. 5.2. There are two advantages in constructing a $2D$ function for the feeddown correction rather than just fitting the p_T dependence in each centrality bin. The first advantage is that we leverage the functional form of the centrality dependence which reduces the number of simulated events needed. The second advantage is a more precise event by event

correction rather than averaging across large centrality bins. Similar logic applies to the rest of the corrections in this chapter. Note that Fig. 5.3 exhibits a very weak centrality dependence so that the correction to R_{CP} is very small.

5.2 Tracking Efficiency

The p_T , centrality, and species dependent tracking efficiencies in the TPC were determined by embedding Monte Carlo tracks, modified by a GEANT [85, 86] simulation of STAR, into real events for each energy [87]. The embedding was flat in $-1 < \eta < 1$ and flat in $0 < p_T < 5 \text{ GeV}/c$ in minimum bias events, with $\sim 500k$ embedded tracks per collision energy and species. The efficiency was defined to be the fraction of embedded Monte Carlo tracks that, after event reconstruction, were matched to reconstructed tracks that passed track quality cuts. These efficiencies were determined with respect to p_T and in slices of $Mult$, as for the feeddown correction. The correction was determined with respect to the Monte Carlo p_T and since it is determined in narrow p_T bins no p_T weighting is needed. These p_T -dependent efficiencies, for each species and $Mult$ slice in the BES, were fit using, Eq. 5.3; while the efficiency corrected single species spectra were fit with Eq. 5.5.

$$\epsilon(p_T) = p_0 \cdot e^{-(p_1/p_T)^{p_2}} \quad (5.3)$$

Figure 5.4 shows a typical efficiency curve. The efficiency varied year to year and energy to energy as portions of the TPC suffered a loss of performance or were repaired. π^+ and π^- shared similar efficiencies with each other for all energies and centralities, as did K^+ with K^- and \bar{p} with p . Pion efficiencies were nearly flat as a function of p_T for $p_T > 0.5 \text{ GeV}/c$. They ranged in value from 70% at $\sqrt{s_{NN}} = 39 \text{ GeV}$ for $Mult = 400^1$ to 88% at $\sqrt{s_{NN}} = 14.5 \text{ GeV}$ for $Mult = 10$. Simliar to the pions, proton efficiencies were

¹The reason that particular values of $Mult$ and p_T are quoted rather than ranges is that these efficiencies were extracted from the $2D$ functions developed later in this chapter.

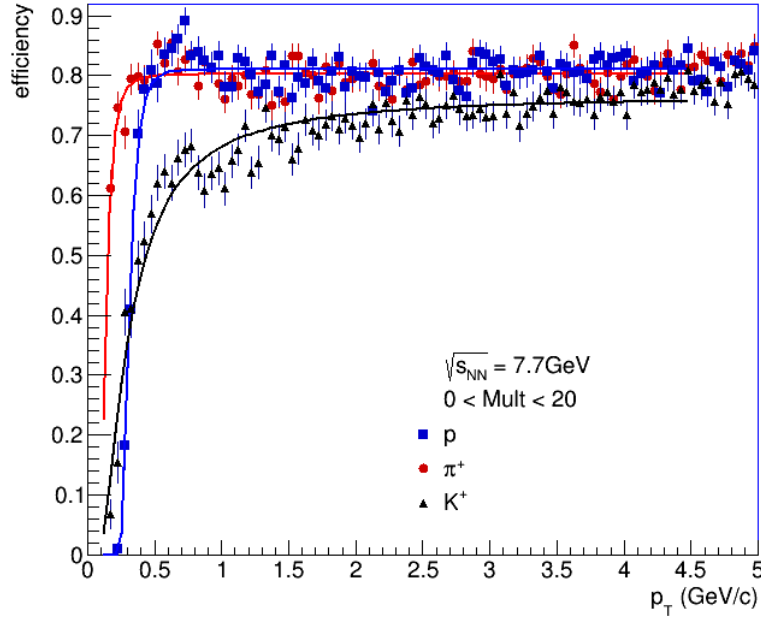
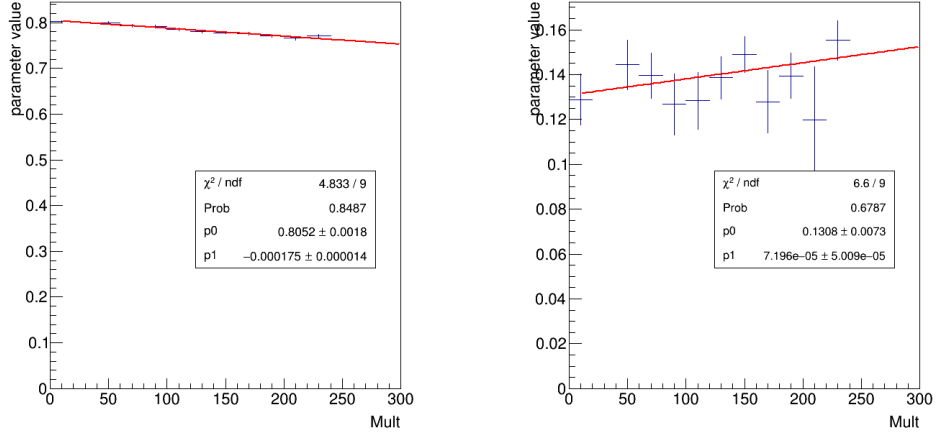


FIGURE 5.4 Fit of single species efficiency from embedding of π^+ , K^+ , and p into $0 < Mult < 20$ for $\sqrt{s_{NN}} = 7.7$ GeV.

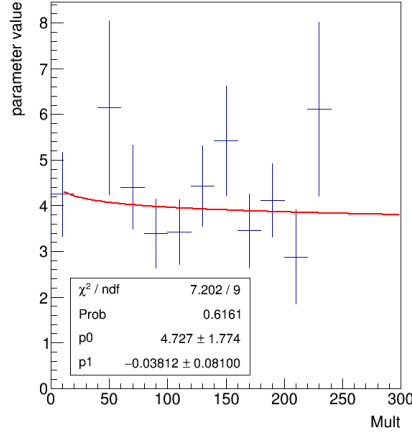
also nearly flat as a function of p_T for $p_T > 0.5$ GeV/c. They also ranged in value from 70% at $\sqrt{s_{NN}} = 39$ GeV for $Mult = 400$ to 90% at $\sqrt{s_{NN}} = 14.5$ GeV for $Mult = 10$. Kaons have a strong p_T dependence due to low- p_T Kaons having a higher probability to decay and not be reconstructed than high- p_T Kaons. For $\sqrt{s_{NN}} = 39$ GeV and $Mult = 400$ the efficiency is 40% at $p_T = 0.5$ GeV/c and increases to 70% at $p_T = 5$ GeV/c. For $\sqrt{s_{NN}} = 14.5$ GeV and $Mult = 10$ the efficiency is 50% at $p_T = 0.5$ GeV/c and increases to 85% at $p_T = 5$ GeV/c. The efficiencies decrease linearly with increasing $Mult$ such that an increase in $Mult$ of 100 will cause a worsening of the efficiency by 1.5-2%, as seen in Fig. 5.5(a).

The $Mult$ dependence of the parameters of Eq. 5.3 were fit with lines for p_0 and p_1 and with a power-law for p_2 (Fig. 5.5). The power-law was used to avoid negative values for the parameter in the high $Mult$ extrapolation. Next, a 2D function was constructed for each species (i),



(a)

(b)



(c)

FIGURE 5.5 Fits of the $Mult$ dependence of $\sqrt{s_{NN}} = 7.7$ GeV π^+ efficiency parameters p_0 (a), p_1 (b), and p_2 (c) .

$$\epsilon_i(p_T, Mult) = (p_0 + p_1 \cdot Mult) \cdot e^{-((p_2 + p_3 \cdot Mult)/p_T)^{(p_4 \cdot Mult^{p_5})}}, \quad (5.4)$$

similar to the $2D$ correction function constructed for feeddown in the previous section.

The resulting $2D$ correction for π^+ at $\sqrt{s_{NN}} = 7.7$ GeV is shown in Fig. 5.6.

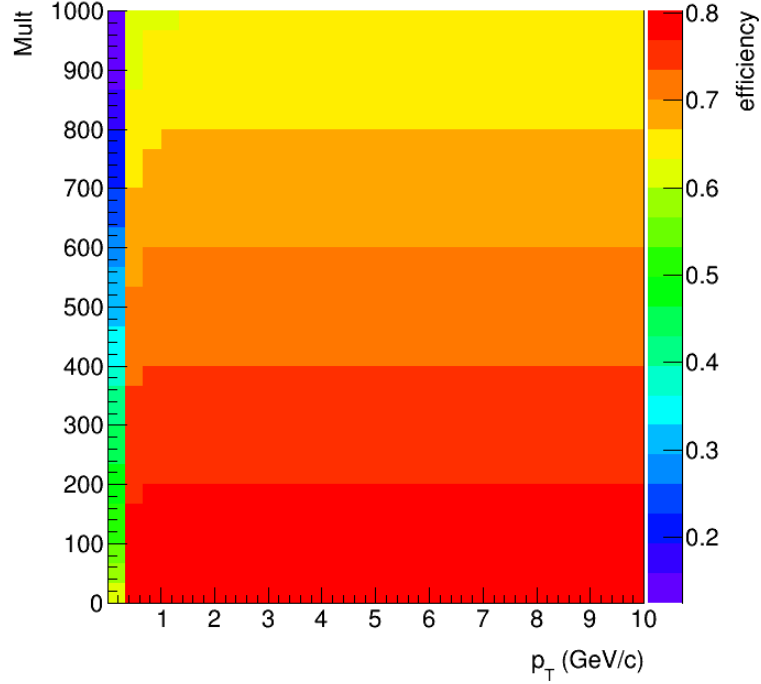


FIGURE 5.6 Fit of single species efficiency from embedding of π^+ for $\sqrt{s_{\text{NN}}} = 7.7$ GeV.

5.3 Identified Spectra Fits

The charged hadron efficiency is constructed as the weighted average of the single species efficiencies where the weights are provided by fits to the corrected spectra using Eq. 5.5,

$$\text{spectra} = \frac{1}{2\pi p_{\text{T}}} \frac{d^2 N_i^j}{d\eta dp_{\text{T}}}(p_{\text{T}}) = p_0 \cdot (1 - p_1(1 - p_2) \cdot p_{\text{T}}^2)^{\frac{1}{1-p_2}}, \quad (5.5)$$

for each species, i , and centrality, j . This particular arrangement of parameters was chosen so that the default step size in the fitting algorithm would consistently converge on a minimum. Other functional forms were tried but only this one gave consistently good fits across all centralities for all six species and the seven energies studied in this dissertation. Figure 5.7 shows a typical fit to the spectra. The centrality dependence of these parameters is then fit with power-laws for each of p_0 , p_1 and p_2 (Fig. 5.8). The identified spectra did not go as high in p_{T} as the unidentified spectra, but the efficiencies were nearly constant in the p_{T} region extrapolated into, which limited the

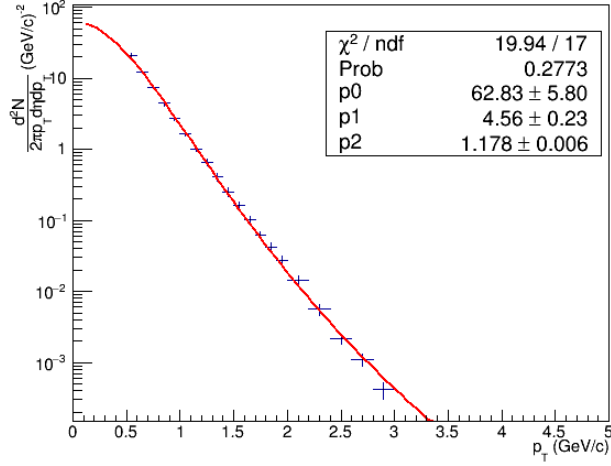


FIGURE 5.7 Fit to the spectra of π^+ for peripheral 60-80% $\sqrt{s_{\text{NN}}} = 7.7$ GeV.

impact from the extrapolation on the systematic uncertainties. Next a $2D$ function of corrected spectra was constructed,

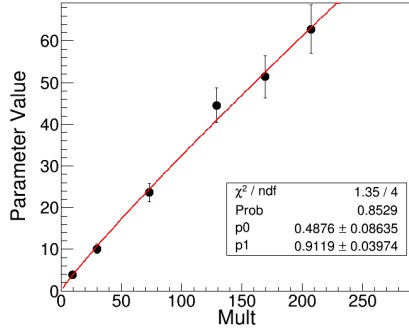
$$\text{spectra}_i(p_T, Mult) = (p_0^0 \cdot Mult^{p_0^1}) \cdot (1 - p_1^0 \cdot Mult^{p_1^1} (1 - p_2^0 \cdot Mult^{p_2^1}) \cdot p_T^2)^{\frac{1}{1 - p_2^0 \cdot Mult^{p_2^1}}}, \quad (5.6)$$

for each species, i (Fig. 5.9). The parameters in the $2D$ function describe the $Mult$ dependence of the parameters from Eq. 5.5 with,

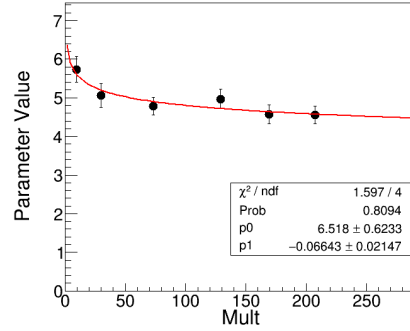
$$\begin{aligned} p0 &\rightarrow p_0^0 \cdot Mult^{p_0^1} \\ p1 &\rightarrow p_1^0 \cdot Mult^{p_1^1} \\ p2 &\rightarrow p_2^0 \cdot Mult^{p_2^1}. \end{aligned} \quad (5.7)$$

5.4 Momentum Resolution and Energy Loss

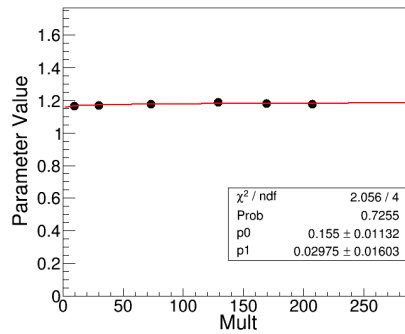
Track reconstruction does not perfectly reproduce the particle trajectories. This means that the reconstructed p_T of a particle can deviate from the actual p_T the particle had



(a)



(b)



(c)

FIGURE 5.8 Fit parameters as a function of centrality for π^+ at $\sqrt{s_{NN}} = 7.7$ GeV for parameters p0 (a), p1 (b), and p2 (c).

immediately after a collision. One reason for this is that TPC hits have a resolution associated with their position. Track reconstruction using the imperfect positions of hits given by the TPC hit reconstruction results in distorted tracks. The amount of momentum smearing caused by this effect is described by the momentum resolution. Momentum resolution can be improved by requiring more hits per track, by narrowing the cut on DCA, and by using the reconstructed primary vertex position in the track fit. Figure 5.10 shows the distributions of relative p_T shifts of embedded tracks. Within p_T bins these distributions are projected onto the y-axis and fit with Gaussians as in Fig. 5.11. The means give the energy loss correction: the shift in momenta due to the pion mass assumption used in track reconstruction, as well as due to a small energy loss in the beam pipe and other detector materials, and also due to residual distortions not corrected for in calibrations. The Gaussian widths give the momentum resolutions.

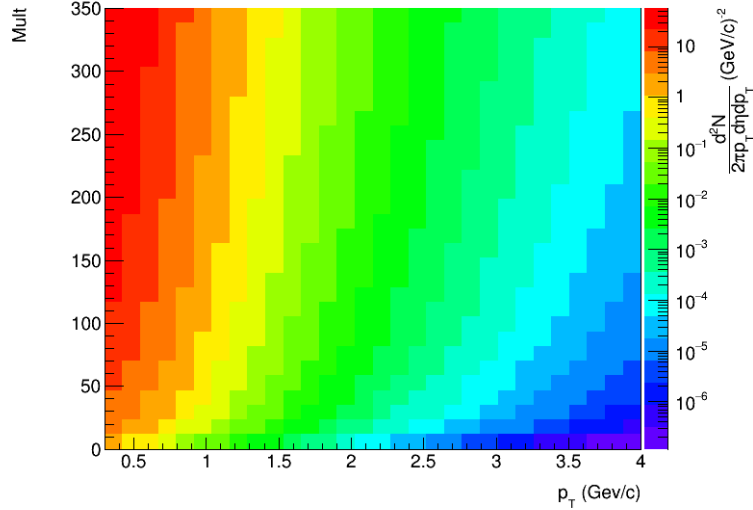


FIGURE 5.9 The fits of the spectra were used to construct this 2D function to describe the spectra as a function of p_T and $Mult$ shown here for $\sqrt{s_{NN}} = 7.7$ GeV.

The momentum dependence of the Gaussian widths is fit at high p_T , while avoiding the edges of the spectrum as seen in Fig. 5.12, in order to extrapolate to higher p_T where no embedding was done. σ_{p_T}/p_T is found to be $\approx (0.5+0.25 \cdot p_T)\%$. There is little species, energy or centrality dependence to this result, although it does depend on track quality cuts and whether the primary vertex is used in track reconstruction, as it was here.

In order to estimate the effect of momentum resolution on the reconstructed charged hadron spectra several steps were taken. First the single species spectra are fit with Eq. 5.5. Then one p_T spectrum is constructed by randomly sampling this fit and another by randomly sampling the fit and smearing the momentum by the previously obtained resolution. The ratios of the smeared to the non-smeared distributions give an estimate for how large the effect of momentum resolution is on the single species spectra. 100M tracks are generated for each scenario. Most tracks are measured at low p_T due to how steeply the spectra fall. Figure 5.13 shows that momentum smearing has a negligible effect at low p_T . However we want to be certain of the behavior at high p_T , so the fit in Fig. 5.12 is extrapolated to high p_T and the spectrum is sampled in only this higher p_T region using the same method as before. The results of this procedure are

shown as the red and blue triangles in Fig. 5.13 where we see a 1% effect for the ranges accessible by data. Because the correction is negligible at low p_T and small at high p_T it is not applied and is instead included in the systematic uncertainty analysis for the high- p_T charged hadrons as a very conservative, flat 2% systematic uncertainty. This uncertainty is smaller than all others included in the analysis and so has little effect. Had this correction been applied then a 1% uncertainty would have been appropriate, but as the correction was not applied a 2% systematic uncertainty was taken so as to err on the side of caution. Similar results were obtained when this procedure was repeated with the other species.

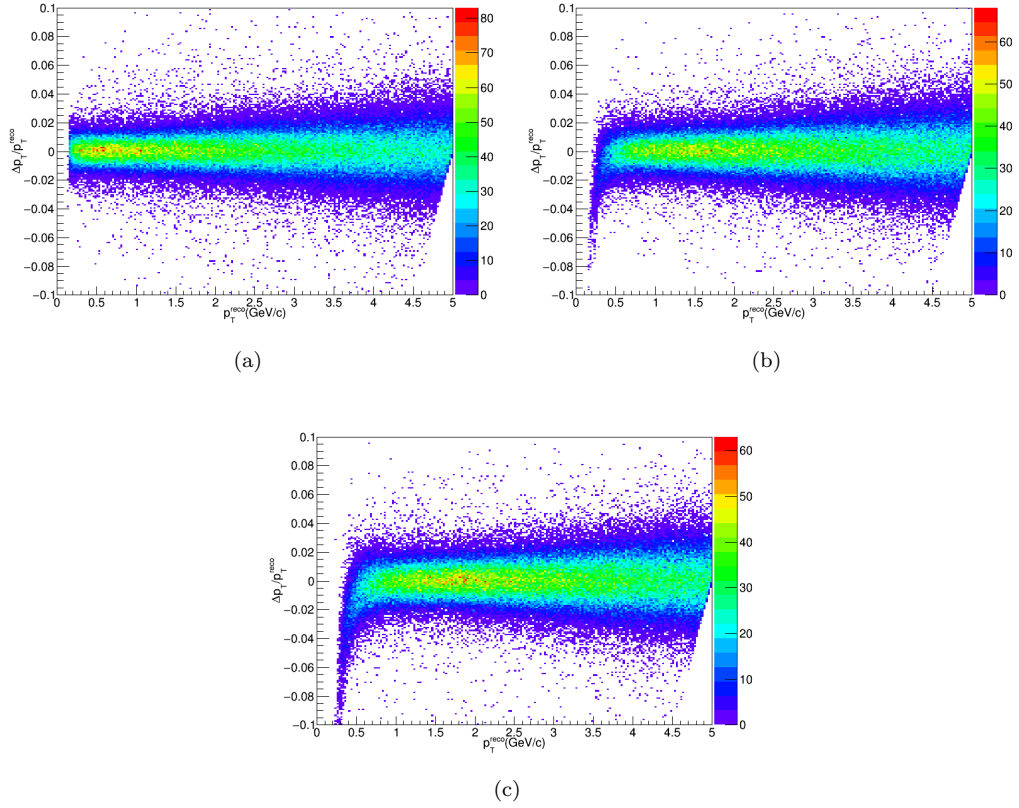


FIGURE 5.10 The distributions of p_T shifts as a function of p_T are shown for π^+ , K^+ , and p for $\sqrt{s_{NN}} = 7.7$ GeV.

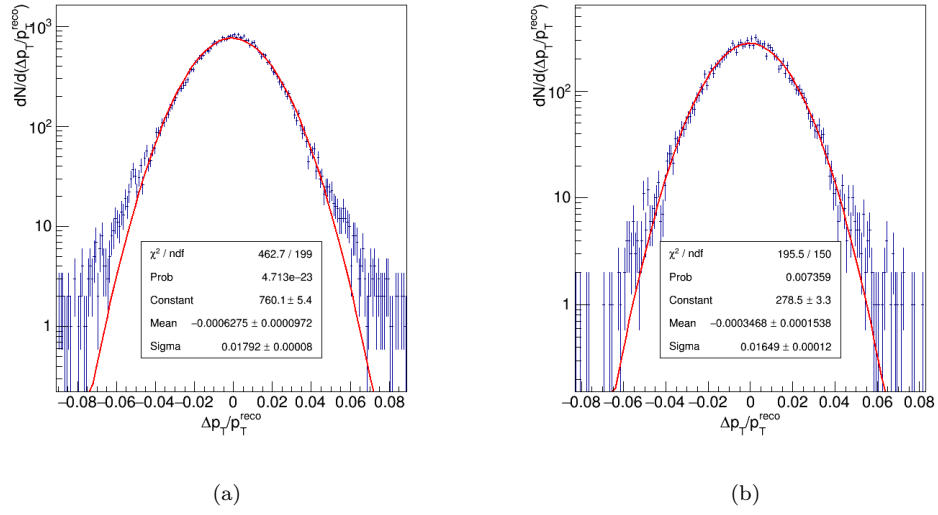


FIGURE 5.11 The distributions of p_T shifts as a function of p_T are shown for p at $\sqrt{s_{NN}} = 7.7$ and 62.4 GeV projected over $4.5 < p_T < 4.75$ GeV/c and fit with Gaussians.

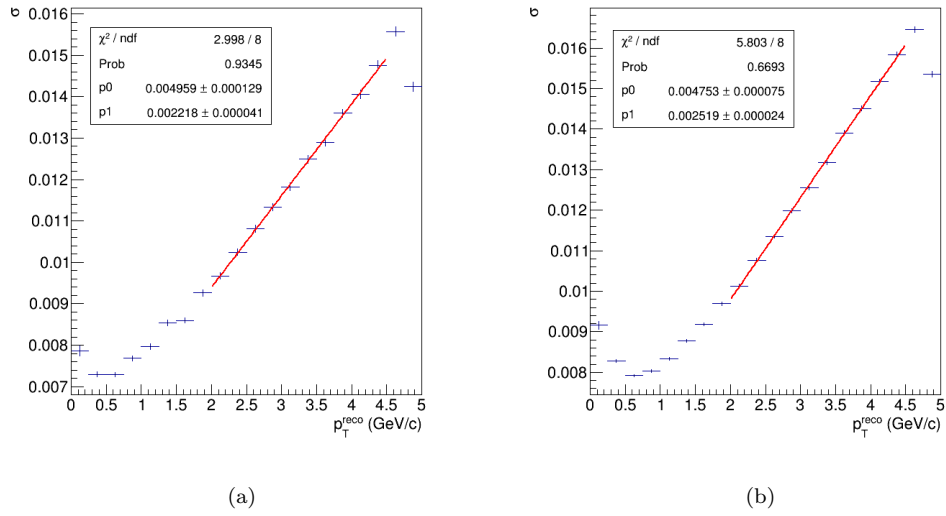


FIGURE 5.12 Momentum resolution as a function of p_T and fit at high- p_T with a linear fit for π^+ at $\sqrt{s_{NN}} = 7.7$ GeV and 62.4 GeV. The momentum resolution is similar for the other species and energies.

5.5 Combined Correction

The final step is to construct the correction factor that includes the feed-down correction as well as the charged hadron efficiency. The previously constructed 2D functions (Eq.

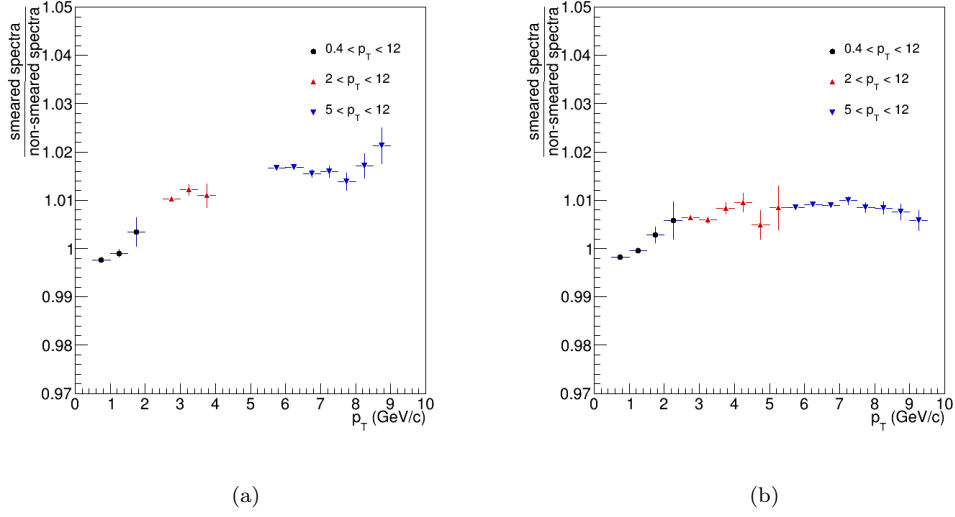


FIGURE 5.13 Ratio of smeared spectra to non-smeared spectra as a function of p_T for π^+ at $\sqrt{s_{NN}} = 7.7$ GeV and 62.4 GeV.

5.2 for C_{feed} , Eq. 5.4 for ϵ_i , and Eq. 5.6 for $spectra_i$) are combined for each collision energy. This is done by taking the weighted average of the tracking efficiencies with the fits to the identified species providing the weights. This gives a charged hadron tracking efficiency which can be combined with the feeddown correction to give us a combined correction factor,

$$correction(p_T, Mult) = C_{feed} \frac{\sum_i \epsilon_i \cdot spectra_i}{\sum_i spectra_i}. \quad (5.8)$$

Each charged track is weighted by the inverse of this combined correction. The corrections for each collision energy are shown in Fig. 5.14.

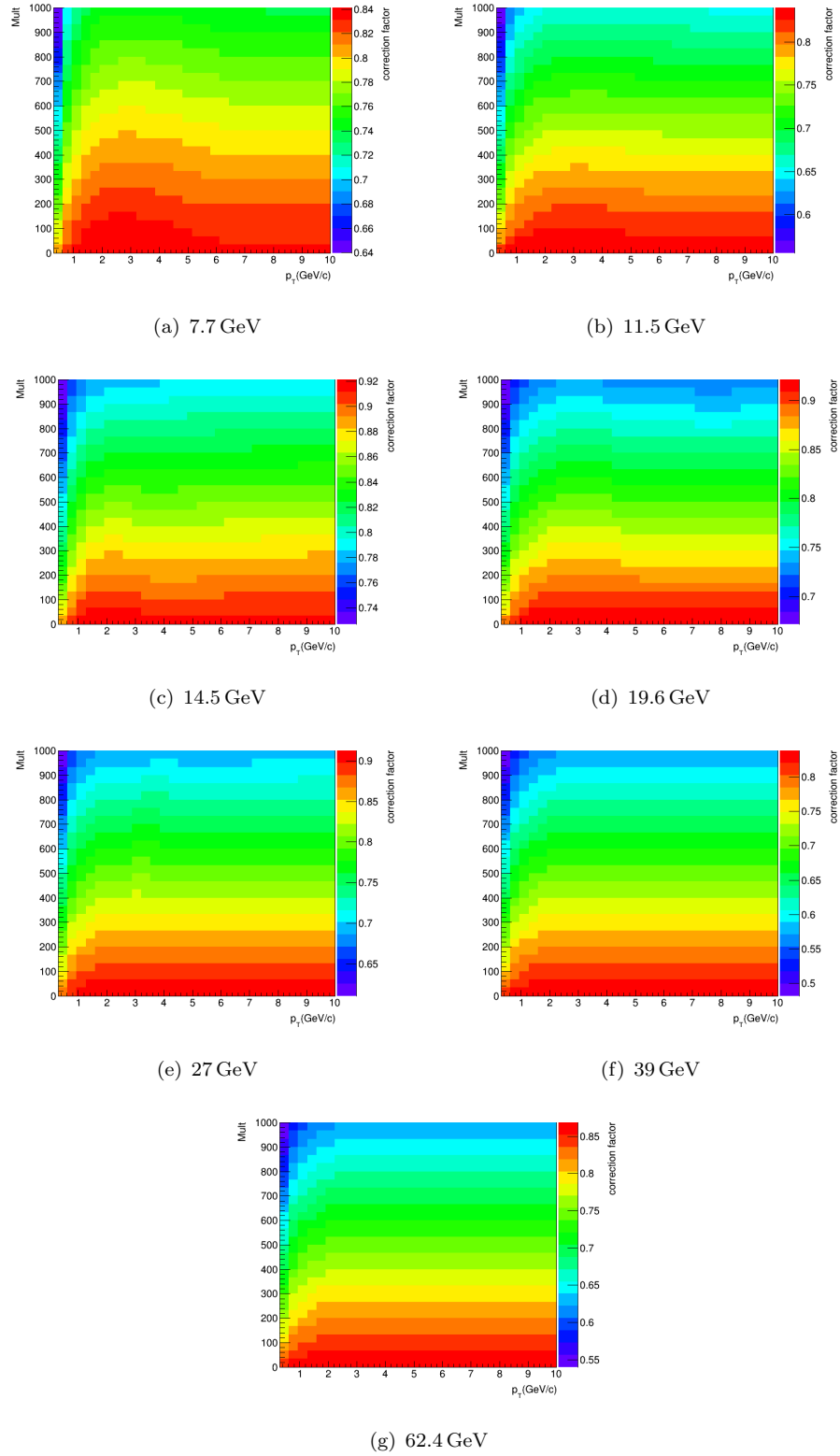


FIGURE 5.14 Combined corrections as a function of p_T and $Mult$ for inclusive charged hadrons for each energy in the BES.

Chapter 6

Systematic Uncertainties

The analyses in this dissertation have four major sources of systematic uncertainties: an uncertainty on the trigger and vertex reconstruction efficiency, an uncertainty due to momentum resolution, an uncertainty on the tracking efficiency correction, and one for the contribution to the spectra from weak decay feed-down. The different sources of systematic uncertainty are added in quadrature. Several of the systematics are correlated meaning that if the value is wrong in one bin it will be wrong in the same direction for other bins. However, when the ratios of spectra from different centralities are taken the correlated uncertainties largely cancel¹. More specifically, if two observables have correlated uncertainties then their ratio will not simply be their quadrature sum, but will be reduced as shown in Eq. 6.1.

$$f = \frac{A}{B}, \quad \sigma_f \approx f \sqrt{\left(\frac{\sigma_A}{A}\right)^2 + \left(\frac{\sigma_B}{B}\right)^2 - 2\frac{\sigma_A\sigma_B}{AB}} \quad (6.1)$$

This relationship is heavily exploited in this dissertation. Each paragraph below will detail a different systematic uncertainty. Then the last paragraph will summarize the

¹This is similar to climate data where there can be a large uncertainty in the averaged global temperature due to sparse data sampling, instrument uncertainties, or variation in sampling locations to name a few reasons. However, because these biases are mostly unchanged from year to year, the change in average temperature from a reference year, the temperature anomaly, can be measured with much smaller uncertainties.

range of combined uncertainties and which systematics were considered correlated in which dimensions.

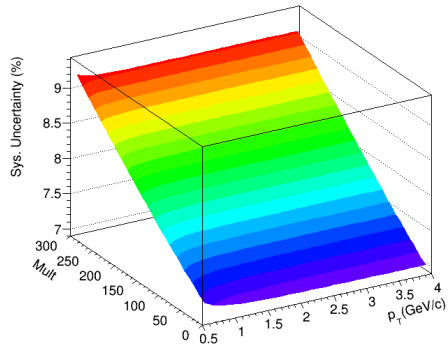
First consider the uncertainty in the trigger efficiency and the vertex finding uncertainty. Very peripheral collisions produce few particles and are less likely to satisfy the trigger conditions. This results in a reduction in the total cross-section for triggered events from the true interaction cross section. Among those peripheral events that satisfy the trigger, some still don't have enough tracks in the TPC to reliably reconstruct a vertex. This further reduces the cross section of reconstructed peripheral events. The Glauber Monte Carlo outlined in Chapter 4 and described with more detail by [44] is used to estimate the missed cross section and to characterize the centrality of a collision by the number of tracks produced at mid-rapidity. It also is used to determine the mean number of binary collisions and the mean number of participating nucleons in each collision. There is a systematic uncertainty on these mean values that is driven by the uncertainty in the estimation of the total cross-section due to non-reconstructed peripheral collisions. There are smaller contributions to this uncertainty from uncertainties in the $p+p$ cross-section and in the Woods-Saxon parameters for a gold nucleus. These uncertainties are largest for peripheral collisions, and become smaller for increasing event multiplicity. Tables of $\langle N_{\text{bin}} \rangle$, $\langle N_{\text{part}} \rangle$, and their uncertainties can be found for all collision energies and centralities used in these analyses in Appendix A.

The second systematic uncertainty considered in this analysis is due to momentum resolution. As was shown in Chapter 5, the correction to spectra due to momentum resolution was 1% at its largest. To be conservative, rather than applying the 1% correction and keeping a 1% systematic, a 2% systematic uncertainty was assigned to the uncorrected spectra for all centralities, p_T , and $\sqrt{s_{\text{NN}}}$. However, this uncertainty was taken to be 100% correlated with centrality so that it factors out in the ratio for R_{CP} and in the arbitrary normalization of Y .

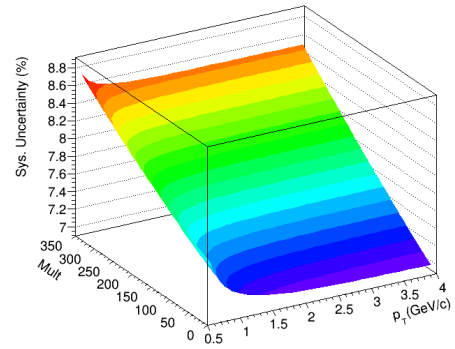
The third systematic uncertainty is from the determination of the tracking efficiency. The STAR embedding procedure results in single particle tracking efficiencies being

determined with a 5% systematic uncertainty [88, 89]. The efficiencies were taken to be correlated across species for a given centrality, $\sqrt{s_{\text{NN}}}$, and p_{T} so that the procedure for constructing the charged hadron efficiency still results in a 5% systematic uncertainty across the board.

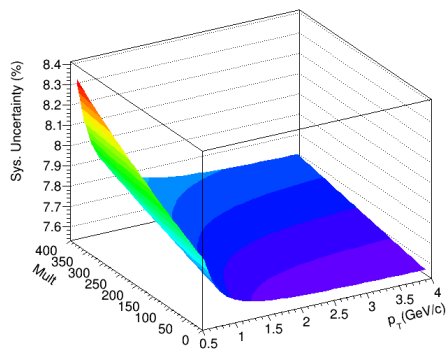
The final and largest point-to-point systematic uncertainty comes from the correction for the contribution to the spectra from weak decay feed-down. Due to uncertainties in the UrQMD's particle ratios, a 100% systematic uncertainty on the feed-down was assumed. This translates into a $\sqrt{s_{\text{NN}}}$, p_{T} , and centrality dependent uncertainty on the final spectra on the order of 5-10% depending most strongly on collision energy and centrality.



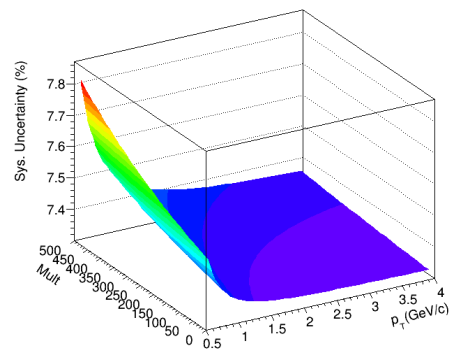
(a) 7.7 GeV



(b) 11.5 GeV



(c) 14.5 GeV



(d) 19.6 GeV

FIGURE 6.1 Total systematic uncertainties for p_T spectra (from tracking efficiency, momentum resolution, and weak decay feed-down in summed in quadrature) are shown for each $\sqrt{s_{NN}}$ as a function of p_T and detector level multiplicity measured in $|\eta| < 0.5$.

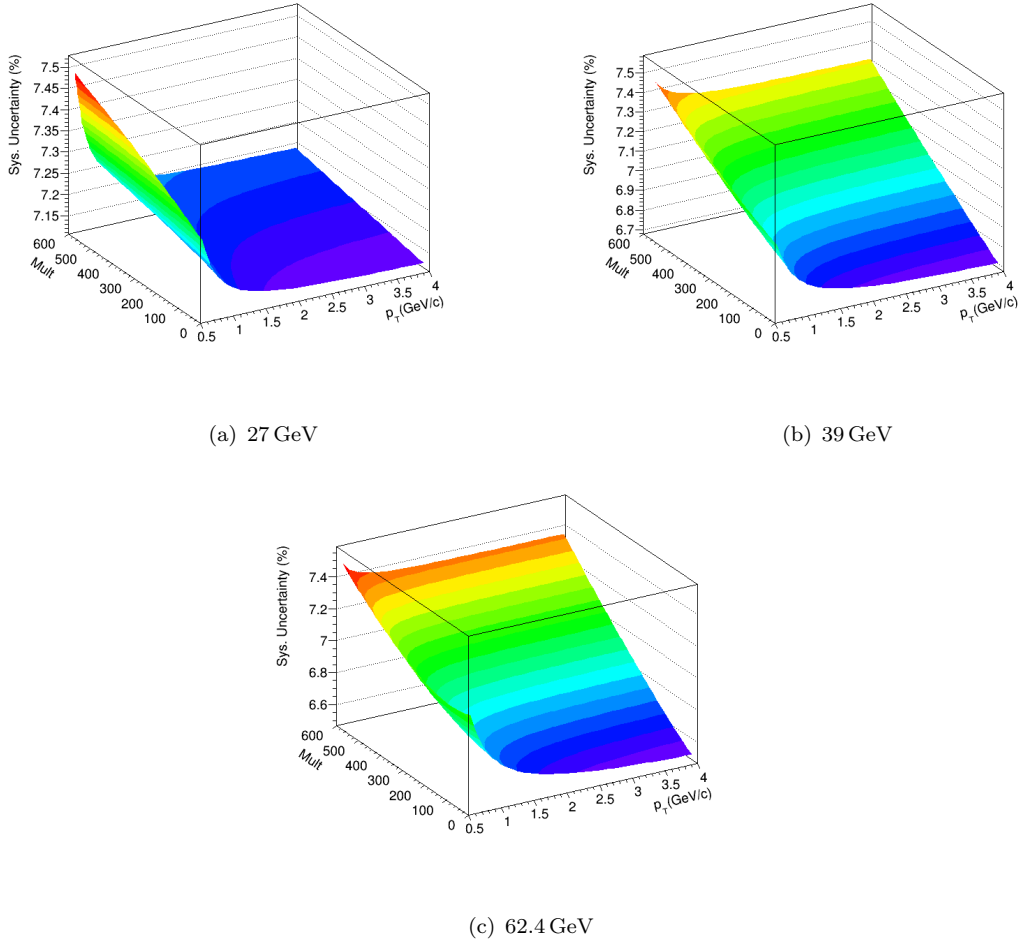


FIGURE 6.2 Total systematic uncertainties for p_T spectra (from tracking efficiency, momentum resolution, and weak decay feed-down in summed in quadrature) are shown for each $\sqrt{s_{NN}}$ as a function of p_T and detector level multiplicity measured in $|\eta| < 0.5$.

The p_T spectra combined relative systematic uncertainties of tracking efficiency, momentum resolution, and weak decay feed-down are added in quadrature with the results shown in Figs. 6.1 and 6.2. The errors are dominated by weak-decay feed-down and are worst at low p_T and high multiplicity. They range from a minimum 6.6% for high p_T and low multiplicity collisions at $\sqrt{s_{NN}} = 62.4$ GeV up to a maximum 9.1% for low p_T and high multiplicity at $\sqrt{s_{NN}} = 7.7$ GeV. For R_{CP} the N_{bin} uncertainties for the central and peripheral bins are considered 100% correlated when determining the scale uncertainty. The systematic uncertainty from the feed-down correction is assumed to

be uncorrelated with centrality and dominates for R_{CP} . For Y , the N_{bin} uncertainty is combined in quadrature with the other systematic uncertainties and dominates for peripheral collisions while the uncertainty from the feed-down correction dominates for central collisions.

Chapter 7

Results

This chapter discusses results derived from charged hadron data collected as a function of p_T , centrality, and $\sqrt{s_{NN}}$ after corrections from chapter 5 have been applied. Section 1 shows p_T -spectra for each centrality and $\sqrt{s_{NN}}$ in the RHIC BES. All of the other results in this chapter are derived from these spectra, or from the spectra of negative charged hadrons only. Section 2 shows the $\sqrt{s_{NN}}$ dependence of $\langle p_T \rangle$ for each centrality. Section 3 presents the charged hadron R_{CP} results for each $\sqrt{s_{NN}}$. The fractional energy-loss, S_{loss} , is shown as a function of p_T for each collision energy in section 4. In the last section results from the newly developed observable, $Y(N_{part})$, are shown for each $\sqrt{s_{NN}}$.

The results and basic descriptions of the plots are included in this chapter. The next chapter will discuss the results in greater detail with physics interpretations.

7.1 p_T -spectra

Fully corrected charged hadron p_T -spectra measured in $|\eta| < 0.5$ are shown in Fig. 7.1. The spectra are shown for 0-5%, 5-10%, 10-20%, 20-40%, 40-60%, and 60-80% centralities in $\sqrt{s_{NN}} = 7.7, 11.5, 14.5, 19.6, 27, 39, \text{ and } 62.4 \text{ GeV}$ collisions. The p_T reach generally increases for more central spectra, except in a few cases where the

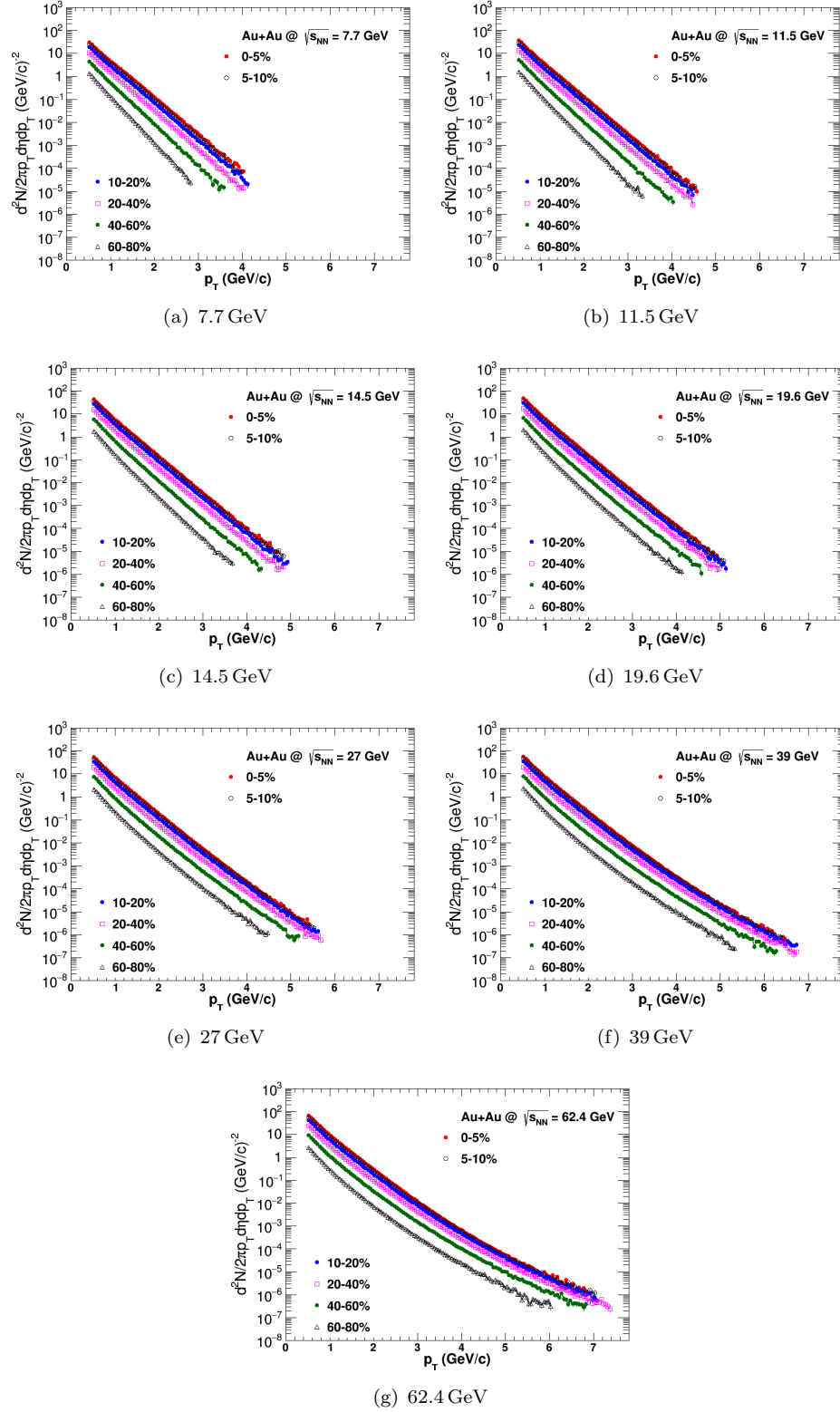


FIGURE 7.1 Corrected charged hadron spectra for each $\sqrt{s_{NN}}$ and centrality bin as a function of p_T and measured in $|\eta| < 0.5$. Systematic uncertainty bands are shown but are generally smaller than the symbol size.

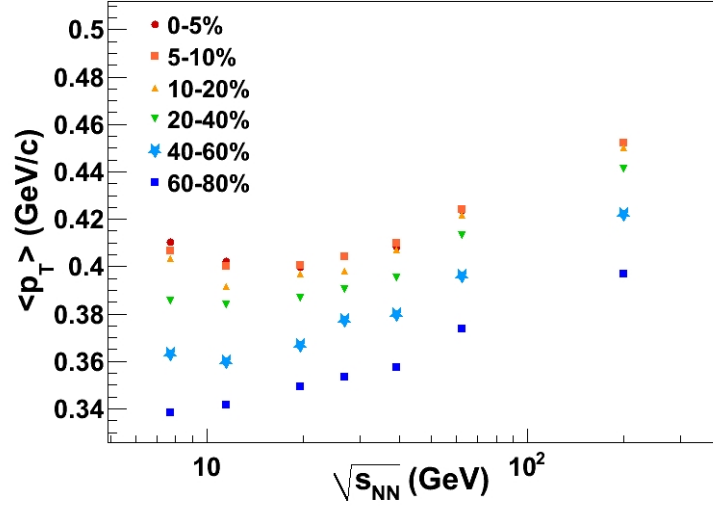


FIGURE 7.2 Charged hadron $\langle p_T \rangle$ in $|\eta| < 0.5$ for $\sqrt{s_{NN}} = 7.7, 11.5, 14.5, 19.6, 27, 39,$ and 62.4 GeV and in 0-5%, 5-10%, 10-20%, 20-40%, 40-60%, and 60-80% centrality bins. The error bars on the points are from statistical uncertainty only and are smaller than the markers. The systematic uncertainties would be highly correlated with centrality and $\sqrt{s_{NN}}$ with the dominant uncertainties arising from tracking efficiency and feed-down corrections. The point-to-point systematic uncertainties should be smaller than 0.01 GeV/c

narrower centrality bins of the most central spectra result in fewer measured tracks and a reduced p_T reach. The spectra fall more steeply for lower $\sqrt{s_{NN}}$ and there is also a strong centrality dependence to the slopes at lower $\sqrt{s_{NN}}$. Systematic uncertainties from the feed-down, momentum resolution, and tracking efficiency corrections are included in Fig. 7.1, but are generally too small to be seen.

The p_T -inclusive yields ($dN/d\eta$) have a strong dependence on centrality, increasing with increasing N_{part} . They have a weaker dependence on collision energy, but also increase with $\sqrt{s_{NN}}$.

7.2 $\langle p_T \rangle$

Fits to the charged hadron p_T -spectra can be used to determine $\langle p_T \rangle$,

$$\langle p_T \rangle = \frac{\int_0^\infty p_T \frac{d^2 N}{dp_T d\eta}(p_T) dp_T}{\int_0^\infty \frac{d^2 N}{dp_T d\eta}(p_T) dp_T}, \quad (7.1)$$

for the various centralities and collision energies. Figure 7.2 shows these results with statistical errors only. An exponential fit at low- p_T was used for the extrapolation to $p_T = 0$ GeV/c. The fit function was only used to extrapolate to $p_T = 0$ GeV/c with the bin contents above $p_T = 0.2$ GeV/c summed together and then added to the integral of the fit at low- p_T . The systematic uncertainties due to the feed-down correction, the tracking efficiency, centrality determination, choice of fit function, and due to the fit's low- p_T extrapolation were not evaluated here. These uncertainties would be highly correlated with $\sqrt{s_{NN}}$ and centrality.

$\langle p_T \rangle$ increases monotonically as a function of $\sqrt{s_{NN}}$ for 60-80% peripheral collisions, but has a minimum in $11.5 < \sqrt{s_{NN}} < 27$ GeV for 0-5% central collisions. Because the systematic uncertainties in this measurement are highly correlated with $\sqrt{s_{NN}}$, this non-monotonic trend is likely significant. $\langle p_T \rangle$ increases monotonically with N_{part} for a given $\sqrt{s_{NN}}$.

7.3 R_{CP}

Figure 7.3 shows fully corrected charged hadron R_{CP} for 0-5% central over 60-80% central collisions and for $\sqrt{s_{NN}} = 7.7, 11.5, 14.5, 19.6, 27, 39,$ and 62.4 GeV in $|\eta| < 0.5$. The error bars indicate statistical uncertainties while the boxes on the points indicate systematic uncertainties from the feed-down correction. Other systematic uncertainties were taken to be 100% correlated with centrality so that they are greatly reduced in the ratio. The colored bands at unity on the right side of the plot are for the systematic

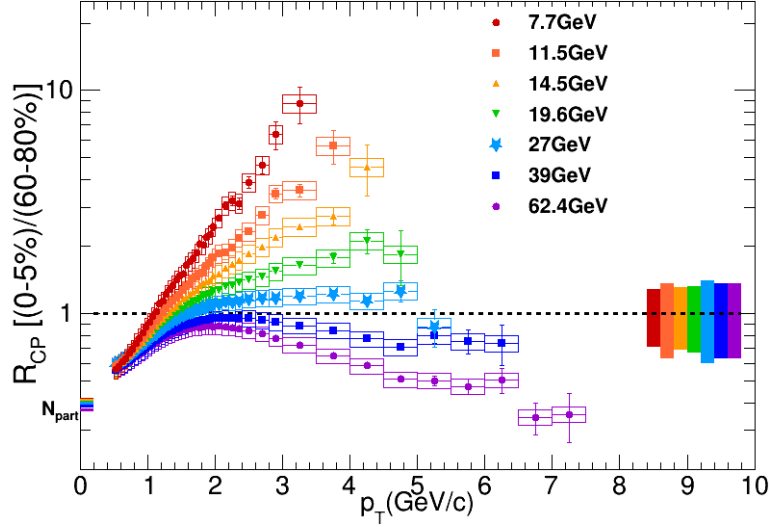


FIGURE 7.3 Charged hadron R_{CP} in $|\eta| < 0.5$ are shown for $\sqrt{s_{NN}} = 7.7, 11.5, 14.5, 19.6, 27, 39,$ and 62.4 GeV. N_{part} scaling is indicated for each collision energy by the colored lines at $p_T = 0$ GeV/c. The error bands at unity on the right side of the plot indicate the N_{bin} scaling uncertainty. The error bars on the points are for their statistical uncertainty and the boxes on the points are for their systematic uncertainties.

uncertainty from N_{bin} scaling. These uncertainties were also taken to be 100% correlated with centrality, but remain the dominant scale uncertainty for the ratio, R_{CP} .

Charged hadron R_{CP} at $\sqrt{s_{NN}} = 62.4$ GeV demonstrates net suppression¹ at high- p_T . If the scale uncertainties are taken into account, R_{CP} is consistent with unity for $\sqrt{s_{NN}} = 39$ and 27 GeV at high- p_T . As the $\sqrt{s_{NN}}$ is further reduced, high- p_T enhancement becomes increasingly dominant until R_{CP} at $\sqrt{s_{NN}} = 7.7$ GeV is enhanced by an order of magnitude. In fact, as a consequence of all the $\sqrt{s_{NN}} = 7.7$ GeV p_T -spectra decreasing exponentially, but with different slopes, R_{CP} at this same energy increases exponentially as a function of p_T .

The charged hadron R_{CP} for all of the collision energies is suppressed relative to unity at low- p_T and converge toward N_{part} scaling values. The low- p_T trends do not all converge on N_{part} scaling exactly, but depend on the species. Dr. Evan Sangaline's PhD. thesis dealt with identified $\pi^\pm, K^\pm, p,$ and \bar{p} R_{CP} in $|y| < 0.25$ for $\sqrt{s_{NN}} = 7.7, 11.5, 19.6, 27,$

¹Meaning that the combined effects that cause enhancement are overwhelmed by effects leading toward suppression.

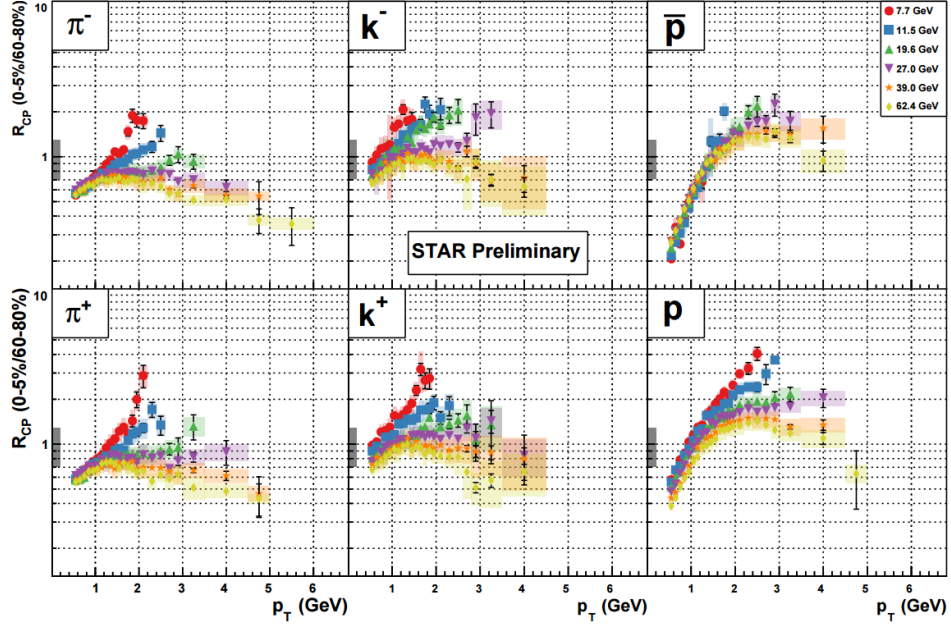


FIGURE 7.4 Identified π^\pm , K^\pm , p , and \bar{p} R_{CP} in $|y| < 0.25$ is shown for $\sqrt{s_{NN}} = 7.7, 11.5, 19.6, 27, 39,$ and 62.4 GeV. The gray boxes at unity on the left side of the plot indicate the N_{bin} scaling uncertainty. The error bars on the points are for their statistical uncertainty and the boxes on the points are for their systematic uncertainties [90].

39, and 62.4 GeV and is shown in Fig. 7.4 [90]. He found that low- p_T baryons were more suppressed than mesons due to radial flow. Although the p_T reach is limited relative to charged hadron R_{CP} , a similar energy ordering at intermediate to high p_T is observed for the identified species. It is worth noting that the baryon R_{CP} s are enhanced relative to the meson R_{CP} s at intermediate to high- p_T .

If baryons are more affected by enhancement effects, this motivates investigating the R_{CP} of h^- since this observable would converge toward the R_{CP} of π^- as the $\sqrt{s_{NN}}$ is reduced while still having a higher p_T reach than if the pion yields were being extracted from dE/dx and time-of-flight measurements. Figure 7.5 shows negative charged hadron, h^- , R_{CP} in $|\eta| < 0.5$ for $\sqrt{s_{NN}} = 7.7, 11.5, 14.5, 19.6, 27, 39,$ and 62.4 GeV. As for the charged hadron R_{CP} in Fig. 7.3, the error bars indicate statistical uncertainties while the boxes on the points indicate systematic uncertainties from the feed-down correction. Here the feed-down correction was for negative daughters only. Other systematic uncertainties

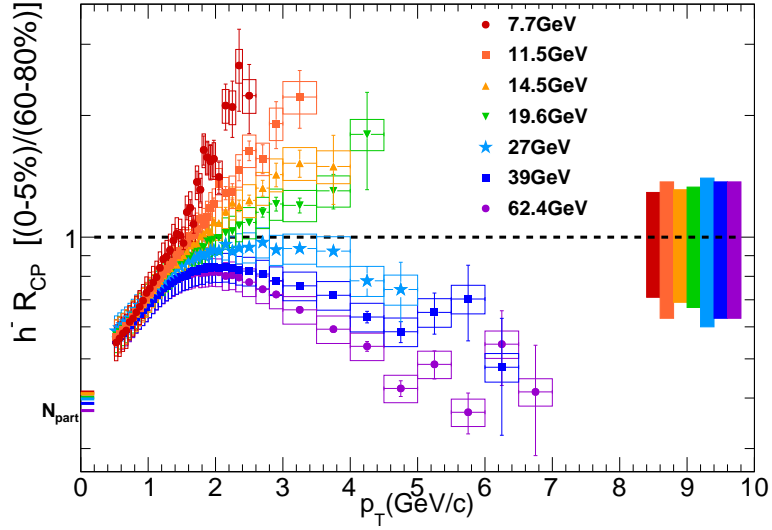


FIGURE 7.5 Negative charged hadron R_{CP} in $|\eta| < 0.5$ is shown for $\sqrt{s_{NN}} = 7.7, 11.5, 14.5, 19.6, 27, 39,$ and 62.4 GeV. N_{part} scaling is indicated for each collision energy on the y-axis. The error bands at unity on the right side of the plot indicate the N_{bin} scaling uncertainty. The error bars on the points are for their statistical uncertainty and the boxes on the points are for their systematic uncertainties.

were taken to be 100% correlated with centrality so that they are greatly reduced in the ratio. The colored bands at unity on the right side of the plot are for the systematic uncertainty from N_{bin} scaling. These uncertainties were also taken to be 100% correlated with centrality, but remain the dominant scale uncertainty for the ratio, R_{CP} .

As expected based on Fig. 7.4, $h^- R_{CP}$ is significantly suppressed at high- p_T relative to the inclusive charged hadron R_{CP} . However, the scaling uncertainties remain too large for us to make stronger conclusions about which collision energies exhibit net suppression from the $h^- R_{CP}$ than we did for inclusive charged hadron R_{CP} .

7.4 S_{loss}

While R_{CP} measures the change in scaled yields for a given p_T bin, one might assume that the high- p_T yields are actually constant and that it is just their momenta that are modified to shuffle them into different p_T bins. $S_{loss} = \delta p_T / p_T$ is constructed to

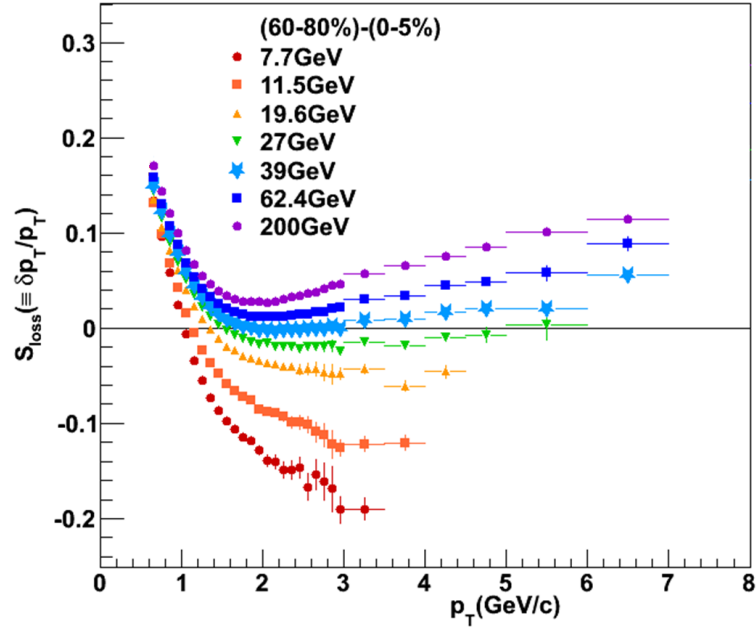


FIGURE 7.6 Charged hadron S_{loss} in $|\eta| < 0.5$ is shown for $\sqrt{s_{NN}} = 7.7, 11.5, 14.5, 19.6, 27, 39, 62.4,$ and 200 GeV. Systematic uncertainties due to N_{bin} scaling would dominate the uncertainties of this measurement and are $\approx 4\%$.

measure the fractional momentum-loss, or gain, of central spectra relative to N_{bin} scaled peripheral spectra. This is done by measuring the momentum shift from the scaled peripheral spectra to the central for a fixed yield. Such a model would only work where N_{bin} scaling is valid and at sufficiently high p_T to minimize the modifications to the yields from coalescence, recombination, gluon fusion, and annihilation.

Figure 7.6 is constructed from the same spectra that were used to construct the charged hadron R_{CP} in the previous section. The peripheral spectra were fit by a series of exponentials in order to give precise extrapolations between the data points when determining δp_T . The rise at low- p_T corresponds to the region where N_{bin} scaling breaks down. There is positive energy-loss for $\sqrt{s_{NN}} > 27$ GeV at high p_T and negative energy-loss for $\sqrt{s_{NN}} < 27$ GeV at high p_T .

Figure 7.7 shows a similar result for negative charged hadrons only. While the high- p_T energy loss is similar for inclusive charged hadrons and negative charged hadrons for

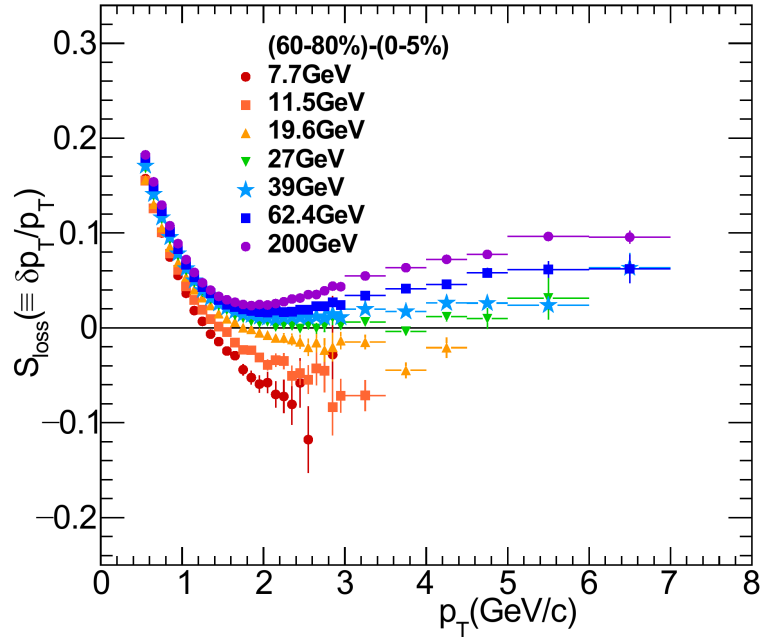


FIGURE 7.7 Negative charged hadron S_{loss} in $|\eta| < 0.5$ is shown for $\sqrt{s_{NN}} = 7.7, 11.5, 14.5, 19.6, 27, 39, 62.4,$ and 200 GeV. Systematic uncertainties due to N_{bin} scaling would dominate the uncertainties of this measurement and are $\approx 4\%$.

high $\sqrt{s_{NN}}$, the inclusive charged hadron energy-loss is more negative than the negative charged hadron energy loss for low $\sqrt{s_{NN}}$.

7.5 Y

$Y(N_{part})$ is shown for two p_T ranges and for $\sqrt{s_{NN}} = 7.7, 11.5, 14.5, 19.6, 27, 39, 62.4,$ and 200 GeV in Fig. 7.8. For $p_T > 3.5$ GeV/c, fewer collision energies are shown due to p_T limits. The distribution for each $\sqrt{s_{NN}}$ is normalized by their most peripheral bin so that the shapes of the distributions for each $\sqrt{s_{NN}}$ may be more directly compared. The systematic uncertainty bands on the points are dominated by the uncertainty on N_{bin} at low N_{part} and by the feed-down uncertainty at high N_{part} . Momentum resolution and tracking efficiency uncertainties are highly correlated with centrality and so are suppressed. Figure 7.11 shows the same measurement but for negative charged hadrons rather than inclusive charged hadrons.

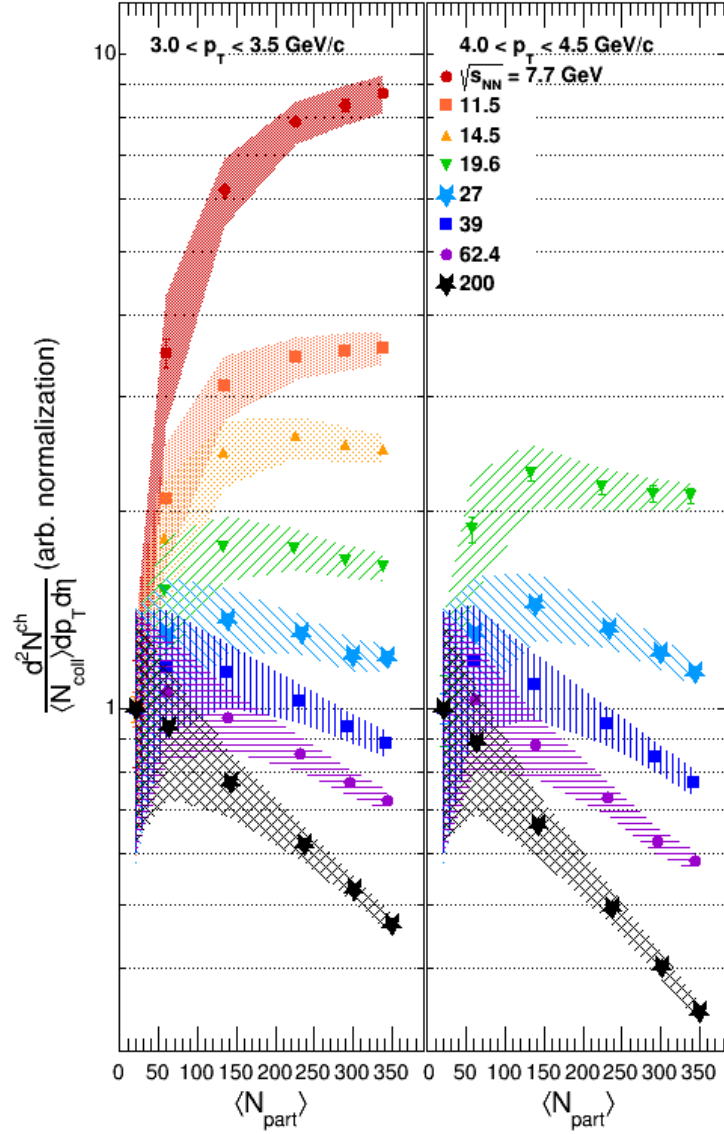


FIGURE 7.8 Charged hadron $Y(N_{\text{part}})$ in $|\eta| < 0.5$ for $\sqrt{s_{\text{NN}}} = 7.7, 11.5, 14.5, 19.6, 27, 39, 62.4,$ and 200 GeV . The statistical uncertainty bars are mostly smaller than the marker sizes. The error band is the quadrature sum of the uncertainty on N_{bin} and the uncertainty from the feed-down correction. The left panel shows Y for $3 < p_T < 3.5 \text{ GeV/c}$ while the right panel shows Y for $4 < p_T < 4.5 \text{ GeV/c}$.

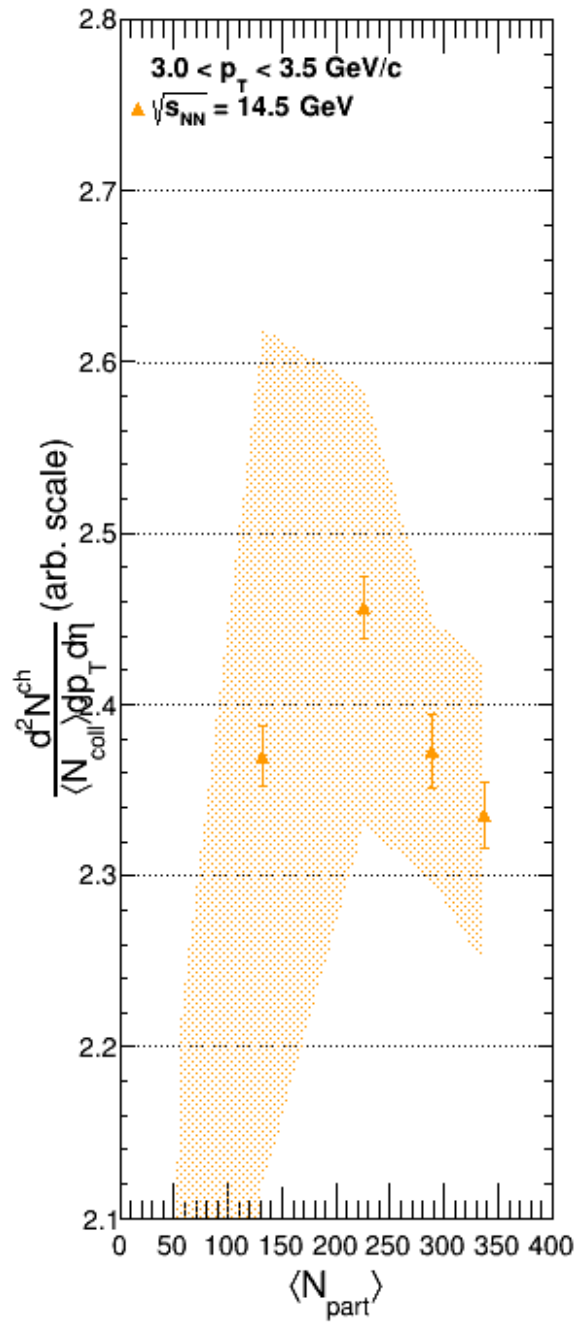


FIGURE 7.9 Charged hadron $Y(N_{\text{part}})$ in $|\eta| < 0.5$ for $\sqrt{s_{\text{NN}}} = 14.5 \text{ GeV}$. The statistical uncertainty bars are mostly smaller than the marker sizes. The error band is the quadrature sum of the uncertainty on N_{bin} and the uncertainty from the feed-down correction.

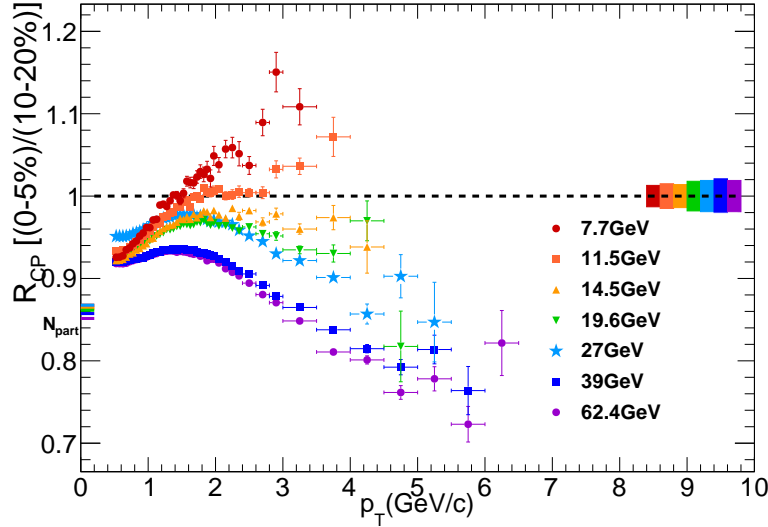


FIGURE 7.10 Charged hadron [(0-5%)/(10-20%)] R_{CP} in $|\eta| < 0.5$ is shown for $\sqrt{s_{NN}} = 7.7, 11.5, 14.5, 19.6, 27, 39,$ and 62.4 GeV. N_{part} scaling is indicated for each collision energy on the y-axis. The error bands at unity on the right side of the plot indicate the N_{bin} scaling uncertainty. The error bars on the points are for their statistical uncertainty while the highly correlated point-to-point systematic uncertainties are suppressed.

Y at $\sqrt{s_{NN}} = 200$ GeV decreases monotonically with increasing N_{part} for both p_T ranges in Fig. 7.8. Y from 7.7 and 11.5 GeV collisions increase monotonically with increasing N_{part} for $3 < p_T < 3.5$ GeV/c. The other collision energies contain non-monotonic dependencies on N_{part} , first increasing and then decreasing. At higher $\sqrt{s_{NN}}$, Y “turns over” at lower N_{part} and the lower the $\sqrt{s_{NN}}$, the later the distribution “turns over”.

For every $\sqrt{s_{NN}} > 11.5$ GeV, Y in the most central 0-5% centrality bin is suppressed relative to Y in the 10-20% centrality bin with the case of $\sqrt{s_{NN}} = 14.5$ GeV shown in Fig. 7.9. This motivates constructing an “ R_{CP} ” where the peripheral 60-80% centrality bin is replaced by the 10-20% centrality bin so that the full p_T dependence of this variable may be investigated. This is done in Fig. 7.10. Here the systematic uncertainties have been suppressed since even the feed-down correction can be assumed to be 100% correlated between two centrality bins that are so close to each-other. The uncertainty bands at unity on the right correspond to the uncertainties from the N_{bin} scaling which were also taken to be 100% correlated. In order to improve readability of this plot, points with

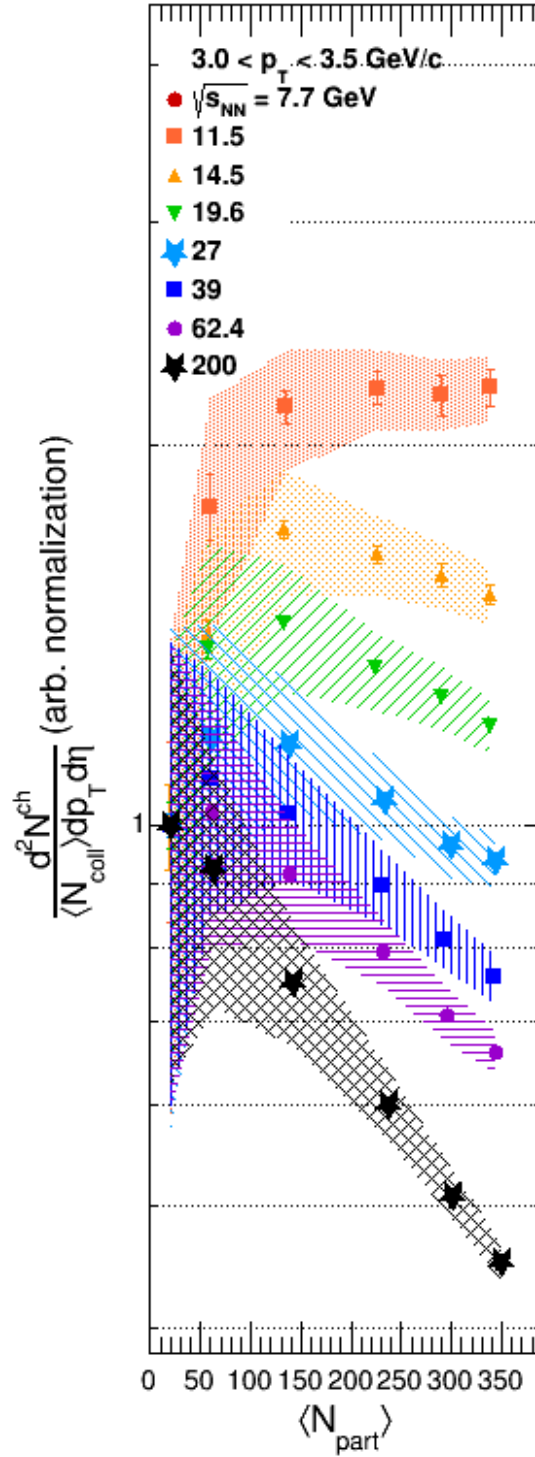


FIGURE 7.11 Negative charged hadron $Y(N_{\text{part}})$ in $|\eta| < 0.5$ for $3 < p_T < 3.5 \text{ GeV}/c$ and for $\sqrt{s_{\text{NN}}} = 7.7, 11.5, 14.5, 19.6, 27, 39, 62.4, \text{ and } 200 \text{ GeV}$. The statistical uncertainty bars are mostly smaller than the marker sizes. The error band is the quadrature sum of the uncertainty on N_{bin} and the uncertainty from the feed-down correction.

absolute statistical uncertainties greater than 0.05 have been removed. These points followed the trends of the points that are shown within their uncertainties, but cluttered up the plot unnecessarily. Figure 7.10 exhibits net suppression for charged hadrons in 0-5% central collisions relative to those in 10-20% central collisions at $\sqrt{s_{\text{NN}}} = 14.5, 19.6, 27, 39, \text{ and } 62.4 \text{ GeV}$.

To increase the fraction of pions in this measurement Fig. 7.11 shows $Y(N_{\text{part}})$ for negative charged hadrons only. Here the $\sqrt{s_{\text{NN}}} = 14.5 \text{ GeV}$ data is more clearly decreasing as a function of N_{part} and the 11.5 GeV data constant versus N_{part} for $N_{\text{part}} > 100$.

Chapter 8

Discussion

This chapter dives into possible physics interpretations for the results from the previous chapter. The sections are ordered in the same sequence as in the previous chapter.

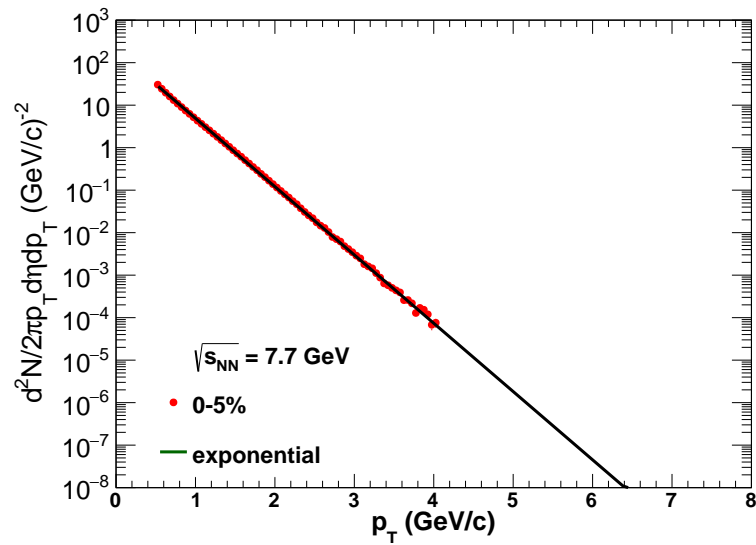


FIGURE 8.1 Charged hadron 0-5% central p_T -spectra in $|\eta| < 0.5$ is shown for $\sqrt{s_{NN}} = 7.7 \text{ GeV}$ Au+Au collisions with an exponential fit.

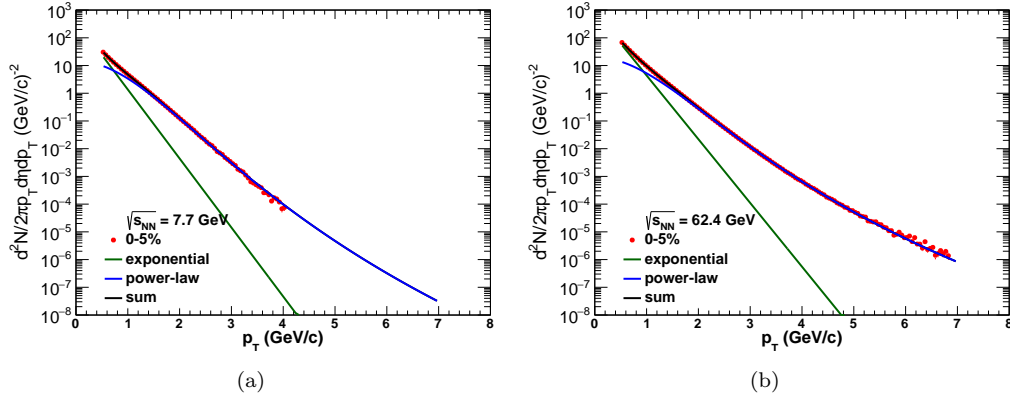


FIGURE 8.2 Corrected charged hadron p_T -spectra for 0-5% central Au+Au collisions at $\sqrt{s_{NN}} = 7.7$ (a) and 62.4 GeV (b) with two component fits. The exponential contribution to the fit is shown with the green curve while the power-law contribution is shown with the blue curve.

8.1 Spectra

The corrected p_T -spectra at low $\sqrt{s_{NN}}$ are well described by exponentials, as shown in Fig. 8.1 for 0-5% central Au+Au collisions at $\sqrt{s_{NN}} = 7.7$ GeV. However, as the $\sqrt{s_{NN}}$ is increased a high- p_T power-law tail develops. This motivates using a two component model to describe the spectra [52]:

$$\frac{d^2N}{2\pi p_T d\eta dp_T} = A_e \cdot \exp(-p_T/T_e) + \frac{A}{(1 + \frac{p_T^2}{T^2 \cdot n})^n}, \quad (8.1)$$

where A_e , T_e , A , T , and n are the fit parameters. The only limits imposed on the fits were that A_e and A should be positive. The exponential term describes a simple thermal system at low p_T while the power-law term describes mid to high- p_T fragmentation. Replacing the exponential term with a Blast-Wave formula [91] would provide a more physically accurate description of the radially expanding emission source, but the simpler exponential function is sufficient to motivate particle production from at least two separate processes at higher $\sqrt{s_{NN}}$.

Figure 8.2 shows fits to 0-5% central charged hadron p_T -spectra for $\sqrt{s_{NN}} = 7.7$ and 62.4 GeV using this two component model. Although the 7.7 GeV data were previously

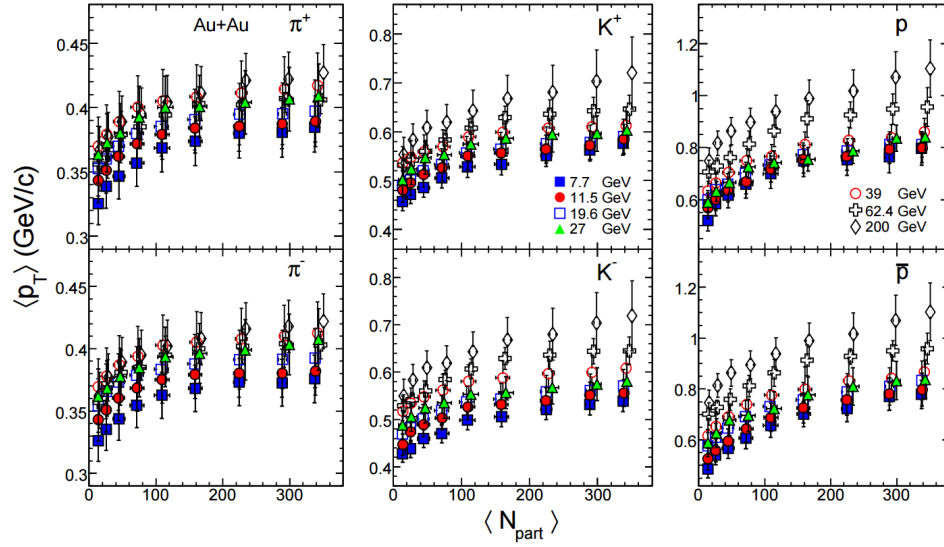


FIGURE 8.3 $\langle p_T \rangle$ for identified species in the BES [89].

well constrained by an exponential alone, the two component fit favors a large contribution from the power-law. Fits such as these can be improved by constraining the parameters with other data. For example, the exponential slope parameter in these fits could be constrained with exponential fits in the low- p_T region before performing the two component fit over the entire p_T range. Also, the various parameters in this fit are related to physical quantities and would be expected to have certain trends as a function of N_{part} . For example, the exponential slope parameters are related to the temperatures of the emission sources. These “temperatures” would be expected to increase monotonically with N_{part} . This is clearly the case in Fig. 7.1(a).

8.2 $\langle p_T \rangle$

Non-monotonic trends with $\sqrt{s_{NN}}$ are very exciting for some observables where they are taken as possible signatures for a critical point or a softest point in the equation of state. This means we want to consider carefully the physics that might drive this observable.

One might expect $\langle p_T \rangle$ to increase monotonically with both $\sqrt{s_{NN}}$ and N_{part} . This would be driven by hydrodynamic flow, especially radial flow, boosting particles to higher p_T .

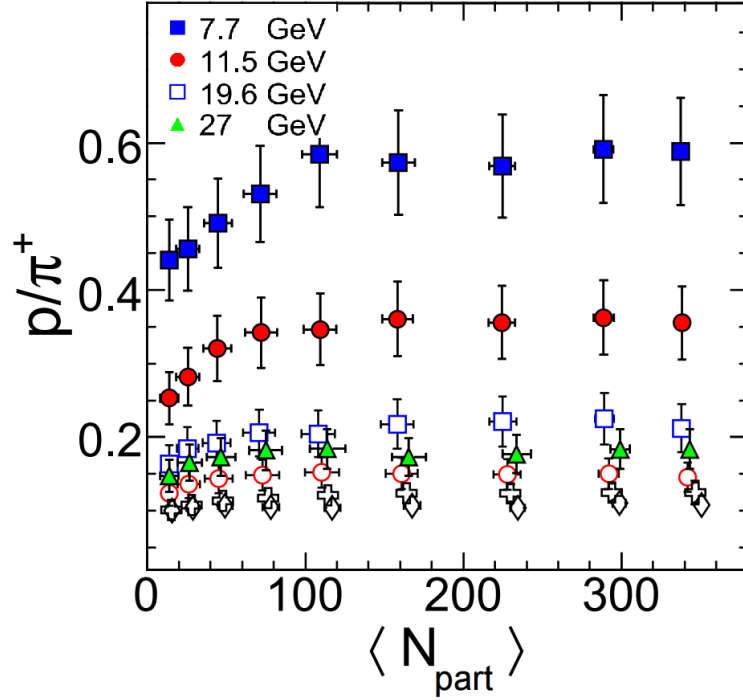


FIGURE 8.4 p/π as a function of N_{part} for $\sqrt{s_{\text{NN}}} = 7.7, 11.5, 19.6, 27, 39, 62.4,$ and 200 GeV [89].

The higher phase space density in central collisions and at higher $\sqrt{s_{\text{NN}}}$ might also be expected to increase the contribution of coalescence to hadronization, which would also cause $\langle p_{\text{T}} \rangle$ to increase with N_{part} and $\sqrt{s_{\text{NN}}}$. The non-monotonic shape versus $\sqrt{s_{\text{NN}}}$ for high N_{part} is somewhat surprising then. Recall however that these are inclusive charged hadron spectra. The p/π ratios can vary with N_{part} and each species can be expected to have a different $\langle p_{\text{T}} \rangle$ for a given $\sqrt{s_{\text{NN}}}$ and N_{part} with $\langle p_{\text{T}} \rangle_p > \langle p_{\text{T}} \rangle_\pi$ as shown in Fig. 8.3 [89]. The non-monotonic behavior for the charged hadrons at low $\sqrt{s_{\text{NN}}}$ and high N_{part} is then driven by the increase in $\langle p_{\text{T}} \rangle_p$ with N_{part} and the high p/π at low $\sqrt{s_{\text{NN}}}$, as shown in Fig. 8.4 [89]. The $\langle p_{\text{T}} \rangle$ follows the expected trends for the individual species and it is just the particle ratios that drive the non-monotonic trends in charged hadron $\langle p_{\text{T}} \rangle$ for central collisions at low $\sqrt{s_{\text{NN}}}$.

8.3 R_{CP}

High- p_T charged hadrons are suppressed in 0-5% central Au+Au collisions at $\sqrt{s_{NN}} = 62.4$ GeV relative to 60-80% peripheral collisions. They are less suppressed than in $\sqrt{s_{NN}} = 200$ GeV data and are energy ordered with suppression giving way to enhancement between $\sqrt{s_{NN}} = 39$ and 27 GeV. This means that suppression of high- p_T charged hadrons, as a signature for the formation of QGP in heavy-ion collisions, “turns off” between $\sqrt{s_{NN}} = 39$ and 27 GeV. However the strong enhancement at lower $\sqrt{s_{NN}}$ suggests that processes that lead to enhancement are competing with partonic energy-loss so that this signature has a reduced sensitivity to the actual minimum energy required to form a QGP.

The strength of the enhancement increases with decreasing $\sqrt{s_{NN}}$ until the lowest collision energy in the RHIC BES where R_{CP} increases exponentially with p_T . This is driven by the fact that the spectra at this energy are themselves well described by exponentials with different temperature parameters so that their ratios give another exponential. This may mean that the spectra are dominated by a thermalized bulk at all p_T for this energy. Because the spectra at lower $\sqrt{s_{NN}}$ fall much more steeply than at higher $\sqrt{s_{NN}}$, there are fewer high- p_T partons to fragment down to lower p_T . It may be that with a larger p_T reach, from additional data, the R_{CP} at more of these $\sqrt{s_{NN}}$ would eventually turn over as p_T bins were reached with increasing relative contributions from fragmentation versus bulk physics. While there are several sources of enhancement that come from interactions with cold nuclear matter or from hadronic interactions, these sources may not be sufficient to describe the degree of enhancement observed at $\sqrt{s_{NN}} = 7.7$ GeV.

Another source of enhancement would be coalescence. Combining low- p_T partons into a higher p_T hadron would lead to enhancement, and it may be that much of the enhancement at $\sqrt{s_{NN}} = 7.7$ GeV derives from this source. If so then this would be another signature for the production of QGP. One way to test this idea would be to look at nuclear modification factors from collision energies lower than $\sqrt{s_{NN}} = 7.7$ GeV where we do not expect to be forming a QGP to see if the nuclear modification factor decreases.

It might be useful to do this for negative charged hadrons only to reduce complications from changing particle ratios with larger enhancement effects for protons.

8.4 S_{loss}

Here we are measuring the shift in the spectra to higher or lower p_T rather than taking ratios at fixed p_T . This is useful because the spectra decrease as a function of p_T faster at lower $\sqrt{s_{NN}}$ so that the same shift in p_T results in a larger enhancement or suppression of the modified spectra relative to the reference spectra. A decrease in p_T at high- p_T is expected to be driven by partonic energy-loss. At lower p_T there may be several processes that would lead to enhancement. These include p_T -broadening in cold nuclear matter, radial flow, and coalescence.

Anywhere that R_{CP} is greater than unity, S_{loss} is negative as “energy” was gained rather than lost. This may actually be driven by additional particle production rather than by shifts in p_T so R_{CP} and S_{loss} are complementary measurements from the same spectra under different assumptions.

Interestingly, the magnitude of the S_{loss} turns out to be energy ordered with $\sqrt{s_{NN}} = 7.7$ GeV exhibiting larger increases in p_T than $\sqrt{s_{NN}} = 11.5$ GeV. This may mean that a larger fraction of the particles at each p_T originate from coalescence for 7.7 GeV collisions than for 11.5 GeV collisions. It may also be driven by a change in the particle ratios between the two energies with 7.7 GeV collisions having more protons than 11.5 GeV collisions and protons being shifted more by radial flow and other processes.

By measuring S_{loss} for negative charged hadrons, which are pion dominated for $\sqrt{s_{NN}} = 7.7$ and 11.5 GeV, it is possible to disentangle whether the particle ratios or the relative contributions of coalescence and fragmentation to the hadronization process drive the larger p_T shift measured for 7.7 GeV collisions. The measurement supports an increase in the fraction of the hadronization for a given p_T in $\sqrt{s_{NN}} = 7.7$ GeV collisions relative to 11.5 GeV collisions. The difference in S_{loss} between $\sqrt{s_{NN}} = 7.7$ and 11.5 GeV is

smaller for negative charged hadrons than for inclusive charged hadrons meaning that the higher fraction of protons in $\sqrt{s_{\text{NN}}} = 7.7$ GeV collisions is responsible for some of the enhancement at this energy. However negative charged hadrons at $\sqrt{s_{\text{NN}}} = 7.7$ GeV still have a larger p_{T} shift than negative charged hadrons in 11.5 GeV collisions. This may be driven by the fraction of the hadrons in each p_{T} bin that originate from lower p_{T} partons coalescing to hadrons. These lower p_{T} partons would have larger p_{T} gains from radial flow in the partonic phase and the final hadron would gain p_{T} from all of its constituents rather than just one.

8.5 Y

By investigating N_{bin} -scaled yields as a function of N_{part} the modifications due to enhancement and suppression are partially disentangled. For low N_{part} , enhancement effects increase faster than suppression effects as a function of N_{part} for $\sqrt{s_{\text{NN}}} < 200$ GeV. However the 62.4 GeV data quickly turns over and suppression effects increase faster than enhancement effects for most N_{part} . As the collision energy is reduced, you have to go more and more central before a centrality is reached where suppression effects increase faster than enhancement effects. Using this method, evidence for partonic energy-loss is found for $\sqrt{s_{\text{NN}}} \geq 14.5$ GeV.

Using identified π^{\pm} , K^{\pm} , p , and \bar{p} spectra from the BES energies [90], $Y(N_{\text{part}})$ for each of these species is constructed. The p_{T} reach is more limited for these identified species. Results for $2.4 < p_{\text{T}} < 2.6$ GeV/c are shown in Fig. 8.5. The inclusive systematic uncertainties on the spectra from Evan Sangaline's thesis are added in quadrature with the systematic uncertainties on N_{bin} . $Y(N_{\text{part}})$ for protons and anti-protons is nearly flat as a function of centrality for $N_{\text{part}} \geq 150$. Kaons are enhanced relative to pions. π^{+} and π^{-} are similar with $Y(N_{\text{part}})$ exhibiting suppression for $\sqrt{s_{\text{NN}}} \geq 19.6$ GeV and nearly flat for 11.5 GeV.

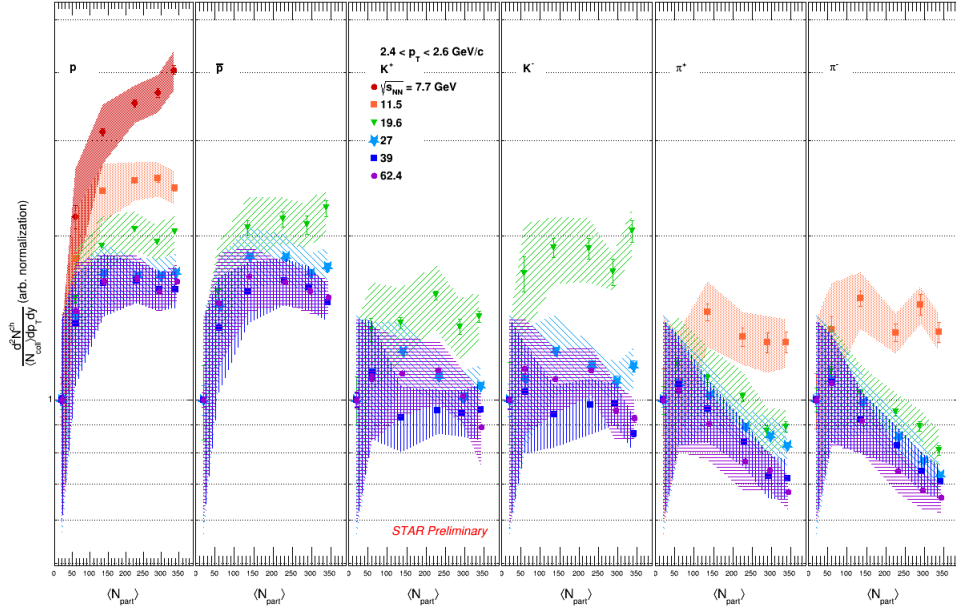


FIGURE 8.5 Identified p , \bar{p} , K^\pm , and π^\pm $Y(N_{\text{part}})$ in $|y| < 0.25$ is shown for $\sqrt{s_{NN}} = 7.7, 11.5, 19.6, 27, 39,$ and 62.4 GeV. The error bands are the quadrature sum of the uncertainties on N_{bin} , from the feed-down correction, from the tracking efficiency, and from the particle identification procedure [90].

The mean impact parameter in 0-5% collisions for these energies is 2.3 ± 1.1 fm while in 10-20% collisions the mean impact parameter is 5.6 ± 2.2 fm. This suggests that the mean in-medium pathlength is significantly longer in 0-5% collisions. So the suppression of high- p_T inclusive charged hadrons and negative charged hadrons in 0-5% central Au+Au collisions relative to 10-20% central collisions is consistent with pathlength dependent partonic energy-loss.

This measurement of $Y(N_{\text{part}})$ motivated constructing an R_{CP} where 10-20% central data is used as the reference, shown in Fig. 7.10. In this case we see that the suppression of the 0-5% data was not a coincidence of the chosen p_T range and is in fact a robust measurement of suppression.

Chapter 9

Modeling Heavy-Ion Collisions

The collection of physical processes that modify p_T spectra are in reality too complicated to be described by simple fits to spectra. More physically accurate models describe initial state and cold nuclear matter effects, produce partons at all phases of the collision, model a partonic phase that starts out-of-equilibrium, correctly handle the modification of high- p_T partons interacting with the medium, hadronize the partons through the correct combination of fragmentation at high- p_T and coalescence at low- p_T , describe hadronic interactions up to freeze-out, and decay short lived particles at the appropriate times throughout the collision evolution.

Models with these components provide a possible method for disentangling partonic energy-loss from the various enhancement effects in heavy-ion collisions. If a model can reproduce many observables over a broad range of kinematics then the model likely gets the relative contributions of each source of modification correct. By comparing the data to the model with jet quenching absent one could obtain an estimate for the modification due to jet-quenching. Even if the model does not describe jet-quenching itself very well, if the model can be validated in regions with minimal partonic energy-loss then a comparison with the model where the model's partonic energy-loss processes were turned off could still provide evidence for suppression in the data relative to such a model.

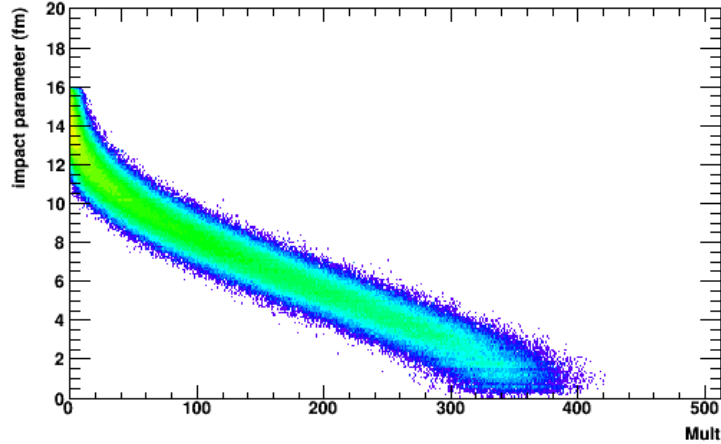


FIGURE 9.1 The correlation of impact parameter with charged multiplicity in $|\eta| < 0.5$ at $\sqrt{s_{NN}} = 14.5$ GeV from UrQMD.

p_T spectra are constructed from charged hadrons that are effected by every phase of heavy-ion collisions. Models that attempt to quantitatively describe data must accurately describe initial state effects, the pre-equilibrium phase, partonic transport, hadronization, hadronic rescattering, and final-state decays. To describe p_T integrated yields only requires getting the net effects for the bulk right, but differential yields require getting the physics at every phase and in every kinematic region quantitatively right. This is a tall order. As Bylinkin, Chernyavskaya, and Rostovtsev said in a recent paper on two component models for charged particle production, “*there is no single theoretical approach that can simultaneously describe both low- p_T and high- p_T hadron production*” [52]. Models that simulate heavy-ion collisions use many components to describe the different kinematic regions and phases of medium production and evolution. These models often focus on getting a particular type of physics right, so they may not do well at simulating physics that was not the focus of the model as it was being constructed. For example, models that include hydrodynamic phases in order to describe the evolution of low- p_T correlations in the bulk may not do well at describing high- p_T processes.

Monte Carlo event generators use different, sometimes interchangeable, models to describe each component of a heavy-ion collision. They typically begin with a set of randomized initial conditions. For the models discussed in this chapter, those initial conditions

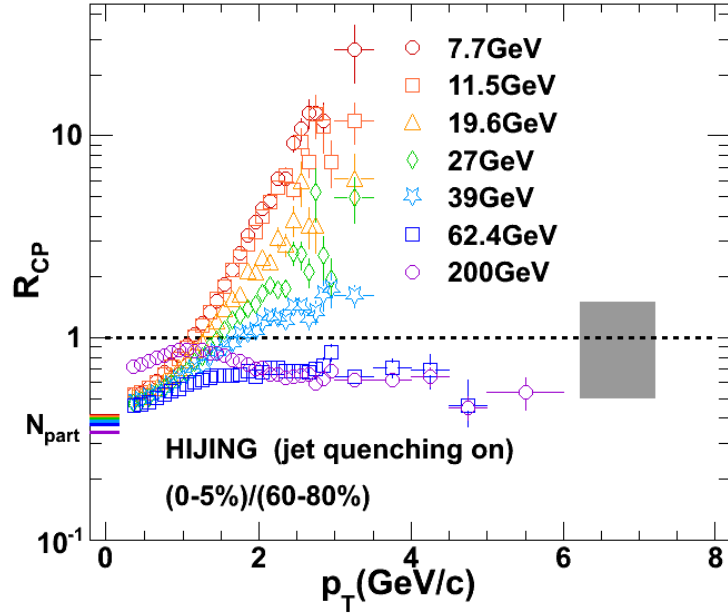


FIGURE 9.2 HIJING generated charged hadron R_{CP} in $|\eta| < 0.5$ are shown for $\sqrt{s_{NN}} = 7.7, 11.5, 19.6, 27, 39, 62.4,$ and 200 GeV for 0-5% over 60-80% centrality bins.

are provided event-by-event using a Glauber Monte Carlo. From there, each model includes different components to describe particle production and evolution. Theorists often select on centrality classes using impact parameters, but experimentally the centrality selection is typically done with event activity measures in various rapidity ranges. The impact parameter is anti-correlated with charged multiplicity at mid-rapidity, as shown in Fig. 9.1 for UrQMD generated events at $\sqrt{s_{NN}} = 14.5$ GeV, but there is some spread in multiplicity values for a fixed impact parameter. These different methods of selecting centrality may introduce some bias, so for these comparisons the final state charged multiplicity in $|\eta| < 0.5$ was used to select centrality in the models so as to be consistent with the experiment. The models that appear in this chapter are HIJING, AMPT, and UrQMD. They are run with their default parameter values.

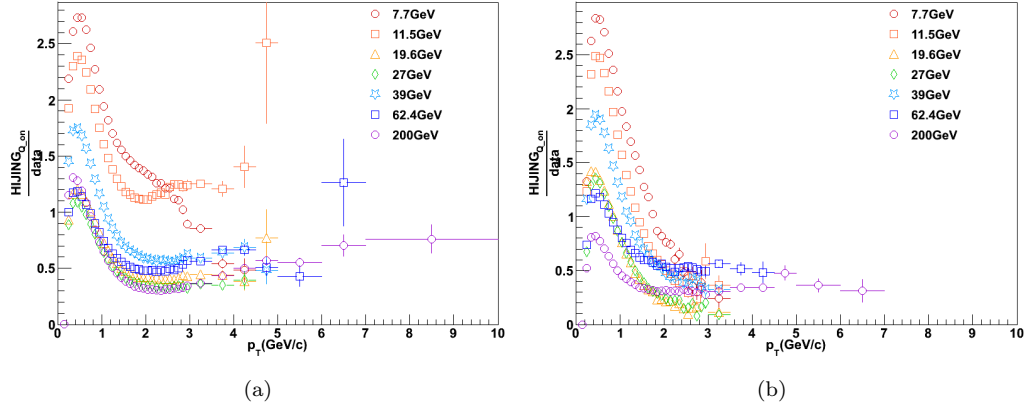


FIGURE 9.3 Ratios of charged hadron p_T spectra from HIJING to those from data for 0-5% central (a) and 60-80% peripheral collisions (b) for $\sqrt{s_{\text{NN}}} = 7.7, 11.5, 19.6, 27, 39, 62.4,$ and 200 GeV.

9.1 HIJING

Each model has different versions as they are improved and tuned to new data. The Heavy Ion Jet Interaction Generator (HIJING) version 1.383 [92] starts from a Glauber Monte Carlo with impact parameter dependent shadowing and merges multi-string phenomenology at low p_T with minijet production for $p_T > 2$ GeV/c [93]. Minijets are produced using the same methods as the PYTHIA $p+p$ event generator with initial and final state radiation. Minijet¹ partonic energy loss is then modeled using the string geometry to get an in-medium path-length. This path-length is multiplied by a fixed estimate of the in-medium energy-loss per unit length, $dE/dl = 1$ GeV/c/fm for a quark jet and 2 GeV/c/fm for a gluon jet, to determine the total energy lost by the minijet to the medium. Energy and momentum are conserved in this model by transferring them to the strings closest to the minijets' trajectories. There is no explicit partonic or hadronic phase in this model and so it would not be expected to reproduce bulk signatures at low- p_T . It does include a “ p_T kick” modification for quarks and diquarks at string end points which models p_T broadening at low p_T .

¹Minijets are moderate p_T scattering processes described by pQCD.

Figure 9.2 shows the charged hadron R_{CP} for 0-5%/60-80% centralities generated by HIJING in $|\eta| < 0.5$ for $\sqrt{s_{NN}} = 7.7, 11.5, 19.6, 27, 39, 62.4,$ and 200 GeV. As in data, there is a strong $\sqrt{s_{NN}}$ dependence to the amount of enhancement or suppression observed at high p_T . However, the ratios of the p_T spectra from data to those from HIJING, shown in Fig. 9.3, reveal that the p_T dependence of the spectra are not well described. Still, this relatively simple model does a remarkably good job of qualitatively describing the particle production over a large range of p_T and $\sqrt{s_{NN}}$. Its simplicity means that it does not require many computational resources, making this an excellent model for simulating detector response.

9.2 AMPT

A Multi-Phase Transport (AMPT) model [94] has two major versions for modeling the partonic phase and hadronization. The default version 1.21 and string melting version 2.21 both start with HIJING initial conditions and use Zhang's Parton Cascade (ZPC) for modeling partonic scatterings, although the default version only runs the minijet partons through ZPC before recombining them with their parent strings. The default version of AMPT then uses the same LUND string fragmentation model for hadronization as HIJING used, but with differently tuned parameters. The string melting version of the model first breaks up the strings into partons, runs these with the partons from minijets through ZPC, and then uses a basic coalescence model for hadronization. Then both versions of the model use A Relativistic Transport model for hadronic scatterings. AMPT is tuned to Pb+Pb data at $\sqrt{s_{NN}} = 17.3$ GeV. p_T spectra from $p+p$ collisions are well described at low p_T by AMPT, as are rapidity densities for a variety of collision systems [94]. AMPT with string melting on is designed to describe the physics of the bulk and so it does well at describing two-particle correlations [94].

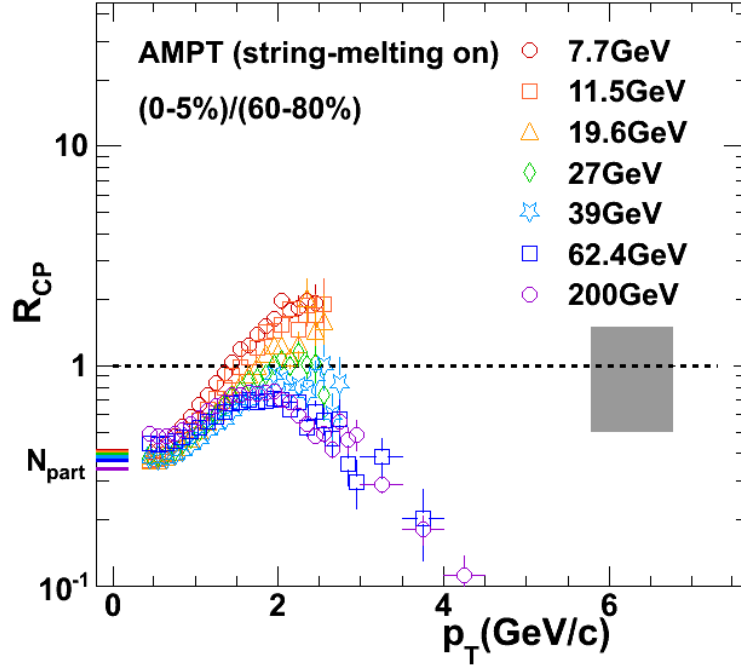


FIGURE 9.4 AMPT generated charged hadron R_{CP} in $|\eta| < 0.5$ for $\sqrt{s_{NN}} = 7.7, 11.5, 19.6, 27, 39, 62.4,$ and 200 GeV for 0-5% over 60-80% centrality bins are shown from the string melting version of the model.

The power of transport models is that they can describe pre-equilibrium and near equilibrium systems that do not satisfy the equilibrium assumptions required for hydrodynamic and thermal models [94].

9.2.1 String-Melting On

The coalescence version of the model might not be expected to accurately describe the high- p_T charged hadron spectra where fragmentation should be the dominant hadronization process. In fact using the default parameters results in a $\sqrt{s_{NN}}$ dependence for R_{CP} , shown in Fig. 9.4, that is similar to what was measured in data. However the ratios of the spectra from the model to the data shown in Fig. 9.5 reveal that the string melting version of the model with default parameters underpredicts the data at $p_T = 3$ GeV/c by an order of magnitude.

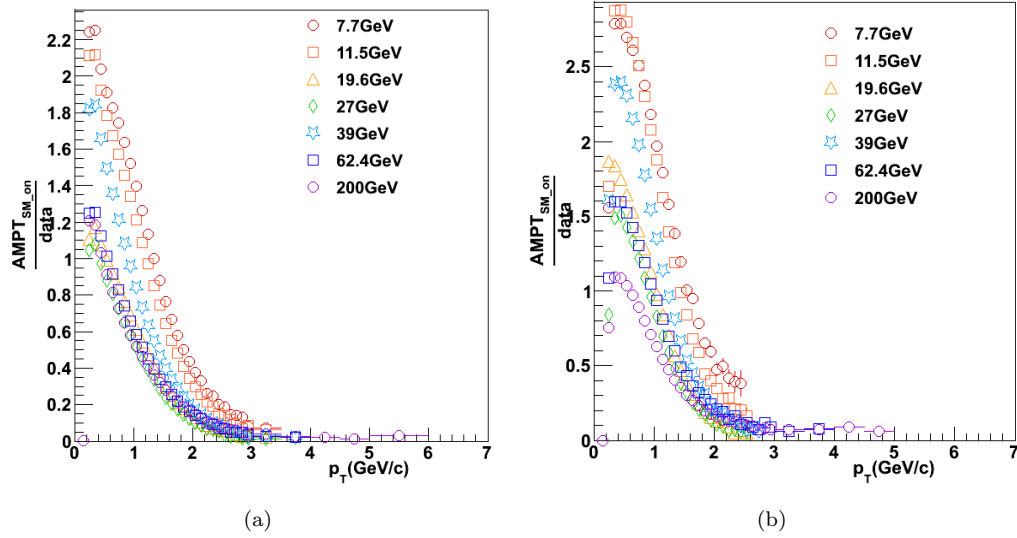


FIGURE 9.5 Ratios of charged hadron p_T spectra from the string melting version of AMPT to those from data for 0-5% central (a) and 60-80% peripheral collisions (b) for $\sqrt{s_{NN}} = 7.7, 11.5, 19.6, 27, 39, 62.4,$ and 200 GeV.

9.2.2 String-Melting Off

The default version of the model would be expected to do a better job of describing the high- p_T kinematics of heavy-ion collisions where fragmentation should dominate the hadronization processes. Instead Fig. 9.6 displays minimal $\sqrt{s_{NN}}$ dependence for high- p_T R_{CP} . The ratios of the spectra from the model to the data are shown in Fig. 9.7. The spectra are closer to the data than for the string melting version of the model, but still underpredict the data. This may be due, in part, to the different Lund spitting function parameters used in the default version of AMPT from those used in HIJING and PYTHIA.

To estimate the effect of running with AMPT Lund spitting function parameters rather than those used in HIJING, HIJING was run with both set of values. The ratios of the central and peripheral spectra with default parameters to those with AMPT's parameters are shown in Fig. 9.8. Clearly, AMPT's values for these parameters reduce its high- p_T yields and shifts it further from the data.

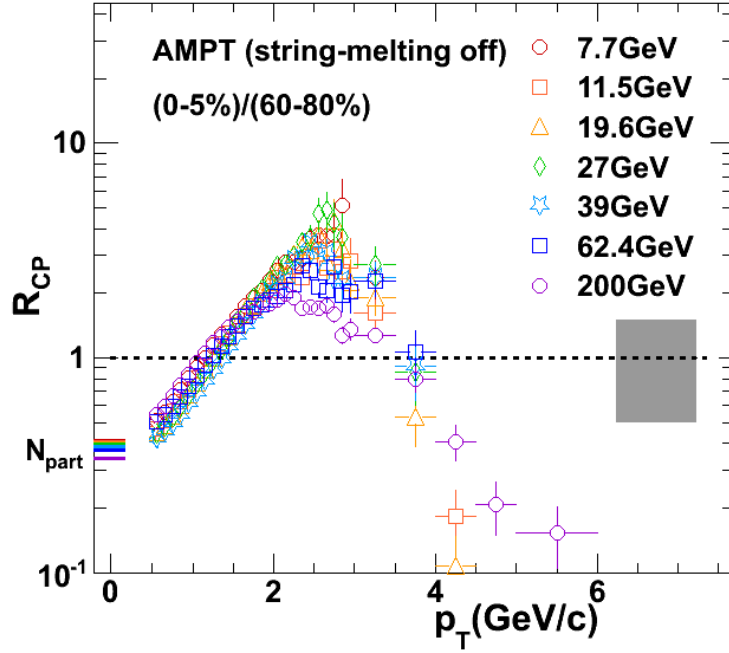


FIGURE 9.6 AMPT generated charged hadron R_{CP} in $|\eta| < 0.5$ for $\sqrt{s_{NN}} = 7.7, 11.5, 19.6, 27, 39, 62.4,$ and 200 GeV for 0-5% over 60-80% centrality bins are shown from the default version of the model.

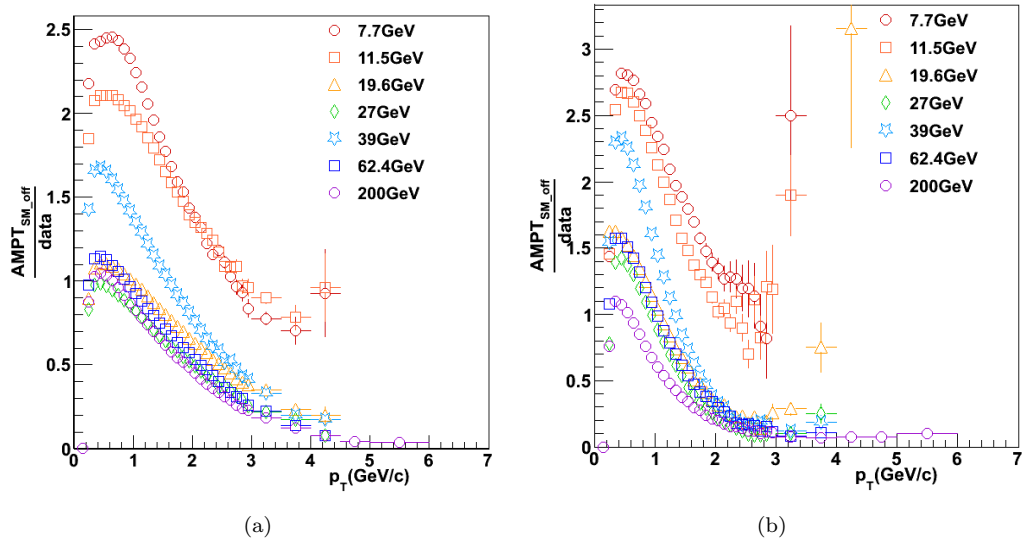


FIGURE 9.7 Ratios of charged hadron p_T spectra from the default version of AMPT to those from data for 0-5% central (a) and 60-80% peripheral collisions (b) for $\sqrt{s_{NN}} = 7.7, 11.5, 19.6, 27, 39, 62.4,$ and 200 GeV.

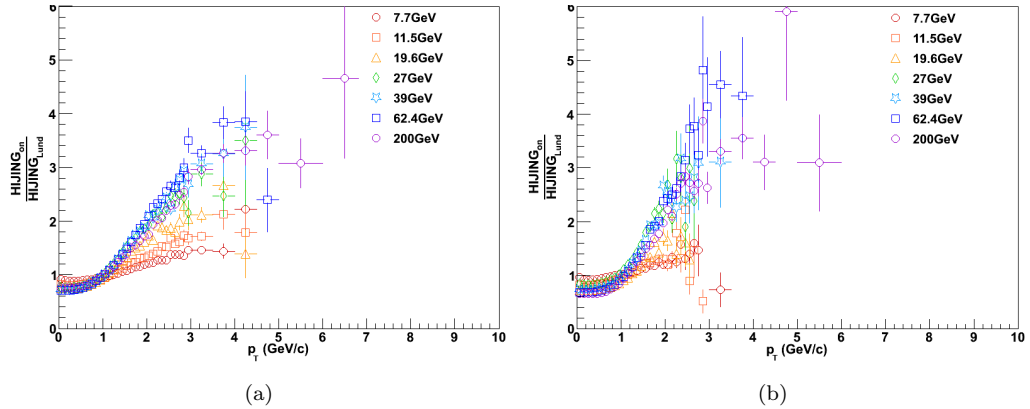


FIGURE 9.8 Ratios of charged hadron p_T spectra from the default version of HIJING to those from HIJING with AMPT's LUND splitting function parameter values for 0-5% central (a) and 60-80% peripheral collisions (b) for $\sqrt{s_{NN}} = 7.7, 11.5, 19.6, 27, 39, 62.4,$ and 200 GeV.

9.3 UrQMD

While the other models use more rudimentary descriptions of the nucleus using relatively simple Glauber Monte Carlos, Ultra-relativistic Quantum Molecular Dynamics (UrQMD) [84, 95] uses a somewhat more precise construction that more closely describes the nucleus in its ground state and carefully takes Pauli-blocking into account in order to avoid unrealistically high local phase space densities for a nucleus near its ground state.

UrQMD is a hadronic transport model which produces hadrons from string decays and resonance decays and uses tabulated and parameterized experimental cross sections to describe the hadronic phase [84, 95]. This model would be expected to do best at describing low- $\sqrt{s_{NN}}$ events that are dominated by the hadronic phase. This model does not require thermal equilibrium and instead describes collectivity dynamically through multiple hadronic scatterings.

Figure 9.9 shows the $\sqrt{s_{NN}}$ dependence of charged hadron R_{CP} from UrQMD. The model predicts minimal $\sqrt{s_{NN}}$ dependence and does not predict the high- p_T enhancement observed at low $\sqrt{s_{NN}}$ in data. The ratios of the p_T -spectra from central and peripheral

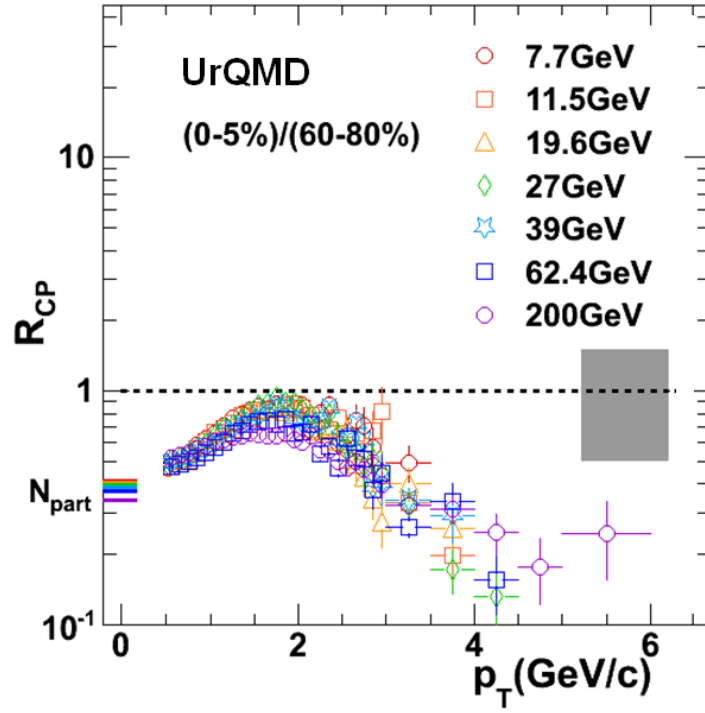


FIGURE 9.9 UrQMD generated charged hadron R_{CP} in $|\eta| < 0.5$ for $\sqrt{s_{NN}} = 7.7, 11.5, 19.6, 27, 39, 62.4,$ and 200 GeV for 0-5% over 60-80% centrality bins are shown from the default version of the model.

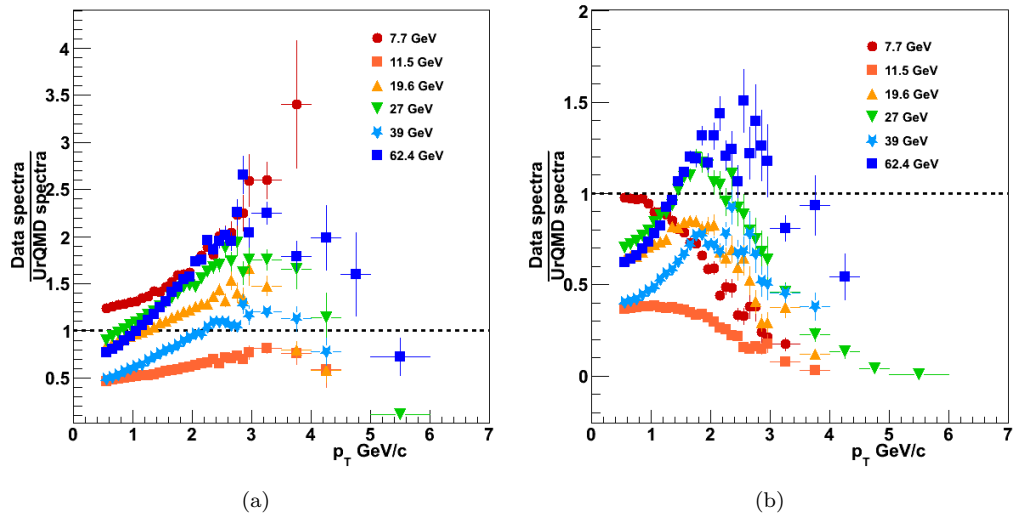


FIGURE 9.10 Ratios of charged hadron p_T spectra from data to those from UrQMD are shown for 0-5% central (a) and 60-80% peripheral collisions (b) for $\sqrt{s_{NN}} = 7.7, 11.5, 19.6, 27, 39, 62.4$ GeV.

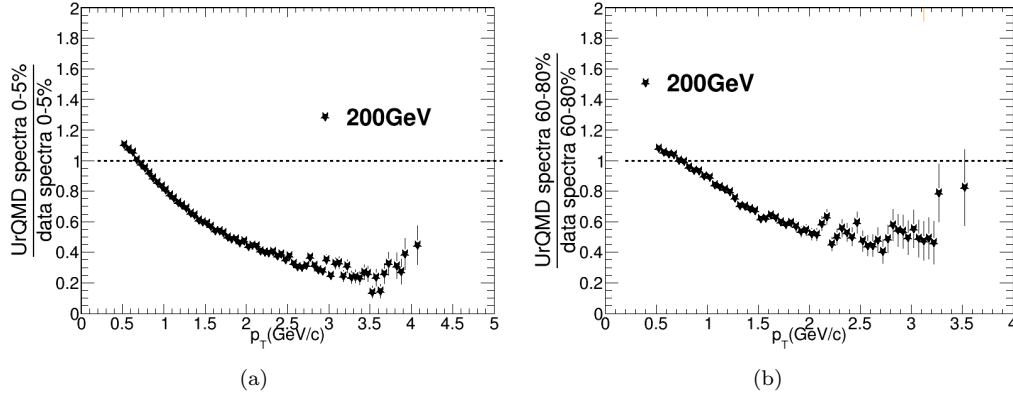


FIGURE 9.11 Ratios of charged hadron p_T spectra from UrQMD to those from data are shown for 0-5% central (a) and 60-80% peripheral collisions (b) for $\sqrt{s_{NN}} = 200$ GeV using an alternative centrality selection procedure.

real events to those generated by UrQMD are shown in Fig. 9.10. The ratios are above unity for some $\sqrt{s_{NN}}$ and below unity for others and these trends are not preserved for the two centrality bins examined here. The ratios increase as a function of p_T for low- p_T central spectra, but some of the ratios turn over and decrease at higher p_T . Peripheral spectra exhibit more complex trends. The deviation between the model and the data is generally not monotonic with either p_T or $\sqrt{s_{NN}}$. Some of the deviation for the peripheral spectra may arise from the sharp cut-off imposed by the model for impact parameters greater than 16 fm, as seen in Fig. 9.1.

In order to partially correct for this centrality bias, the *Mult* cuts for the various centrality bins were adjusted to ensure that the mean impact parameters within the centrality bins matched the mean impact parameters for the various centrality bins from STAR's Glauber Monte Carlo calculations. This procedure was carried out for $\sqrt{s_{NN}} = 200$ GeV with the results shown in Fig. 9.11. UrQMD, like the other models, underpredicts the spectra from data for this energy and these centralities. The deviation is similar for both centralities so that the ratio of charged hadron R_{CP} from UrQMD to that from data is close to unity, as shown in Fig. 9.12.

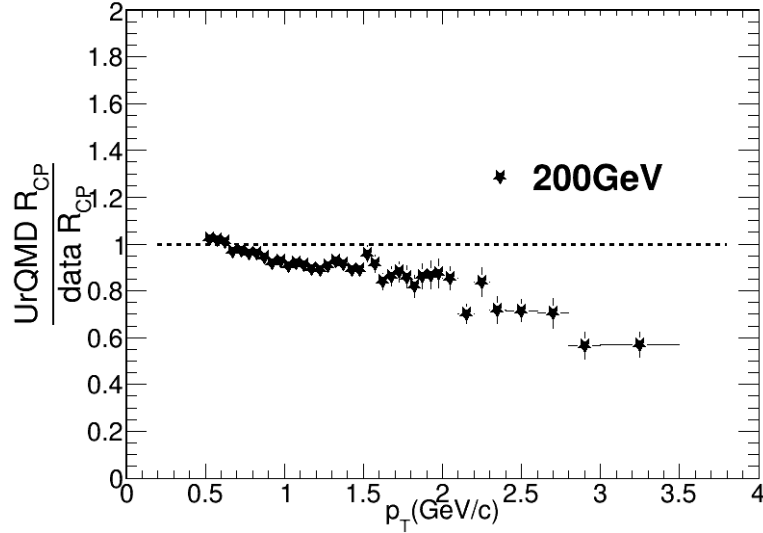


FIGURE 9.12 The ratio of UrQMD generated charged hadron R_{CP} to that from data in $|\eta| < 0.5$ for $\sqrt{s_{NN}} = 200$ GeV for 0-5% over 60-80% centrality bins are shown.

9.4 Summary

Each model discussed in this chapter was designed to reproduce the results of heavy-ion collisions. While each can reproduce many physics results they all fail to reproduce centrality dependent p_T -spectra over a broad range of p_T and $\sqrt{s_{NN}}$ using their default parameter settings. They generally underpredict the spectra at high- p_T . The magnitude of this discrepancy is concealed when the ratios of spectra from different centralities are taken for R_{CP} predictions. HIJING and AMPT with string melting on both exhibit a strong $\sqrt{s_{NN}}$ dependence to the enhancement of high- p_T charged hadron R_{CP} that qualitatively agrees with the data. However, HIJING over predicts the enhancement of high- p_T charged hadrons at low $\sqrt{s_{NN}}$ and underpredicts the suppression at high $\sqrt{s_{NN}}$. AMPT, on the other hand, underpredicts the enhancement at low $\sqrt{s_{NN}}$. AMPT with string melting off and UrQMD fail to qualitatively describe the $\sqrt{s_{NN}}$ dependence of charged hadron R_{CP} at high p_T .

Chapter 10

Conclusions and Outlook

The first purpose of this dissertation is to test the prediction that high- p_T suppression of charged hadron R_{CP} should “turn off” at sufficiently low $\sqrt{s_{NN}}$ if it is really a signature of QGP formation. The second purpose is to set a limit from high- p_T charged hadrons for the minimum $\sqrt{s_{NN}}$ needed to form a QGP. Although high- p_T R_{CP} is below unity for $\sqrt{s_{NN}} = 39$ GeV, only high- p_T charged hadrons at $\sqrt{s_{NN}} = 62.4$ GeV are suppressed when scaling uncertainties are accounted for. In carrying out this dissertation research it was determined that large enhancement effects are competing with the suppression effect that we want to measure, i.e. partonic energy-loss in a QGP. In order to advance this research beyond the measurement of net suppression of high- p_T charged hadrons in N_{bin} -scaled central collisions relative to peripheral collisions, new methods and observables are developed.

One method is to measure suppression relative to models that include the various enhancement effects. However these models are found to need more development and fine-tuning to provide the level of precision needed for this comparison.

Another method to improve the sensitivity to QGP is to use hadrons that are less sensitive to enhancement effects. Because protons have been found to be more affected by enhancement effects than pions, using high- p_T pions as probes for suppression improves

sensitivity to partonic energy-loss. Particle identification becomes increasingly difficult at high p_T though, so an alternative is to only look at negatively charged hadrons. At low $\sqrt{s_{NN}}$, few anti-protons are produced in heavy-ion collisions so that negatively charged hadrons mostly consist of π^- mesons. Negative charged hadron R_{CP} is below inclusive charged hadron R_{CP} for all $\sqrt{s_{NN}}$ in the BES. High- p_T negative charged hadron R_{CP} is below unity for $\sqrt{s_{NN}} \geq 27$ GeV, however it is still the case that only the 62.4 GeV R_{CP} is significantly suppressed.

Because the physical process that we are trying to describe is a shift in p_T rather than the formation or annihilation of hadrons at a particular p_T the fractional energy-loss observable, S_{loss} , is more closely linked to the physics of interest. R_{CP} is sensitive to the shapes of the spectra so that the same shift in p_T will cause a larger change in R_{CP} from steep, low- $\sqrt{s_{NN}}$ data than from less steep, high- $\sqrt{s_{NN}}$ data. Surprisingly, the enhancement in $\sqrt{s_{NN}} = 7.7$ GeV R_{CP} is driven by a shift of p_T for central spectra relative to peripheral spectra that is even larger than the shift from higher $\sqrt{s_{NN}}$. The possibility that this is solely caused by particle ratios and larger enhancement of protons than pions is once again ruled out by measuring S_{loss} for negative charged hadrons, although larger enhancement of protons did contribute significantly. Two possible explanations for the remaining larger p_T enhancement of negative charged hadrons in $\sqrt{s_{NN}} = 7.7$ GeV data are presented here. One possibility is that there is only more *net* enhancement at $\sqrt{s_{NN}} = 7.7$ GeV. If the combined enhancement effects provide the same or less p_T boost to hadrons in central $\sqrt{s_{NN}} = 7.7$ GeV collisions than they do in 11.5 GeV collisions then this difference must be driven by larger energy-loss at $\sqrt{s_{NN}} = 11.5$ GeV. This would be evidence for QGP formation at 11.5 GeV. The other possibility is that the difference is driven by the fraction of hadrons originating from coalescence versus fragmentation. The steeper spectra at $\sqrt{s_{NN}} = 7.7$ GeV reduces the number of high- p_T partons that can produce hadrons for a particular intermediate to high- p_T bin. If a QGP is formed, however, then coalescing low- p_T partons can produce intermediate to high- p_T hadrons. Going from $\sqrt{s_{NN}} = 11.5$ GeV to 7.7 GeV, a larger fraction of the hadrons at a given p_T would originate from coalescence. Enhancement effects on each parton would contribute

to the p_T shift of the final hadron leading to larger p_T shifts for hadrons in the $\sqrt{s_{NN}} = 7.7$ GeV central collisions than in 11.5 GeV collisions. If this is the correct interpretation of these results then it provides evidence for QGP formation in $\sqrt{s_{NN}} = 7.7$ GeV central Au+Au collisions.

A new method for disentangling enhancement and suppression effects is developed in this dissertation. That is to measure the N_{part} dependence of N_{bin} -scaled high- p_T yields. Because enhancement and suppression effects can have different centrality dependence it is possible to measure the net modification of the most central data relative to a centrality bin that already includes enhancement effects. Both $Y(N_{\text{part}})$ and a nuclear modification factor using 10-20% central spectra as the reference provide evidence from high- p_T charged hadrons of QGP formation in 0-5% central, $\sqrt{s_{NN}} = 14.5$ GeV collisions.

Taken together, these measurements provide strong evidence for QGP formation down to $\sqrt{s_{NN}} = 14.5$ GeV. There is also one measurement that is consistent with QGP formation in 0-5% central Au+Au collisions at $\sqrt{s_{NN}} = 11.5$ GeV.

$\sqrt{s_{NN}} = 19.6$ GeV d +Au events collected in 2016 provide a reference for cold nuclear matter effects at a moderate BES collision energy. Making spectra from these events, as well as the Au+Au spectra in this thesis, available will provide important constraints for models.

Triggered dihadron correlations would provide a complimentary high- p_T partonic energy-loss signature. Such a measurement may require more statistics than are currently available for the lower energies in the BES in order to separate the hard component from the background. This is suggested by Fig. 10.1 where the nearside, $\Delta\eta=0$ and $\Delta\phi=0$, jet structure that is prominent at $\sqrt{s_{NN}} = 200$ GeV vanishes with current statistics at $\sqrt{s_{NN}} = 39$ GeV. γ -hadron, γ -jet, jet-hadron, or hadron-jet correlations would provide alternative means of studying particles produced in hard scatterings at BES energies.

The measurements in this dissertation may be improved with the extended p_T reach from the higher statistics in BES II, the second phase of the RHIC BES that is scheduled to

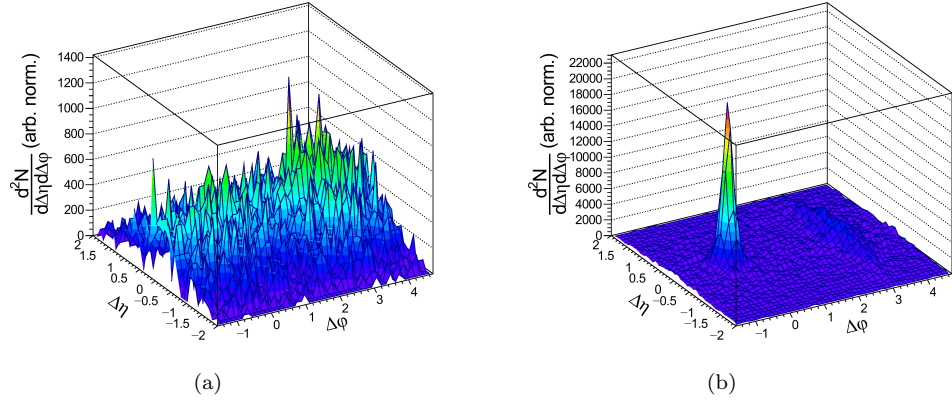


FIGURE 10.1 Dihadron correlations from $\sqrt{s_{\text{NN}}} = 39$ (a) and 200 GeV (b) for $3 < p_{\text{T}}^{\text{trigger}} < 10$ GeV/c and $1.5 < p_{\text{T}}^{\text{associated}} < 3$ GeV/c. These 2D correlations are not corrected for tracking efficiency and acceptance.

take data in 2019-2020. STAR has extended the RHIC kinematics by installing a fixed target which extends the lower limit of the heavy ion collision energy accessible at STAR below $\sqrt{s_{\text{NN}}} = 3.9$ GeV [96]. Data at these lower energies will also be collected during BES II. Au+Au collisions at this low of $\sqrt{s_{\text{NN}}}$ should not produce a QGP. Thus, they will serve as a reference for many of the bulk measurements as well as the observables discussed in this thesis.

Appendix A

Glauber Monte Carlo Results

The STAR Glauber Monte Carlo (Glauber MC) describes the nuclear charge density with a three parameter Fermi distribution,

$$\frac{\rho(r)}{\rho_0} = \frac{1 + w(r/R)^2}{1 + \exp(\frac{r-R}{a})}, \quad (\text{A.1})$$

where w is set to zero for gold since gold is nearly spherical, R is the nuclear radius and is set to 6.38 fm for gold, and a is the skin depth which is set to 0.535. The minimum separation between nucleons in the same nucleus is set to zero as using more physical limitations have not been found to significantly effect the final Monte Carlo results. The effective sizes of the nucleons are obtained from their inelastic nucleon-nucleon cross sections which depend on $\sqrt{s_{\text{NN}}}$ and the values used by STAR are reported in Table A.1. Two gold nuclei are constructed with a particular impact parameter, b , and the total number of participating nucleons, N_{part} , and the number of nucleon-nucleon binary collisions, N_{bin} , are counted. Doing this many times for random b values provides a distribution of N_{part} and N_{bin} values.

The charged particle multiplicity distribution in $|\eta| < 0.5$ is measured from the data and the multiplicity dependent efficiency corrected for. Charged particle production is

$\sqrt{s_{\text{NN}}}$ (GeV)	σ_{NN} (mb)
7.7	30.8
11.5	31.2
14.5	31.5
19.6	32
27	33
39	34
62.4	36
200	42

TABLE A.1 Nucleon-nucleon inelastic cross sections for each $\sqrt{s_{\text{NN}}}$.

$\sqrt{s_{\text{NN}}}$ (GeV)	n_{pp}	x	k
7.7	0.89	0.12	2
11.5	1.07	0.12	2
14.5	1.172	0.12	2
19.6	1.29	0.12	1.8
27	1.385	0.12	1.65
39	1.52	0.12	1.5
62.4	1.60	0.12	2
200	2.43	0.13	2

TABLE A.2 Negative binomial distribution parameter values.

estimated as

$$\frac{dN}{d\eta} = (1 - x)n_{pp} \frac{N_{\text{part}}}{2} + xn_{pp}N_{\text{bin}}, \quad (\text{A.2})$$

where n_{pp} is the multiplicity from a $p+p$ collision and x is the fraction of particle production driven by processes which are proportionate to N_{bin} . Then a negative binomial distribution with a k parameter can be fit to the data to match $\langle N_{\text{bin}} \rangle$ and $\langle N_{\text{part}} \rangle$ values to centrality classes that are defined by cuts on charged multiplicity. The resulting parameters for the negative binomial distributions are shown in Table A.2. The $\langle N_{\text{bin}} \rangle$ and $\langle N_{\text{part}} \rangle$ values are reported in Tables A.3 and A.4 respectively¹.

¹It was frequently advised throughout my education that Wikipedia should be the first place you look and the last place you cite. In gratitude for the important role the site has played in my education (including the preparation of this thesis) and the many people who contribute to this repository of human knowledge, I take that advice literally here [97].

Centrality	7.7 GeV	11.5 GeV	14.5 GeV	19.6 GeV
0-5%	774±28	784±27	788±30	800±27
5-10%	629±20	635±20	634±20	643±20
10-20%	450±22	453±23	454±24	458±24
20-40%	225±24	228±23	224±24	228±24
40-60%	74±16	75±16	72±15	74±15
60-80%	19.2±6.3	19.1±7.8	18.3±6.3	18.9±6.9
Centrality	27 GeV	39 GeV	62.4 GeV	200 GeV
0-5%	841±28	853±27	904±27	1048±27
5-10%	694±22	687±21	727±21	838±23
10-20%	497±26	492±26	519±25	594±30
20-40%	249±27	244±26	258±27	291±30
40-60%	82±18	79±17	82±18	91±20
60-80%	20.0±8.6	19.4±7.7	19.3±7.7	21.6±8.0

TABLE A.3 $\langle N_{\text{bin}} \rangle$ for each energy and centrality used in these analyses.

Centrality	7.7 GeV	11.5 GeV	14.5 GeV	19.6 GeV
0-5%	337.4±2.1	338.2±2.0	337.9±2.3	338.0±2.3
5-10%	290.4±6.0	290.6±6.2	289.1±6.5	289.2±6.0
10-20%	226.2±7.9	226.0±8.2	225.6±8.5	224.9±8.6
20-40%	134±11	135±10	132±10	133±10
40-60%	58.4±9.8	58.5±9.4	56.8±9.1	57.7±9.1
60-80%	20.2±5.3	20.1±6.7	19.5±5.4	19.9±5.9
Centrality	27 GeV	39 GeV	62.4 GeV	200 GeV
0-5%	343.3±2.0	341.7±2.2	344.5±2.1	350.6±2.1
5-10%	299.3±6.2	293.9±6.4	296.6±5.9	302.2±6.0
10-20%	233.6±9.0	229.8±8.7	232.2±8.2	237.3±8.5
20-40%	140±11	137±10.7	139±10	143±11
40-60%	61±10	59.2±9.7	60.4±9.8	62±10
60-80%	20.5±7.1	20.0±6.4	19.8±6.3	21.0±6.1

TABLE A.4 $\langle N_{\text{part}} \rangle$ for each energy and centrality used in these analyses.

Glossary

AMPT A Monte Carlo event generator with transport models of the partonic and hadronic phases. ix, 90, 92–96, 99

BES Phase one of the RHIC beam energy scan. vii, viii, 14, 30, 49, 59, 66, 82, 84, 86, 101–103

BRAHMS The Broad RAnge Hadron Magnetic Spectrometers PHOBOS refers both to the PHOBOS detector and to the PHOBOS Collaboration. 30

CNM Cold nuclear matter effects are the set of modifications due to there being a nucleus in the collision system and are separate from modification caused by QGP production. 23, 24

GEANT A simulation used to model interactions with detector materials. 46, 49

HIJING A fast Monte Carlo event generator that models the phases of a collision phenomenologically. ix, 90–92, 94, 96, 99

nPDF A nPDF is the same as a PDF, but for nucleons bound in nuclei. 3, 20

PDF A parton distribution function describes the probability that a parton will carry a particular momentum fraction, x , of a unbound nucleon. v, 3–5

PHENIX The Pioneering High Energy Nuclear Interaction eXperiment, PHENIX, refers both to the PHENIX detector and to the PHENIX Collaboration. v, 8, 20, 27, 30

PHOBOS PHOBOS refers both to the PHOBOS detector and to the PHOBOS Collaboration. 30

QGP Quark gluon plasma is a de-confined state with partonic degrees of freedom. v, 2, 3, 5–11, 13, 14, 17, 20, 23, 84, 100–103

RHIC The Relativistic Heavy Ion Collider, RHIC, at BNL is one of two heavy-ion colliders currently in operation. v, vi, 2, 9, 14–16, 28–30, 33, 34, 36, 66, 84, 102, 103

STAR The Solenoidal Tracker At RHIC, STAR, is a TPC-based detector operated by the STAR Collaboration. v, vi, 7, 8, 16, 17, 19, 21, 22, 30–34, 36, 43, 46, 49, 61, 98, 103, 104

TPC The time projection chamber provides the tracking for STAR as well as low- p_T charged particle identification. vi, 30–35, 37, 38, 40–42, 49, 54, 61

UrQMD A Monte Carlo event generator with no partonic phase. ix, 46, 47, 62, 89, 90, 96–99

Bibliography

- [1] Alexander M. Polyakov. Compact Gauge Fields and the Infrared Catastrophe. *Phys. Lett.*, B59:82–84, 1975. doi: 10.1016/0370-2693(75)90162-8.
- [2] Henrik Bohr and H.B. Nielsen. *Nuclear Physics B*, 128(2):275 – 293, 1977.
- [3] James M. Lattimer and Madappa Prakash. What a Two Solar Mass Neutron Star Really Means. In Sabine Lee, editor, *From Nuclei to Stars: Festschrift in Honor of Gerald E Brown*, pages 275–304. 2011. doi: 10.1142/9789814329880_0012. URL <https://inspirehep.net/record/881493/files/arXiv:1012.3208.pdf>.
- [4] Mark G. Alford, Andreas Schmitt, Krishna Rajagopal, and Thomas Schfer. Color superconductivity in dense quark matter. *Rev. Mod. Phys.*, 80:1455–1515, 2008. doi: 10.1103/RevModPhys.80.1455.
- [5] Shusu Shi. *Event anisotropy v_2 at STAR*. PhD thesis, Hua-Zhong Normal U., 2010. URL <http://drupal.star.bnl.gov/STAR/theses/phd/shusushi>.
- [6] Sayipjamal Dulat, Tie-Jiun Hou, Jun Gao, Marco Guzzi, Joey Huston, Pavel Naldsky, Jon Pumplin, Carl Schmidt, Daniel Stump, and C.-P. Yuan. New parton distribution functions from a global analysis of quantum chromodynamics. *Phys. Rev. D*, 93:033006, Feb 2016. doi: 10.1103/PhysRevD.93.033006. URL <http://link.aps.org/doi/10.1103/PhysRevD.93.033006>.
- [7] Hannu Paukkunen. Nuclear PDFs in the beginning of the LHC era. *Nucl. Phys.*, A926:24–33, 2014. doi: 10.1016/j.nuclphysa.2014.04.001.

-
- [8] Ilkka Helenius. *Spatially dependent parton distribution functions and hard processes in nuclear collisions*. PhD thesis, Jyväskylä U., 2014. URL <https://inspirehep.net/record/1312775/files/arXiv:1408.6660.pdf>.
- [9] Ilkka Helenius, Kari J. Eskola, Heli Honkanen, and Carlos A. Salgado. Impact-Parameter Dependent Nuclear Parton Distribution Functions: EPS09s and EKS98s and Their Applications in Nuclear Hard Processes. *JHEP*, 07:073, 2012. doi: 10.1007/JHEP07(2012)073.
- [10] Stanley J. Brodsky and Hung Jung Lu. Shadowing and Antishadowing of Nuclear Structure Functions. *Phys. Rev. Lett.*, 64:1342, 1990. doi: 10.1103/PhysRevLett.64.1342.
- [11] Xurong Chen, Jianhong Ruan, Rong Wang, Pengming Zhang, and Wei Zhu. Applications of a nonlinear evolution equation II: the EMC effect. *Int. J. Mod. Phys.*, E23(10):1450058, 2014. doi: 10.1142/S021830131450058X.
- [12] Michele Arneodo. Nuclear effects in structure functions. *Physics Reports*, 240(5):301 – 393, 1994. ISSN 0370-1573. doi: [http://dx.doi.org/10.1016/0370-1573\(94\)90048-5](http://dx.doi.org/10.1016/0370-1573(94)90048-5). URL <http://www.sciencedirect.com/science/article/pii/0370157394900485>.
- [13] Steffen A. Bass. Microscopic reaction dynamics at SPS and RHIC. *Nucl. Phys.*, A698:164–170, 2002. doi: 10.1016/S0375-9474(01)01360-4.
- [14] T. Matsui and H. Satz. J/ψ suppression by quark-gluon plasma formation. *Physics Letters B*, 178(4):416 – 422, 1986. ISSN 0370-2693. doi: [http://dx.doi.org/10.1016/0370-2693\(86\)91404-8](http://dx.doi.org/10.1016/0370-2693(86)91404-8). URL <http://www.sciencedirect.com/science/article/pii/0370269386914048>.
- [15] L. Adamczyk et al. Energy dependence of J/ψ production in Au+Au collisions at $\sqrt{s_{NN}} = 39, 62.4$ and 200 GeV. 2016.

- [16] Bjoern Schenke, Prithwish Tribedy, and Raju Venugopalan. Fluctuating Glasma initial conditions and flow in heavy ion collisions. *Phys. Rev. Lett.*, 108:252301, 2012. doi: 10.1103/PhysRevLett.108.252301.
- [17] Mohammad Naghdi. Nucleon-nucleon interaction: A typical/concise review. *Phys. Part. Nucl.*, 45:924–971, 2014. doi: 10.1134/S1063779614050050.
- [18] Peter Brockway Arnold, Guy D. Moore, and Laurence G. Yaffe. Effective kinetic theory for high temperature gauge theories. *JHEP*, 01:030, 2003. doi: 10.1088/1126-6708/2003/01/030.
- [19] Francois Gelis, Edmond Iancu, Jamal Jalilian-Marian, and Raju Venugopalan. The Color Glass Condensate. *Ann. Rev. Nucl. Part. Sci.*, 60:463–489, 2010. doi: 10.1146/annurev.nucl.010909.083629.
- [20] Bjoern Schenke, Prithwish Tribedy, and Raju Venugopalan. Event-by-event gluon multiplicity, energy density, and eccentricities in ultrarelativistic heavy-ion collisions. *Phys. Rev.*, C86:034908, 2012. doi: 10.1103/PhysRevC.86.034908.
- [21] Derek A. Teaney. Viscous Hydrodynamics and the Quark Gluon Plasma. In Rudolph C. Hwa and Xin-Nian Wang, editors, *Quark-gluon plasma 4*, pages 207–266. 2010. doi: 10.1142/9789814293297_0004. URL <https://inspirehep.net/record/820552/files/arXiv:0905.2433.pdf>.
- [22] Szabolcs Borsanyi et al. *JHEP*, 09:073, 2010.
- [23] Jacquelyn Noronha-Hostler, Barbara Betz, Jorge Noronha, and Miklos Gyulassy. Event-by-event hydrodynamics + jet energy loss: A solution to the $R_{AA} \otimes v_2$ puzzle. *Phys. Rev. Lett.*, 116(25):252301, 2016. doi: 10.1103/PhysRevLett.116.252301.
- [24] Hannah Petersen, Jan Steinheimer, Jussi Auvinen, and Marcus Bleicher. The beam energy dependence of collective flow in heavy ion collisions. *PoS*, CPOD2014:024, 2015.

-
- [25] L. Adamczyk et al. Beam-energy-dependent two-pion interferometry and the freeze-out eccentricity of pions measured in heavy ion collisions at the STAR detector. *Phys. Rev.*, C92(1):014904, 2015. doi: 10.1103/PhysRevC.92.014904.
- [26] L. Adamczyk et al. Harmonic decomposition of three-particle azimuthal correlations at RHIC. 2017.
- [27] L. Adamczyk et al. Measurement of elliptic flow of light nuclei at $\sqrt{s_{NN}} = 200, 62.4, 39, 27, 19.6, 11.5,$ and 7.7 GeV at the BNL Relativistic Heavy Ion Collider. *Phys. Rev.*, C94(3):034908, 2016. doi: 10.1103/PhysRevC.94.034908.
- [28] L. Adamczyk et al. Beam Energy Dependence of the Third Harmonic of Azimuthal Correlations in Au+Au Collisions at RHIC. *Phys. Rev. Lett.*, 116(11):112302, 2016. doi: 10.1103/PhysRevLett.116.112302.
- [29] L. Adamczyk et al. Centrality dependence of identified particle elliptic flow in relativistic heavy ion collisions at $\sqrt{s_{NN}}=7.762.4$ GeV. *Phys. Rev.*, C93(1):014907, 2016. doi: 10.1103/PhysRevC.93.014907.
- [30] L. Adamczyk et al. Observation of charge asymmetry dependence of pion elliptic flow and the possible chiral magnetic wave in heavy-ion collisions. *Phys. Rev. Lett.*, 114(25):252302, 2015. doi: 10.1103/PhysRevLett.114.252302.
- [31] N. M. Abdelwahab et al. Isolation of Flow and Nonflow Correlations by Two- and Four-Particle Cumulant Measurements of Azimuthal Harmonics in $\sqrt{s_{NN}} = 200$ GeV Au+Au Collisions. *Phys. Lett.*, B745:40–47, 2015. doi: 10.1016/j.physletb.2015.04.033.
- [32] L. Adamczyk et al. Beam-energy dependence of charge separation along the magnetic field in Au+Au collisions at RHIC. *Phys. Rev. Lett.*, 113:052302, 2014. doi: 10.1103/PhysRevLett.113.052302.

- [33] Berndt Mller. A New Phase of Matter: Quark-Gluon Plasma Beyond the Hagedorn Critical Temperature. In Johann Rafelski, editor, *Melting Hadrons, Boiling Quarks - From Hagedorn Temperature to Ultra-Relativistic Heavy-Ion Collisions at CERN: With a Tribute to Rolf Hagedorn*, pages 107–116. 2016. doi: 10.1007/978-3-319-17545-4_14. URL <http://inspirehep.net/record/1341063/files/arXiv:1501.06077.pdf>.
- [34] Vincenzo Minissale, Francesco Scardina, and Vincenzo Greco. Hadrons from coalescence plus fragmentation in AA collisions at energies available at the BNL Relativistic Heavy Ion Collider to the CERN Large Hadron Collider. *Phys. Rev.*, C92(5):054904, 2015. doi: 10.1103/PhysRevC.92.054904.
- [35] Md. Nasim, Lokesh Kumar, Pawan Kumar Netrakanti, and Bedangadas Mohanty. Energy dependence of elliptic flow from heavy-ion collision models. *Phys. Rev.*, C82:054908, 2010. doi: 10.1103/PhysRevC.82.054908.
- [36] S. Voloshin and Y. Zhang. Flow study in relativistic nuclear collisions by Fourier expansion of Azimuthal particle distributions. *Z. Phys.*, C70:665–672, 1996. doi: 10.1007/s002880050141.
- [37] B. Alver and G. Roland. Collision geometry fluctuations and triangular flow in heavy-ion collisions. *Phys. Rev.*, C81:054905, 2010. doi: 10.1103/PhysRevC.82.039903,10.1103/PhysRevC.81.054905. [Erratum: *Phys. Rev.*C82,039903(2010)].
- [38] L. Adamczyk et al. Direct virtual photon production in Au+Au collisions at $\sqrt{s_{NN}} = 200$ GeV. 2016.
- [39] Santosh K. Das, Marco Ruggieri, Surasree Mazumder, Vincenzo Greco, and Jan-e Alam. Heavy quark diffusion in the pre-equilibrium stage of heavy ion collisions. *J. Phys.*, G42(9):095108, 2015. doi: 10.1088/0954-3899/42/9/095108.
- [40] Shanshan Cao, Guang-You Qin, and Steffen A. Bass. Energy loss, hadronization and hadronic interactions of heavy flavors in relativistic heavy-ion collisions. *Phys. Rev.*, C92(2):024907, 2015. doi: 10.1103/PhysRevC.92.024907.

- [41] B. G. Zakharov. Nuclear modification factor for light and heavy flavors within pQCD and recent data from the LHC. *JETP Lett.*, 96:616–620, 2013. doi: 10.1134/S002136401222016X.
- [42] Serguei Chatrchyan et al. *Eur.Phys.J.*, C72:1945, 2012.
- [43] J.D. Jackson. Wiley, 1975. ISBN 9780471431329. URL https://books.google.com/books?id=_7rvAAAAMAAJ.
- [44] Michael L. Miller, Klaus Reygers, Stephen J. Sanders, and Peter Steinberg. *Ann.Rev.Nucl.Part.Sci.*, 57:205–243, 2007.
- [45] J. Adams et al. Transverse momentum and collision energy dependence of high p(T) hadron suppression in Au+Au collisions at ultrarelativistic energies. *Phys. Rev. Lett.*, 91:172302, 2003. doi: 10.1103/PhysRevLett.91.172302.
- [46] K. Walsh. Theory provides roadmap in quest for quark soup 'critical point', 2017. URL <https://www.bnl.gov/newsroom/news.php?a=26716>. [Accessed: 2017-01-31].
- [47] Roy A. Lacey. Indications for a Critical End Point in the Phase Diagram for Hot and Dense Nuclear Matter. *Phys. Rev. Lett.*, 114(14):142301, 2015. doi: 10.1103/PhysRevLett.114.142301.
- [48] Roy A. Lacey, Peifeng Liu, Niseem Magdy, B. Schweid, and N. N. Ajitanand. Finite-Size Scaling of Non-Gaussian Fluctuations Near the QCD Critical Point. 2016.
- [49] S. Afanasiev et al. Measurement of Direct Photons in Au+Au Collisions at $\sqrt{s_{NN}} = 200$ GeV. *Phys. Rev. Lett.*, 109:152302, 2012. doi: 10.1103/PhysRevLett.109.152302.
- [50] Guang-You Qin. Anisotropic Flow and Jet Quenching in Relativistic Nuclear Collisions. *Int. J. Mod. Phys.*, E24(02):1530001, 2015. doi: 10.1142/S0218301315300015.
- [51] A. Schmah and B. Jacobs. The mixed event technique for the h-jet analysis in au+au 200 gev, 2016. URL <https://indico.cern.ch/event/566346/contributions/>

- 2288233/attachments/1329727/1997731/aschmah_Jet_ME_08_30_2016_V1.pdf.
[Accessed: 2017-02-21].
- [52] A. A. Bylinkin, N. S. Chernyavskaya, and A. A. Rostovtsev. Two components in charged particle production in heavy-ion collisions. *Nucl. Phys.*, B903:204–210, 2016. doi: 10.1016/j.nuclphysb.2015.12.009.
- [53] J. Adams et al. Identified hadron spectra at large transverse momentum in p+p and d+Au collisions at $s(\text{NN})^{1/2} = 200\text{-GeV}$. *Phys. Lett.*, B637:161–169, 2006. doi: 10.1016/j.physletb.2006.04.032.
- [54] J.W. Cronin, Henry J. Frisch, M.J. Shochet, J.P. Boymond, R. Mermud, et al. *Phys.Rev.*, D **11**:3105, 1975.
- [55] L. Kluberg, P.A. Piroue, Richard L. Sumner, D. Antreasyan, J.W. Cronin, et al. *Phys.Rev.Lett.*, 38:670–673, 1977.
- [56] P.B. Straub, D.E. Jaffe, Henry D. Glass, M.R. Adams, C.N. Brown, et al. *Phys.Rev.Lett.*, **68**:452–455, 1992.
- [57] Alberto Polleri and Feng Yuan. Rapidity dependence of large p(transverse) hadron production at RHIC. 2001.
- [58] A. H. Mueller, Bin Wu, Bo-Wen Xiao, and Feng Yuan. Probing Transverse Momentum Broadening in Heavy Ion Collisions. *Phys. Lett.*, B763:208–212, 2016. doi: 10.1016/j.physletb.2016.10.037.
- [59] A. Adare et al. Evolution of π^0 suppression in Au+Au collisions from $\sqrt{s_{\text{NN}}} = 39$ to 200 GeV. *Phys. Rev. Lett.*, 109:152301, 2012. doi: 10.1103/PhysRevLett.109.152301.
- [60] H. Hahn. THE RHIC PROJECT: OVERVIEW AND STATUS. In *Proceedings, 3rd Workshop on Experiments and Detectors for a Relativistic Heavy Ion Collider: Upton, NY, July 18-22, 1988*, pages 7–28, 1988.

-
- [61] H. Hahn et al. The RHIC design overview. *Nucl. Instrum. Meth.*, A499:245–263, 2003. doi: 10.1016/S0168-9002(02)01938-1.
- [62] Alexandru Jipa. Overview of the results from the BRAHMS experiment. *Acta Phys. Hung.*, A22:121–137, 2005. doi: 10.1556/APH.22.2005.1-2.13.
- [63] K. H. Ackermann et al. STAR detector overview. *Nucl. Instrum. Meth.*, A499:624–632, 2003. doi: 10.1016/S0168-9002(02)01960-5.
- [64] E. J. O’Brien. Overview of the PHENIX experiment. *AIP Conf. Proc.*, 698:745–750, 2004. doi: 10.1063/1.1664343. [,745(2004)].
- [65] B. B. Back et al. The PHOBOS detector at RHIC. *Nucl. Instrum. Meth.*, A499:603–623, 2003. doi: 10.1016/S0168-9002(02)01959-9.
- [66] H. Wieman et al. STAR TPC at RHIC. *IEEE Trans. Nucl. Sci.*, 44:671–678, 1997. doi: 10.1109/23.603731.
- [67] F. Bergsma et al. The STAR detector magnet subsystem. *Nucl. Instrum. Meth.*, A499:633–639, 2003. doi: 10.1016/S0168-9002(02)01961-7.
- [68] M. Anderson et al. The Star time projection chamber: A Unique tool for studying high multiplicity events at RHIC. *Nucl. Instrum. Meth.*, A499:659–678, 2003. doi: 10.1016/S0168-9002(02)01964-2.
- [69] M. Beddo et al. The STAR barrel electromagnetic calorimeter. *Nucl. Instrum. Meth.*, A499:725–739, 2003. doi: 10.1016/S0168-9002(02)01970-8.
- [70] C. E. Allgower et al. The STAR endcap electromagnetic calorimeter. *Nucl. Instrum. Meth.*, A499:740–750, 2003. doi: 10.1016/S0168-9002(02)01971-X.
- [71] W. J. Llope. Multigap RPCs in the STAR experiment at RHIC. *Nucl. Instrum. Meth.*, A661:S110–S113, 2012. doi: 10.1016/j.nima.2010.07.086.
- [72] Clemens Adler, Alexei Denisov, Edmundo Garcia, Michael J. Murray, Herbert Strobele, and Sebastian N. White. The RHIC zero degree calorimeter. *Nucl. Instrum. Meth.*, A470:488–499, 2001. doi: 10.1016/S0168-9002(01)00627-1.

- [73] C. Adler, A. Denisov, E. Garcia, M. Murray, H. Strobele, and S. White. The RHIC zero-degree calorimeters. *Nucl. Instrum. Meth.*, A499:433–436, 2003. doi: 10.1016/j.nima.2003.08.112.
- [74] W. J. Llope et al. The TOFp / pVPD time-of-flight system for STAR. *Nucl. Instrum. Meth.*, A522:252–273, 2004. doi: 10.1016/j.nima.2003.11.414.
- [75] J. Kiryluk. Local polarimetry for proton beams with the STAR beam beam counters. In *Spin physics. Polarized electron sources and polarimeters. Proceedings, 16th International Symposium, SPIN 2004, Trieste, Italy, October 10-16, 2004, and Workshop, PESP 2004, Mainz, Germany, October 7-9, 2004*, pages 718–721, 2005.
- [76] F. S. Bieser et al. The STAR trigger. *Nucl. Instrum. Meth.*, A499:766–777, 2003. doi: 10.1016/S0168-9002(02)01974-5.
- [77] J. M. Landgraf, Micheal J. LeVine, A. Ljubicic, D. Padrazo, John M. Nelson, and M. W. Schulz. An overview of the STAR DAQ system. *Nucl. Instrum. Meth.*, A499:762–765, 2003. doi: 10.1016/S0168-9002(02)01973-3.
- [78] B. G. Gibbard and T. G. Throwe. The RHIC computing facility. *Nucl. Instrum. Meth.*, A499:814–818, 2003. doi: 10.1016/S0168-9002(02)01978-2.
- [79] A. Rose. STAR integrated tracker. *eConf*, C0303241:THLT004, 2003.
- [80] G. Van Buren. Precision Calibration of the STAR TPC. In *Astroparticle, particle and space physics, detectors and medical physics applications. Proceedings, 10th Conference, ICATPP 2007, Como, Italy, October 8-12, 2007*, pages 1029–1033, 2008. doi: 10.1142/9789812819093_0174.
- [81] C. Pruneau, M. Calderon, B. Hippolyte, J. Lauret, and A. Rose. A new STAR event reconstruction chain. In *Computing in high energy physics and nuclear physics. Proceedings, Conference, CHEP'04, Interlaken, Switzerland, September 27-October 1, 2004*, pages 268–271, 2005. URL <http://doc.cern.ch/yellowrep/2005/2005-002/p268.pdf>.

- [82] D. Kayran, G. Wang, M. Bai, M. Blaskiewicz, A. V. Fedotov, W. Fischer, C. Montag, T. Satogata, and S. Tepikian. Beam Lifetime and Limitations during Low-Energy RHIC Operation. *Conf. Proc.*, C110328:2285–2287, 2011.
- [83] M. M. Aggarwal et al. *Phys. Rev.*, C83:034910, 2011.
- [84] M. Bleicher, E. Zabrodin, C. Spieles, S.A. Bass, C. Ernst, et al. *J.Phys.*, G25:1859–1896, 1999.
- [85] J. Allison et al. *Nuclear Science, IEEE Transactions on*, 53(1):270–278, Feb 2006.
- [86] S. Agostinelli et al. *Nuclear Instruments and Methods in Physics Research Section A: Accelerators, Spectrometers, Detectors and Associated Equipment*, 506(3):250 – 303, 2003.
- [87] Rene Brun, Federico Carminati, and Simone Giani. GEANT Detector Description and Simulation Tool. 1994.
- [88] L. Adamczyk et al. Di-hadron correlations with identified leading hadrons in 200 GeV Au + Au and d + Au collisions at STAR. *Phys. Lett.*, B751:233–240, 2015. doi: 10.1016/j.physletb.2015.10.037.
- [89] L. Adamczyk et al. Bulk Properties of the Medium Produced in Relativistic Heavy-Ion Collisions from the Beam Energy Scan Program. 2017.
- [90] Evan Sangaline. *Ups and Downs with a Bit of Strange: A STAR Analysis of $\pi/K/p$ Spectra at High p_T in Au+Au collisions at $\sqrt{s_{NN}} = 7.7, 11.5, 19.6, 27.0, 39.0, \text{ and } 62.4 \text{ GeV}$ and Its Physics Implications*. PhD thesis, University of California, Davis, 2014. URL https://drupal.star.bnl.gov/STAR/system/files/EWS_thesis.pdf.
- [91] Ekkard Schnedermann, Josef Sollfrank, and Ulrich W. Heinz. Thermal phenomenology of hadrons from 200-A/GeV S+S collisions. *Phys. Rev.*, C48:2462–2475, 1993. doi: 10.1103/PhysRevC.48.2462.

- [92] Xin-Nian Wang and Miklos Gyulassy. HIJING: A Monte Carlo model for multiple jet production in p p, p A and A A collisions. *Phys. Rev.*, D44:3501–3516, 1991. doi: 10.1103/PhysRevD.44.3501.
- [93] Xin-Nian Wang and Miklos Gyulassy. Gluon shadowing and jet quenching in A + A collisions at $s^{*}(1/2) = 200\text{-GeV}$. *Phys. Rev. Lett.*, 68:1480–1483, 1992. doi: 10.1103/PhysRevLett.68.1480.
- [94] Zi-Wei Lin, Che Ming Ko, Bao-An Li, Bin Zhang, and Subrata Pal. A Multi-phase transport model for relativistic heavy ion collisions. *Phys. Rev.*, C72:064901, 2005. doi: 10.1103/PhysRevC.72.064901.
- [95] S.A. Bass, M. Belkacem, M. Bleicher, M. Brandstetter, L. Bravina, et al. *Prog.Part.Nucl.Phys.*, 41:255–369, 1998.
- [96] Kathryn C. Meehan. The fixed-target experiment at STAR. *J. Phys. Conf. Ser.*, 742(1):012022, 2016. doi: 10.1088/1742-6596/742/1/012022.
- [97] Wikipedia, 2001. URL <https://en.wikipedia.org/wiki/Wikipedia>. [Accessed: 2017-03-07].